Physics-based and data-driven computational models of inelastic deformations

Thesis by
Eric Ocegueda

In Partial Fulfillment of the Requirements for the
Degree of
Doctor of Philosophy in Mechanical Engineering

CALIFORNIA INSTITUTE OF TECHNOLOGY
Pasadena, California

2023
Defended May 24, 2023

Eric Ocegueda
ORCID: 0000-0001-7845-6890

ACKNOWLEDGEMENTS

Thank you to everyone who has made my academic journey possible.

First, my deepest gratitude to my advisor Professor Kaushik Bhattacharya. His continued guidance, expertise, and natural curiosity have provided me with a mentor and motivation to grow as a researcher and educator. Through my work with Kaushik, I have not only learned modeling details but how to think, explore, and learn. I am grateful for this time, which has shaped me into a better person, researcher, and educator.

Next, I would like to thank my thesis committee: Prof. Guruswami Ravichandran, Prof. Nadia Lapusta, and Prof. Andrew Stuart. I am thankful to Ravi for his invaluable feedback during our weekly joint group meetings. My interactions with Nadia, as her teaching assistant for Continuum Mechanics, motivated me to continue developing as a researcher and educator. Andrew provided thought-provoking discussions and questions during our collaborative meetings.

I am indebted to the funding I have received from Army Research Laboratory's MEDE grant and NSF's Alliances for Graduate Education and the Professoriate (AGEP) fellowship. My involvement in MEDE introduced me to a variety of researchers from different laboratories while grounding my research. Further, the AGEP fellowship provided me support and motivation to pursue academia.

I have been fortunate to work with wonderful collaborators Burigede Liu, Margaret Trautner, and Andrew Stuart, both at Caltech and Cambridge. Their work and discussions on surrogate modeling were invaluable for the machine learning project.

I would like to acknowledge and thank those from my undergraduate studies at UC Berkeley that supported my success in a graduate program. My impactful faculty: Prof. Oliver O'Reilly and Prof. George Johnson, not only taught me rigorous engineering topics but motivated me to explore mechanics within a Ph.D. program. My mentor Douglas Varela, provided me with insights on the possibilities within research, education, and outreach, shaping my pursuit of a doctorate and more. My long-time friendships with Diana Gomez, Salvador Gomez, Goka Norbana, and Annarosa Robledo have been immensely supportive as we left Berkeley to pursue postgraduate degrees/careers.

I would like to thank all former and current members of the Bhattacharya and Ravi groups for the countless discussions and collaborations throughout the years. In par-

ticular, I thank Hao Zhou, Andrew Akerson, and Burigede Liu for our conversations on computational methods. My friends and current/former office-mates Sharan Injeti, Jack Weeks, Andrew Akerson, Vatsa Gandhi, Sathvik Sanagala, Aakila Rajan, Barry Lawlor, Amanda Toledo Barrios, Adeline Wihardja, Shengduo Liu, Maximo Cravero Baraja, and Taeho Kim for keeping the office a fun place I always looked forward going to, along with our food, snacks, and gaming breaks.

My appreciation goes to Jenni Campbell, Lynn Seymour, and Stacie Takase for their friendly assistance with various administrative questions (I always had). Additionally, Club Latino provided a break from academia that I always valued; in particular, I would thank fellow officers Salvador Gomez, Victor Garcia Ruiz, Anna Karen Orta, and our club advisor Yazmin Gonzalez for her constant support in organizing club activities.

Lastly, I am very thankful to my girlfriend, Thi Pham, and my family - parents (Amelia and Jose Ocegueda) and brother (Anthony Ocegueda) - for their unconditional love, support, and encouragement throughout my Ph.D. Specifically, this thesis is the culmination of the hard work and sacrifices of my parents and is therefore dedicated to them.

Eric Ocegueda
May 24, 2023

ABSTRACT

Crystalline materials inevitably exhibit inelastic deformation when applied to large enough loads. The behavior in this inelastic regime is a coupling of physics across several length scales: from initiating as defects at the atomic scale, interacting with crystal defects, and finally spanning multiple grains and influencing macroscopic stress behavior. These length-scale interactions make predicting material response an open challenge and an avenue for leveraging microscale physics for material design. This thesis examines developing physics-based and data-driven computational models to capture complex inelastic behavior at appropriate length scales.

First, we present a mesoscale model for capturing deformation twinning physics at the polycrystal scale. Mechanical twinning is a form of inelastic deformation observed in low-symmetry crystals, such as magnesium and other hexagonal close-packed (hcp) metals. Twinning, unlike slip, forms as bands collectively across grains with complex local morphology propagating into bulk behavior, drastically affecting strength and ductility. We, thus, propose a model where twinning is treated using a phase-field approach, while dislocation slip is considered using crystal plasticity. Lattice reorientation, length-scale effects, interactions between dislocations and twin boundaries, and twin and slip interactions with grain boundaries are all carefully considered. We first outline the model and its implementation using a novel approach of accelerated computational micromechanics in a two-dimensional, single twin-slip system, polycrystal case to demonstrate its capabilities. Finally, we consider multiple twin-slip systems and conduct three-dimensional simulations of polycrystalline magnesium. We summarize the insights gained from these studies and the implications on the macroscale behavior of hcp materials.

The second part of the thesis focuses on data-driven models for capturing microscopic history-dependent phenomena for multiscale modeling applications. The multiscale modeling framework has seen increased usage over the last few decades for its ability to capture complex material behavior over a range of time/length scales by solving a macroscale problem directly with a constitutive relation defined implicitly by the solution of a microscale problem. However, this implementation is computationally expensive — needing to solve a microscale problem at each point and time of the macroscopic calculation. In this study, we examine the use of machine learning by utilizing data generated through repeated solutions of a microscale problem to: (i) gain insights into the history dependent macroscopic

internal variables that govern the response and (ii) create a computationally efficient surrogate. We do so by introducing a recurrent neural operator, which can provide accurate approximations of the stress response and insights into the physics of the macroscopic problem. We illustrate these capabilities on a laminate composite and polycrystal made of elasto-viscoplastic materials, summarize insights on the learned internal variables, and accuracy of stress predictions.

PUBLISHED CONTENT AND CONTRIBUTIONS

[1] B. Liu, E. Ocegueda, M. Trautner, A. M. Stuart, and K. Bhattacharya. "Learning macroscopic internal variables and history dependence from microscopic models". In: *Journal of the Mechanics and Physics of Solids* (2023), p. 105329. ISSN: 0022-5096. DOI: https://doi.org/10.1016/j.jmps.2023.105329. URL: https://www.sciencedirect.com/science/article/pii/S0022509623001333.

E.O. participated in implementation of the unit cell problems, surrogate model development and analysis, generation of all figures shown, and in the writing of the manuscript.

TABLE OF CONTENTS

Acknowledgements . . . iii
Abstract . . . v
Published Content and Contributions . . . vii
Table of Contents . . . vii
List of Illustrations . . . x
List of Tables . . . xvii
Chapter I: Introduction . . . 1
1.1 Inelastic behavior of metals . . . 1
1.1.1 Dislocation slip . . . 1
1.1.2 Deformation twinning . . . 4
1.2 Research objectives . . . 6
Chapter II: Overview of inelastic models . . . 9
2.1 Dislocation slip models: crystal plasticity . . . 9
2.1.1 Flow kinematics . . . 9
2.1.2 Energy and evolution equations . . . 10
2.2 Deformation twinning models: phase field . . . 11
2.2.1 Kinematics . . . 11
2.2.2 Energy and evolution equations . . . 12
2.3 Combined twinning and dislocation models: pseudo-slip . . . 12
2.3.1 Flow kinematics . . . 13
2.3.2 Energy and evolution equations . . . 14
2.3.3 Other approaches for combined twin and slip . . . 14
Chapter III: Phase field approach to twinning . . . 16
3.1 Motivation . . . 16
3.2 Model . . . 18
3.2.1 Kinematics . . . 18
3.2.2 Free energy and stress . . . 20
3.2.3 Equilibrium and evolution . . . 21
3.2.4 Twin interface thickness . . . 22
3.2.5 Twin nucleation and propagation . . . 23
3.2.6 Polycrystal domains . . . 24
3.3 Implementation . . . 24
3.4 Model verification and exploration . . . 26
3.4.1 Single crystal simulations . . . 28
3.5 Twin-slip interactions in 2D polycrsytal material . . . 30
3.5.1 Typical results . . . 32
3.5.2 Asymmetry of response . . . 38
3.5.3 Proportional loading-unloading-reverse loading . . . 39
3.5.4 Non-proportional loading . . . 40

3.5.5 Twin and slip activity . . . 40
3.5.6 Texture . . . 44
3.5.7 Comparison with the results of a pseudo-slip model . . . 46
3.6 Discussion . . . 46
Chapter IV: Deformation twinning and dislocation slip interactions in polycrystalline Magnesium . . . 50
4.1 Motivation . . . 50
4.2 Extension of model . . . 52
4.2.1 Kinematics . . . 52
4.2.2 Free energy . . . 53
4.2.3 Equilibrium and evolution . . . 54
4.2.4 Twinning latent hardening . . . 55
4.2.5 Implementation . . . 56
4.3 Magnesium material parameters . . . 57
4.3.1 Anisotropic elasticity . . . 57
4.3.2 Plastic slip . . . 57
4.3.3 Deformation twinning . . . 58
4.4 Results . . . 60
4.4.1 Bi-crystal twin transmission . . . 60
4.4.2 Twin-slip evolution in polycrystal magnesium specimens . . . 63
4.4.3 Texture influence . . . 66
4.5 Discussion and conclusion . . . 67
Chapter V: Learning macroscopic internal variables and history dependence from microscopic models . . . 73
5.1 Introduction . . . 73
5.2 Background, proposed architecture, and training . . . 77
5.3 Elasto-viscoplastic laminated composite . . . 81
5.3.1 No strain hardening . . . 82
5.3.2 Exponential strain hardening . . . 88
5.4 Elasto-viscoplastic polycrystals . . . 90
5.5 Discussion . . . 93
Chapter VI: Conclusions and Future Works . . . 97
6.1 Summary of findings . . . 97
6.2 Future directions . . . 98
Bibliography . . . 102

LIST OF ILLUSTRATIONS

Number *Page*

1.1 Dislocation slip. (a) – (c) Dislocation slip motion through a crystalline material with red dislocation showing slip plane normal and slip direction — following [137]. (d) Slip band motion and arrest at a grain boundary [10]. (e) Hall-Petch effect — yield stress dependence on grain size (D) [75, 147]. Figures (d) and (e) are adapted (with permission) from [10, 147]. 3

1.2 Length-scale of dislocation slip. From left to right atomistic view of a single dislocation slip, several dislocation slips forming a slip band, slip bands creating strain heterogeneity inside a single crystal, and collection of slip bands across polycrystal domain. 3

1.3 Deformation twinning. (a) Schematic showing twin reorientation of a lattice and a slip system ($\perp$) rotation across the twin plane. (b) Electron back-scattering diffraction (EBSD) orientation mapping of zirconium under compression showing twin bands [103]. (c) Twinning frequency versus grain area size showing Hall-Petch effect for twinning [23]. (d) Tension-compression asymmetry of AZ31B magnesium alloy [73]. Figures (b) – (d) are adapted (with permission) from [23, 73, 103]. 5

1.4 Length-scale of deformation twinning. From left to right atomistic view of the formation of a twin plane, twin band propagating from grain boundary, twin band encompassing length of a single grain, and complex twin transmission across a polycrystal domain. 6

3.1 Twinning schematic. Parent and twinned lattice are shown with the respective dislocation slips in red. 19

3.2 Twin interface thickness versus $\sqrt{\frac{\alpha}{M}}$ for displacement control simulations on a single crystals in the absence of plastic slip. 23

3.3 Twin resolved shear stress (RSS) (a) Twin RSS versus applied shear for varying M. (b) Twin length scale related critical RSS versus M. . 24

3.4 Monocrystal twinning simulations. Average shear stress (dotted red line) and twin volume fraction (solid black line) versus applied strain for simple shear along (a) vertical and horizontal unit cell axes and (b) $\pi/8$ rotated axes of the unit cell. Twin microstructure plots are shown for a few representative times. 28
3.5 Monocrystal plasticity simulations. Plastic resolved shear stress versus strain for different crystal orientations, ψ is the relative angle between slip system and shear directions. Slip morphology at the final loading step are shown with border color and line type matching the stress curves. 30
3.6 Monocrystal twin-slip simulations. Average stress (dotted red curve), slip magnitude (dashed blue curve), and twin volume fraction (solid black curve) versus applied shear strain for loading along (a) the unit cell axes (aligned with twin directions), (b) $\pi/8$ rotated axes of the unit cell (aligned with neither) and (c) $\pi/4$ rotated axes of the unit cell (aligned with slip). 31
3.7 Deformation of polycrystalline specimen subjected to simple shear. (a) The polycrystalline specimen. The grayscale shows the propensity for twinning and slip. The darker grains are favorably oriented for slip and lighter grains for twinning, while the numbers indicate the grain orientation. (b) Stress-strain behavior and evolution of average slip magnitude and twin volume fraction. Vertical dashed lines indicate points at which microstructure is shown. (c–f) Snapshot of twin volume fraction (η) at strains of $\gamma = 0.01, 0.044, 0.07, 0.1$. Gray and white arrows show twin and reciprocal twin directions, respectively. (g–j) Snapshots of accumulated slip magnitude (ϵ^{p}) at strains of $\gamma = 0.01, 0.044, 0.07, 0.1$. 33
3.8 Nucleation. (a) Slip nucleation at $\gamma = 0.01$. (b) Twin nucleation at $\gamma = 0.04$. 34
3.9 Geometrically necessary dislocation density. Magnitude of the curl of (a) twinning, (b) plastic slip, and (c) inelastic (plastic and twinning) deformations. 36

3.10 Statistical features of inelastic deformations for the Figure 3.7 case. (a–c) Heat map showing the distribution of twin volume fraction and plastic activity as a function of grain orientation at strains of $\gamma = 0.01, 0.044, 0.1$, respectively. Blue represents little activation at that orientation and inelastic value, while red represents a larger number of material points with that orientation and inelastic value. (d–e) Cumulative histogram of twin and slip activity v.s. nominal driving force. 37

3.11 Asymmetry of response. Deformation of polycrystalline specimen subjected to reversed simple shear loading compared to Figure 3.7. (a) The polycrystalline specimen. The grayscale shows Schmidt factors for twinning and slip. Darker grains are favorably oriented for slip and lighter grains for twinning, while the numbers indicate the grain orientation. (b) Stress-strain behavior and evolution of average slip magnitude and twin volume fraction. (c) Snapshot of twin volume fraction (η) and slip magnitude (γ^{p}) at the final strain of $\gamma = -0.1$. 38

3.12 Proportional forward-reverse deformation. (a) Average twin volume fraction and slip magnitude versus shear strain. (b) Average stress-strain plot with markers indicating points at which microstructure plots are obtained. (c–f) Twin volume fractions at points during the reverse loading. (g–j) Slip magnitudes at points during the reverse loading. 39

3.13 Non-proportional loading. Three macroscopic strain paths (a) are simulated with identical final strain. (b) Shear stress paths for each loading. Average twin volume fraction and slip magnitude and final twin and slip morphology for path 1 (c–e), path 2 (f–h), and path 3 (i–k). 41

3.14 Role of surface energy. Average stress, twin volume fraction and slip magnitude, final twin, and slip microstructure for (a–c) $M = 8$ MPa (d–f) $M = 80$ MPa and (g–i) $M = 800$ MPa. All other parameters as before. 42

3.15 Effect of twin rate hardening. Average stress, twin volume fraction and slip magnitude, final twin, and slip microstructure for (a–c) $\tau_0^{\mathrm{t}} =$ 0.1 MPa, (d–f) $\tau_0^{\mathrm{t}} = 1$ MPa and (g–i) $\tau_0^{\mathrm{t}} = 10$ MPa. 43

3.16 Effect of slip rate hardening. Average stress, twin volume fraction and slip magnitude, final twin, and slip microstructure for (a–c) $\tau_0^{\mathrm{p}} = 0.4$ MPa, (d–f) $\tau_0^{\mathrm{p}} = 4$ MPa and (g–i) $\tau_0^{\mathrm{p}} = 40$ MPa. 44

3.17 Role of texture. Deformation of the different polycrystalline specimens subjected to simple shear. Polycrystalline specimen for twin centered (a) and slip centered (b) grain angles. The grayscale shows Schmidt factors for twinning and slip. Darker grains are favorably oriented for slip and lighter grains for twinning, while the numbers indicate the grain orientation. Stress-strain behavior and average inelastic deformations for twin centered (c) and slip centered (f) grains. Final twin volume fraction (η) and slip magnitude (γ^{p}) at a final strain of $\gamma = 0.1$ for twin centered (d–e) and slip centered (g–h) grains. . . . 45

3.18 Comparison with pseudo-slip model. Stress strain curve and average slip magnitude and twin volume fraction for phase-field (a) and pseudo slip (b). The gray dashed lines correspond to points where the microstructure is plotted. Phase-field's twin volume fraction (c–f) and pseudo slip's twin volume fraction (g–j) at strains of $\gamma = 0.01, 0.044, 0.07, 0.1$. Phase-field's slip magnitude (k–n) and pseudo slip's twin volume fraction (o–r) at strains of $\gamma = 0.01, 0.044, 0.07, 0.1$. 47

4.1 Magnesium inelastic systems accounted for in simulations. (a) – (c) are the dislocation slip systems and (d) is the deformation twinning system. 58

4.2 Bicrystal sample. 60

4.3 Twin-slip configurations for twin transmission through x-axis rotated bicrystal. The twin configuration (a, e, i), basal slip (b, f, j), prismatic slip (c, g, k), and prismatic slip (d, h, l) are shown at a strain of $\varepsilon = 0.06$ for the angles listed. 62

4.4 Twin arrest at grain a boundary with (a) 30° and (b) 45° rotation at a strain of $\varepsilon = 0.06$. 63

4.5 Bulk response for bicrystal study. (a, d, g) Average twin volume fraction, (b, e, h) bulk slip magnitudes, and (c, f, i) stress-strain response for misalignment angles shown. 64

4.6 Polycrystal (nine grains) sample with color mapping showing propensity for slip (blue) or twinning (red). 65

4.7 Bulk response for nine grain sample. (a) Average twin volume fraction, (b) bulk slip magnitudes, and (c) stress-strain response. 65
4.8 Polycrystal magnesium simulation. The configuration for both twin systems (a – c) and (d – f), basal slip (g – i), prismatic slip (j – l), and pyramidal slip (m – n) are shown for strains of $\varepsilon = 0.02,\ 0.0325,\ 0.06$. 69
4.9 Twin-slip nucleation in slice of polycrystal magnesium specimen. (a) Grain texture with grain misalignment across grains $1-2:\ 30^\circ$ and $1-3:\ 61^\circ$. (b) and (d) Basal slip magnitude at strains of $\varepsilon = 0.03$ and $\varepsilon = 0.035$, respectively. (c) and (e) Twin volume fraction at strains of $\varepsilon = 0.0325$ and $\varepsilon = 0.035$, respectively. 70
4.10 Polycrystal texture simulation. The configuration for both twin systems (a – b, f – g, k – l), basal slip (c, h, m), prismatic slip (d, i, n), and pyramidal slip (e, j, o) shown at a strain of $\varepsilon = 0.06$ for the three texture listed. 71
4.11 Polycrystal texture bulk response. (a, d, g) Average twin volume fractions, (b, e, h) average slip magnitudes, and (c, f, i) stress strain response for the listed initial texture cases. 72
5.1 A laminate composite and the unit cell domain. 81
5.2 Approximating an elasto-viscoplastic laminate with no-strain hardening with a recurrent neural operator. (a) Training RNOs with various numbers of internal variables. In each case, we train the homogeneous material (MH) and then use transfer learning. The notation A ($\leftarrow B$) indicates the case A was trained using transfer learning from B. (b) Comparison of the ground truth and RNO prediction of the stress for eight arbitrarily chosen test strain trajectories for the case M3 with three internal variables. (c–f) Training RNOs with various numbers of internal variables both directly and with transfer learning. 83

5.3 Reducing the number of the model variables using an auto-encoder. (a) The error of approximating the model variables (state variables in the original laminate model) with an auto-encoder for various reduced dimensions. (b) Comparison between the computed values of the model variables and the recovered values from the trained auto-encoder for eight arbitrarily chosen trajectories in the test data for the case M3 with three reduced variables. (c) The computed values of the model variables in the the two layers for eight arbitrarily chosen trajectories in the test data for the case M3. (d) Comparison of the computed stress response (solid) with the learnt stress response (dashed) for a typical test trajectory for the case M3. (e) Comparison of the computed plastic strains model variables (solid) with the reconstructed plastic strain (dashed) for a typical test trajectory for the case M3. (f) Comparison of the computed stress with the learnt stress for eight test trajectories for the case M3. 85

5.4 Reconstructing the micromechanical model variables from the macroscopic internal variables for the case M3. Comparison between the computed values of the model variables and the recovered values from the RNO internal variables for (a) an arbitrarily chosen trajectory and (b) eight arbitrarily chosen trajectories. 87

5.5 Approximating an elasto-viscoplastic laminate with exponential strain hardening. (a–c) Learning the strain history to stress history map with a recurrent neural operator: (a) Training RNOs with various numbers of internal variables. In each case, we train the homogeneous material with no hardening (MH–NH) and then use transfer learning. (b) Training RNOs with various numbers of internal variables both directly and with transfer learning. (c) Comparison of the ground truth and RNO output for eight test strain trajectory for the case M3-EH with four internal variables. (d–f) Reducing the number of the internal variables using an auto-encoder: (d) The error of approximating the model variables (state variables in the original laminate model) with an auto-encoder for various reduced dimensions. (e) Comparison between the computed values of the model variables and the recovered values from the trained auto-encoder for eight arbitrarily chosen trajectories in the test data for the case M3–EH with a reduced dimension of four. (f) The computed values of the model variables in the the two layers for eight arbitrarily chosen trajectories in the test data for the case M3–EH. 89

5.6 Approximating two dimensional polycrystalline elasto-viscoplasticity with a recurrent neural operator. (a) Training RNOs with various numbers of internal variables with increasing epochs. (b) Test error of the trained RNOs of the deviatoric stress with various number of internal variables and rate hardening cases. (c) Test error of the trained RNOs of the hydrostatic pressure with various number of internal variables and rate hardening cases. (d) A typical average deformation gradient history input from the test data. (e) Comparison of the resulting deviatoric stress history for the test data (solid) and the prediction of the RNO with two internal variables (dashed) for case PH. (f) Test error of the trained RNOs of the deviatoric stress with various number of internal variables and strain hardening cases. 92

LIST OF TABLES

Number *Page*

1.1 Dislocation slip directions and planes of various common crystal structures [82]. . . . 2
1.2 Twin directions, planes, and shear magnitude of various common crystal structures [49]. . . . 4
3.1 Material parameters used for two-dimensional polycrystal simulations. 32
4.1 Experimentally-determined transversely-isotropic elastic constants of pure Mg at 280 K (Slutsky and Garland, 1957). . . . 57
4.2 Plastic slip hardening and dissipation parameters for magnesium simulations [42, 43]. . . . 59
4.3 Twin hardening and dissipation parameters for magnesium simulations from [42, 43, 49, 118], phase field parameters informed from simulations and theory [50, 98, 109, 125, 151, 153, 158]. . . . 60
4.4 Twin and slip Schmid factors for bicrystal simulations. . . . 61
5.1 Material parameters used for laminates along with labels (and colors) used for plotting. . . . 83
5.2 Material parameter cases used for polycrystals unit cell simulations in two dimensions. . . . 91

Chapter 1

INTRODUCTION

1.1 Inelastic behavior of metals

Metals subjected to small forces respond elastically — upon removal of the force, the metal recovers its original shape. However, larger loads lead to inelastic deformations involving permanent (irrecoverable) shape changes. Such inelastic deformations significantly affect engineering materials' stress response and ultimate failure [31, 56]. The observed macroscopic inelastic response of metals is heavily dictated by complex interactions of smaller scale physics [35, 137]. Firstly, different inelastic deformations initiate through nucleation of crystallographic defects, such as dislocations or deformation twinning, which depend on the crystal structure for relative activation thresholds. Secondly, dislocations, twins, or other defects create strain localization that interacts with other preexisting defects such as vacancies, grain boundaries, or dislocations and twins themselves. Lastly, the resulting collection of interacting crystal imperfections leads to stress concentrations, local hardening, and further inelastic strains across the single-grain and polycrystal scale. Thus, the resulting material behavior heavily depends on microscale crystal structure, texture information, strain history, and loading conditions, requiring an understanding of defects in crystalline materials and their connection to controllable factors in metals to better tailor materials for complex engineering loading conditions. The two main inelastic deformation mechanisms of importance for this thesis are dislocation slip and deformation twinning, which encompass a wide range of complex behavior observed in engineering materials.

1.1.1 Dislocation slip

The plastic deformation most commonly observed in metals occurs through the accumulated motion of dislocations. Dislocations are linear defects, where a portion of the lattice slides relative to another (seen in Figure 1.1 (a) – (c)), and nucleates in order to accommodate large macroscopic stress [137]. The lattice translation occurs through the breaking and reforming of bonds, leading to a permanent deformation confined to specific slip directions and planes. The directions associated with dislocation slip are along densely packed directions/planes since the threshold for reforming bonds is lowest in these directions. Thus, the directions and nucle-

crystal structure	slip plane	slip direction
face centered cubic	$\{111\}$	$\langle 110 \rangle$
body centered cubic	$\{110\}$	$\langle 111 \rangle$
	$\{112\}$	$\langle 111 \rangle$
	$\{123\}$	$\langle 111 \rangle$
hexagonal close packed	$\{0001\}$	$\langle 11\bar{2}0 \rangle$
	$\{1\bar{1}00\}$	$\langle 11\bar{2}0 \rangle$
	$\{11\bar{2}2\}$	$\langle \bar{1}\bar{1}23 \rangle$

Table 1.1: Dislocation slip directions and planes of various common crystal structures [82].

ation thresholds for dislocation slip depend on the crystal structure, with the slip planes/directions (given using Miller indices) in a few crystal structures shown in Table 1.1.

The reforming of bonds in a dislocation slip means that a single defect occurs at atomic scales. The accumulation/motion of several dozens to hundreds of these defects form slip systems (or slip bands) that appear at the single crystal scale [1, 4, 8, 18, 21, 81, 100, 101]. For example, using high-resolution SEM, slip bands can be found inside a single grain, Figure 1.1 (d) [10]. The interaction of several slip systems forms dislocation patterns at the sub-grain scale, which form heterogeneous strain patterns that interact with other defects inside a crystal. Finally, at the polycrystal scale, the collection of different crystal orientations and slip's directional dependence leads to differing dislocation patterns across multiple grains. Figure 1.2 depicts the hierarchy of length-scales for plasticity, from the nucleation of discrete dislocations at the atomistic scale to the presence of slip bands/patterns across single and multiple grains.

Observed macroscopic inelastic behavior, such as yielding or strain hardening of metals, occurs through the motion of several (often hundreds or more) of these dislocation slips coupled with their interactions with lattice defects or impurities at several length scales. For example, the yielding of a metal is the nucleation and motion of several new dislocations across a large portion of the material. While hardening effects such as grain refinement, solid solutions, precipitation, or cold working, work to impede the movement of dislocations by introducing defects (in the form of grain boundaries, impurities, or dislocations) where significant stresses

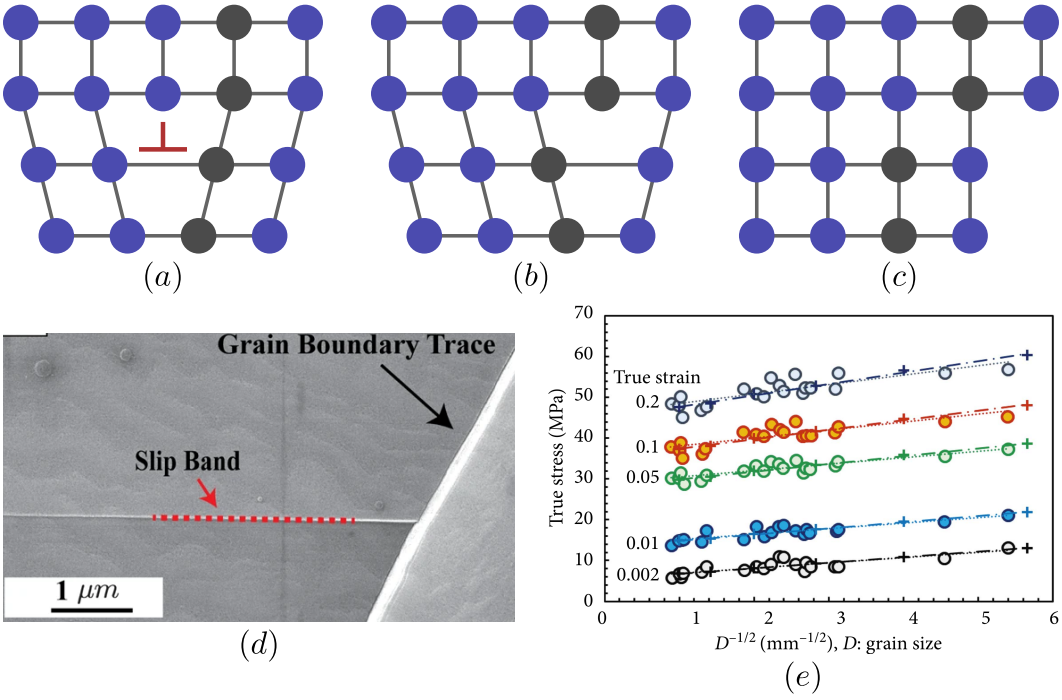

Figure 1.1: Dislocation slip. (a) – (c) Dislocation slip motion through a crystalline material with red dislocation showing slip plane normal and slip direction — following [137]. (d) Slip band motion and arrest at a grain boundary [10]. (e) Hall-Petch effect — yield stress dependence on grain size (D) [75, 147]. Figures (d) and (e) are adapted (with permission) from [10, 147].

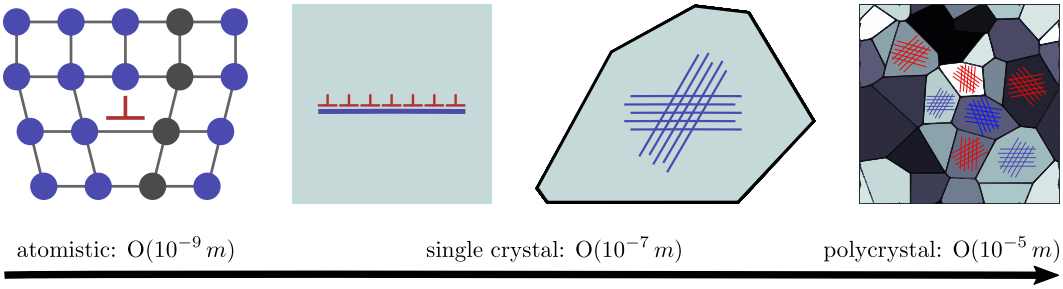

Figure 1.2: Length-scale of dislocation slip. From left to right atomistic view of a single dislocation slip, several dislocation slips forming a slip band, slip bands creating strain heterogeneity inside a single crystal, and collection of slip bands across polycrystal domain.

crystal structure	twin plane	twin direction	twinning shear
face centered cubic	$\{111\}$	$\langle 112\rangle$	0.707
body centered cubic	$\{112\}$	$\langle 111\rangle$	0.707
hexagonal close packed	$\{10\bar{1}2\}$	$\langle\bar{1}011\rangle$	0.129
	$\{10\bar{1}1\}$	$\langle\bar{1}012\rangle$	1.066

Table 1.2: Twin directions, planes, and shear magnitude of various common crystal structures [49].

are necessary to allow further dislocation propagation [13, 137]. Figure 1.1 (d) shows examples of the pinning of dislocation slip bands at a grain boundary, and Figure 1.1 (e) shows the effect grain size (known as the Hall-Petch effect) has on the material yield stress and hardening [74, 133].

1.1.2 Deformation twinning

Deformation twinning is an alternative inelastic deformation that occurs profusely in low-symmetry metals such as hcp magnesium or zirconium, where dislocation slip cannot fully activate due to high nucleation thresholds [118]. Despite seeming similar to dislocation slip, deformation twinning has several differences creating unique material responses. Twinning is a planar defect that occurs from the coordinate shearing of a portion of the lattice to create an identical but rotated, "twinned" lattice, see Figure 1.3 (a). Like slip, twinning is confined to specific shear directions and twin planes that are crystal structure dependent and well tabulated for various crystalline materials; see Table 1.2 for a few examples of twinning shear magnitudes and twin planes/directions given in Miller indices.

The nucleation of deformation twins occurs at the atomic scale where preexisting dislocations, either inside the lattice [39, 51, 84, 118, 121, 135] or at grain boundaries [17, 22, 25], dissociate into twin partials. These twin partials form into a sub-micron size twin band whose boundaries propagate under stress inside a single grain. Eventually, the twins span the entire crystal, terminating at grain boundaries where they can promote twin transmission into neighboring grains. Finally, twin bands can be seen several microns thick at the polycrystal scale, spanning multiple grains. For example, Figure 1.3 (b) shows electron-back scattering diffraction (EBSD) scans of an hcp zirconium specimen under compression, where different colors are related to the relative orientation of the local lattice. From the EBSD scan, we can see sharp, bright twin bands present within and across multiple grains [103]. These

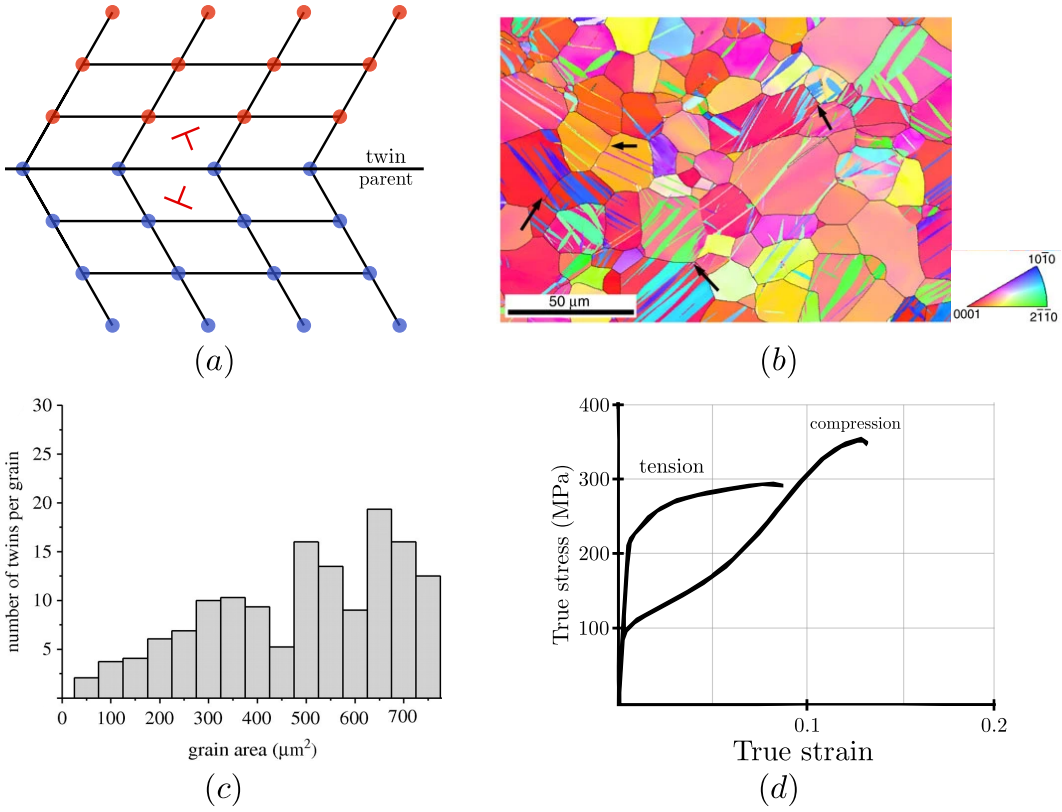

Figure 1.3: Deformation twinning. (a) Schematic showing twin reorientation of a lattice and a slip system (⊥) rotation across the twin plane. (b) Electron backscattering diffraction (EBSD) orientation mapping of zirconium under compression showing twin bands [103]. (c) Twinning frequency versus grain area size showing Hall-Petch effect for twinning [23]. (d) Tension-compression asymmetry of AZ31B magnesium alloy [73]. Figures (b) – (d) are adapted (with permission) from [23, 73, 103].

twin bands at the multiple grain scale introduce a twinning length scale that interacts in polycrystal specimens ([15, 17, 20, 40, 152]). Figure 1.4 summarizes the different length scales involved in the nucleation, propagation, growth, and transmission of deformation twinning. Lastly, unlike slip, twinning has a specific sense, i.e., it can nucleate under shear in one direction but not the other, leading to an asymmetric response under loading. While dislocation slip is symmetric, it can nucleate due to shear in either direction, leading to a contrast in material response dependent on the presence of dislocation slip or deformation twinning.

Finally, the rich microscale of twin morphology interacts with local defects, leading to drastic material responses. For example, twinning is reversible in isolation, known as detwinning; however, dislocation slip can pin twin bands preventing un-

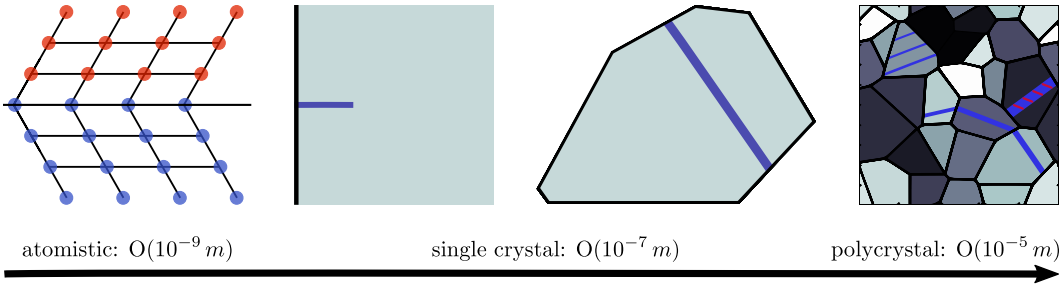

Figure 1.4: Length-scale of deformation twinning. From left to right atomistic view of the formation of a twin plane, twin band propagating from grain boundary, twin band encompassing length of a single grain, and complex twin transmission across a polycrystal domain.

loading and leaving permanent deformation. Additionally, the presence of twinning often promotes further slip activity. The sharp twin bands that often appear at the polycrystal scale lead to a heterogeneous stress state, which, coupled with the new rotated slip directions in the twin lattice, allow an increase in dislocation slip propagation and possible nucleation of high threshold slip systems. These twin-slip interactions increase inelastic deformations leading to a complex hardening response that is heavily load dependent. For example, Figure 1.3 (d) shows the well-known tension-compression asymmetry of an hcp magnesium alloy, which is a result of complex twin-slip interactions [73]. Lastly, the hardening techniques used to delay slip nucleation hold, to an extent, for preventing twin yielding. Figure 1.3 (c) shows experimental data of twin nucleation frequency in magnesium grains, where we can see a grain size dependence, i.e., smaller grains have decreased twins per grain [23].

1.2 Research objectives

Here we present two different research studies on developing accurate and efficient computational models to capture inelastic deformations in crystalline materials at the mesoscale. The goal of these studies are to create tools necessary for describing complex physics that dictates material behavior at large-scales. The first study focuses on modeling complex twin-slip interactions through detailed incorporation of both dislocation slip and deformation twinning. For several decades, there has been significant interest in correctly modeling and simulating twinning along with plasticity due to the complex mesoscale interaction of these defects' significant effects on material response. However, the main challenge of modeling twinning is its complex band morphology, lattice rotation, and asymmetry in nucleation, which typical dislocation slip models need to include. Hence, we propose a detailed

phase-field model for deformation twinning to adequately capture twin-specific features, modify a classic crystal plasticity model to include dislocation slip coupling with twin activity and utilize an operator splitting method for an efficient parallel implementation of high-resolution polycrystal simulations. We split the study into two parts. The first part aims to showcase the power of our phase field model to efficiently illustrate detailed twin-slip interactions by conducting two-dimensional single-crystal and polycrystal simulations with a single twin and slip system. The second part of the work examines the extension of the model to three dimensions with multiple twin and slip systems and illustrates its capabilities to capture realistic twin morphology and interactions by applying it to hcp magnesium polycrystal specimens.

The second study explores machine learning techniques for creating efficient and accurate surrogate models of mesoscale inelastic simulations for application in multiscale modeling. Recent years have seen an increase in using multiscale modeling to adequately capture complex microscale and mesoscale features that greatly affect the behavior of materials. For example, consider a polycrystalline solid with grains significantly smaller than the overall dimensions of the solid, subjected to macroscopic loads. Each grain is governed by dislocation slip (and possibly deformation twinning) with heterogeneous strain and strain-rate distributions forming a complex history dependence. Existing multiscale models/simulations methods can properly couple microscopic unit cell and macroscopic simulations; however, these methods are extremely computationally expensive since the unit cell problem must be solved at each time step and material point. Hence, we examine the use of machine learning neural networks, motivated by internal variable theories in continuum modeling, to efficiently generate a surrogate model for the unit cell problem. We first illustrate the method's accuracy for a simple laminate elasto-viscoplastic composite and a more complex two-dimensional polycrystal comprised of an elasto-viscoplastic material. Secondly, we emphasize the insights the surrogate model can provide on macroscopic internal variables governing the material response and their possible connection to microscopic variables.

The remainder of the dissertation is organized as follows.

In Chapter 2, we first review common computational approaches for mesoscale modeling of dislocation slip, deformation twinning, and both. This overview explains the crystal plasticity model utilized repeatedly throughout the dissertation and the standard twin-slip model, pseudo-slip, which we contrast to our phase field

approach.

In Chapter 3, we introduce the phase field approach to describe twinning in the context of two-dimensional single twin-slip system materials. We use this simplified case to explore and emphasize the details of the phase field model: twin-slip interactions, nucleation barriers from twin surface energy, and texture influence from twin asymmetry.

In Chapter 4, we extend the model developed in Chapter 3 to include multiple twin and slip systems in three dimensions. In addition, we apply the model to polycrystal magnesium specimens to emphasize the model's capabilities to capture texture's and non-local twin-slip interaction's influence on twin transmission and inelastic response.

In Chapter 5, we outline the machine learning approach, coined recurrent neural operator (RNO), to fit a surrogate model for a microscale unit cell problem. We showcase detailed studies on the capabilities of the RNO for two problems: a laminate elasto-viscoplastic composite and a polycrystal elasto-viscoplastic metal. The first problem is a simpler case, where we can verify the RNO results and the fitted internal variables. The second problem is much more involved and computationally expensive, so we focus on showcasing the accuracy of the RNO model and hints the fitted internal variables provide. We conclude with a discussion of findings and further work explored.

In Chapter 6, we conclude with a summary of results and contributions toward modeling inelastic deformations. Lastly, we provide some suggestions for future work on the discussed approaches.

Chapter 2

OVERVIEW OF INELASTIC MODELS

This chapter briefly summarizes the common mesoscale computational models used to describe dislocation slip, deformation twinning, and both twin and slip. These approaches will serve as background information used throughout the dissertation.

2.1 Dislocation slip models: crystal plasticity

The computational approaches for describing dislocation slip in mesoscale simulations have long been established and developed since the first implementations by Peirce et al. [132]. These mesoscale approaches aim to predict the stress-strain response and capture local strain localization and texture information assuming dislocation slip is the only plastic deformation. Here we will outline the phenomenological-based variational approach, crystal plasticity, which allows incorporating grain, crystal structure, and dislocation information in a continuum model.

2.1.1 Flow kinematics

The local deformation of the body will be governed by a deformation mapping $\boldsymbol{y}(\boldsymbol{x})$, which maps the reference (stress-free) configuration to the deformed configuration based on the loading conditions. Assuming finite strains, covered here since the case of infinitesimal strains would be a linearized simplification, the deformation gradient $\mathbf{F} = \nabla\mathbf{y}$ is multiplicatively decomposed, following Rice [140] and other researchers [76, 106], into

$$\mathbf{F} = \mathbf{F}^{\mathrm{e}}\mathbf{F}^{\mathrm{p}}, \tag{2.1}$$

where, $\mathbf{F}^{\mathrm{e}}$ and $\mathbf{F}^{\mathrm{p}}$ denote the elastic and plastic (dislocation slip related) deformation gradients. The plastic deformation gradient evolution is governed through the spatial velocity gradient $\mathbf{L} = \nabla\mathbf{v} = \dot{\mathbf{F}}\mathbf{F}^{-1}$, which simplifying using the gradient decomposition leads to,

$$\mathbf{L} = \mathbf{L}^{\mathrm{e}} + \mathbf{L}^{\mathrm{p}} \quad \text{with} \quad \mathbf{L}^{\mathrm{e}} = \dot{\mathbf{F}}^{\mathrm{e}}\mathbf{F}^{\mathrm{e}}, \;\; \mathbf{L}^{\mathrm{p}} = \mathbf{F}^{\mathrm{e}}\tilde{\mathbf{L}}^{\mathrm{p}}\mathbf{F}^{\mathrm{e}-1}, \;\; \text{and} \;\; \tilde{\mathbf{L}}^{\mathrm{p}} = \dot{\mathbf{F}}^{\mathrm{p}}\mathbf{F}^{\mathrm{p}} \tag{2.2}$$

where $\mathbf{L}^{\mathrm{e}}$ and $\mathbf{L}^{\mathrm{p}}$ are the deformed elastic and plastic contributions to the velocity gradient and $\tilde{\mathbf{L}}^{\mathrm{p}}$ is the plastic velocity gradient in the reference configuration.

To complete the plastic deformation update, we define a plastic flow rule, motivated by the fact that at the crystal scale, dislocation slip occurs along specific slip directions and planes,

$$\tilde{\mathbf{L}}^{\mathrm{p}} = \dot{\mathbf{F}}^{\mathrm{p}}\mathbf{F}^{\mathrm{p}} = \sum_{\alpha=1}^{N} \dot{\gamma}_{\alpha}\hat{\mathbf{b}}_{\alpha}^{\mathrm{p}} \otimes \hat{\mathbf{n}}_{\alpha}^{\mathrm{p}}, \tag{2.3}$$

where $\dot{\gamma}_{\alpha}^{\mathrm{p}}$ is the plastic slip rate on system α, characterized by slip direction $\hat{\mathbf{b}}_{\alpha}^{\mathrm{p}}$ and normal $\hat{\mathbf{n}}_{\alpha}^{\mathrm{p}}$ on N slip systems [99, 140]. The additive decomposition of the flow rule in equation 2.3 uses a linearization of the nonlinear plastic deformations along different dislocation slips ($\mathbf{F}^{\mathrm{p}} = \mathbf{F}^{\mathrm{p}(n)}\mathbf{F}^{\mathrm{p}(n-1)} \cdots \mathbf{F}^{\mathrm{p}(1)}$ where each $\mathbf{F}^{\mathrm{p}(k)}$ represents the plastic deformation associated with a single dislocation slip). For the context of grain-scale simulations, the first-order approximation holds since the individual deformations on slip systems are at the atomic scale. Lastly, note that since the slip direction and normal are perpendicular, the flow rule keeps the plastic deformations volume preserving,

$$\mathrm{tr}\left(\tilde{\mathbf{L}}^{\mathrm{p}}\right) = \sum_{\alpha=1}^{N} \dot{\gamma}_{\alpha}\hat{\mathbf{b}}_{\alpha}^{\mathrm{p}} \cdot \hat{\mathbf{n}}_{\alpha}^{\mathrm{p}} = 0, \tag{2.4}$$

as is commonly observed.

2.1.2 Energy and evolution equations

The variational approach to crystal plasticity relies on introducing energy and power terms to compactly represent the stress equilibrium and evolution of the internal variable, γ^{p}. The Helmholtz free energy density is postulated in the following additive decomposition,

$$W(\mathbf{F}^{\mathrm{e}}, \epsilon^{\mathrm{p}}) = W^{\mathrm{e}}(\mathbf{F}^{\mathrm{e}}) + W^{\mathrm{p}}(\epsilon^{\mathrm{p}}), \tag{2.5}$$

where W^{e} is the elastic strain energy density dependent on the elastic deformation and W^{p} is the plastic hardening energy dependent on the accumulated plastic strains $\epsilon_{\alpha} = \int |\dot{\gamma}_{\alpha}^{\mathrm{p}}|\, dt$ [54]. The power term introduced is the dissipation potential $\Psi^{*}(\dot{\gamma}^{\mathrm{p}})$ ([130]) and captures any rate dependence to plastic evolution. Finally, using the principle of minimum dissipation potential ([41, 53, 130]), the evolution of the plastic strain variable is given from the stationary point of the total stress power,

$$\frac{\partial}{\partial \dot{\gamma}^{\mathrm{p}}}\left(\dot{W} + \Psi^{*}\right) \ni 0. \tag{2.6}$$

Note that the equation is written with a differential inclusion to account for rate-independent cases.

Simplifying the stationary point using equation 2.5, we obtain a typical plastic evolution form,

$$-\tau_\alpha^{\mathrm{p}} + \frac{\partial W^{\mathrm{p}}}{\partial \dot{\gamma}^{\mathrm{p}}} + \frac{\partial \Psi^*}{\partial \dot{\gamma}^{\mathrm{p}}} \ni 0 \quad \text{with} \quad \tau_\alpha^{\mathrm{p}} = \sigma_{\mathrm{M}} : (\hat{\mathbf{b}}_\alpha^{\mathrm{p}} \otimes \hat{\mathbf{n}}_\alpha^{\mathrm{p}}) \tag{2.7}$$

where τ_α^{p} is the resolved shear stress for the α slip system and σ_{M} is the Mandel stress tensor. The resolved shear stress indicates the local driving force for slip nucleation/propagation, while the Mandel stress is the local stress measure that is the work conjugate of the plastic strain. The remaining derivatives in equation 2.7 correspond to hardening terms the resolved shear stress must overcome for slip nucleation or propagation. Specifically, $\frac{\partial W^{\mathrm{p}}}{\partial \dot{\gamma}^{\mathrm{p}}}$ will contribute a strain hardening to both nucleation and propagation and $\frac{\partial \Psi^*}{\partial \dot{\gamma}^{\mathrm{p}}}$ will add a strain rate hardening effect only to the propagation of dislocation slip.

2.2 Deformation twinning models: phase field

Several computational approaches have been explored over the last several decades to describe deformation twinning and its resulting morphology. One of which we build off in the proceeding chapters is phase field modeling of twinning. The pioneering studies of heterogeneous materials through the use of phase field models were proposed by Cahn and Hilliard [37] and Allen and Cahn [9], while its specific use for twinning with elasticity was developed by Hu *et al.* and other researchers [50, 78, 79, 116]. Here we outline an introductory phase field model for one twin system with finite elasticity in the absence of plasticity. The formulation can capture twin morphology in single-crystal or polycrystal domains and describes its coupling with finite strain elasticity.

2.2.1 Kinematics

We assume the existence of a phase field variable, $\eta \in H^2$, which distinguishes whether a material point is in the parent lattice ($\eta = 0$), the twinned lattice ($\eta = 1$), or an interface region ($\eta \in (0, 1)$). The parameter, η, will define the twinned related deformation gradient as an interpolation of a simple shear [85, 109],

$$\mathbf{F}^{\mathrm{t}} = \mathbf{I} + \eta \gamma_0^{\mathrm{t}} \hat{\mathbf{s}} \otimes \hat{\mathbf{m}} \tag{2.8}$$

where γ_0^{t}, $\hat{\mathbf{s}}$, and $\hat{\mathbf{m}}$ are the twin shear, shear direction, and normal of the twin plane specific to the crystalline structure. The total deformation gradient can then be split into elastic and twinning parts in the multiplicative decomposition,

$$\mathbf{F} = \mathbf{F}^{\mathrm{e}} \mathbf{F}^{\mathrm{t}}. \tag{2.9}$$

2.2.2 Energy and evolution equations

Classical phase field models make an ansatz [9] that a material system will evolve towards a state of minimum free energy. Thus, here we follow this by postulating that the Helmholtz free energy is decomposed additively to,

$$W(\mathbf{F}^{\mathrm{e}}, \eta, \nabla\eta) = W^{\mathrm{e}}(\mathbf{F}^{\mathrm{e}}, \eta) + W^{\mathrm{t}}(\eta, \nabla\eta), \tag{2.10}$$

where W^{e} is the elastic strain energy density dependent on the twinning parameter, η, in the case of an anisotropic elastic model where the twin-related lattice rotations affect the stiffness tensor. W^{t} is the twinning interfacial energy taking the form,

$$W^{\mathrm{t}}(\eta) = \frac{M}{2}\eta^2(\eta - 1)^2 + \frac{\alpha}{2}||\nabla\eta||^2, \tag{2.11}$$

following Cahn-Hilliard [37], with M and α being the double-well and surface energy parameters. Note the form of the surface energy term, the second term in equation 2.11, assumes isotropic interfacial energy with anisotropic generalizations possible; see [50] for example.

Finally, the evolution equation for twinning is obtained by following the time-dependent Ginzburg–Landau formalization [124]. For this, we assume mechanical equilibrium is reached much faster than twinning's equilibrium leading to a kinetic equation to describe twinning's time-dependent evolution,

$$\dot{\eta} = -L\,\delta_\eta W(\mathbf{F}^{\mathrm{e}}, \eta, \nabla\eta) \tag{2.12}$$

where δ_η represents a variational derivative, and L is a kinetic coefficient related to twin boundary mobility.

2.3 Combined twinning and dislocation models: pseudo-slip

Pseudo-slip is the main computational approach for coupling deformation twinning and dislocation slip in mesoscale simulations. This approach dates back to Kalidindi [91] and borrows ideas from crystal plasticity to track average twin volume fractions rather than fully resolving individual twins. Although this removes morphology details specific to twinning, it allows the quick and easy inclusion of twinning into existing full-field crystal plasticity models [7, 42, 43, 60, 61, 68, 148, 159]. Here we briefly explain the pseudo-slip model, adapted from Chang and Kochmann [42], which will be similar to the crystal plasticity model from Section 2.1 with slight modifications to include twinning. Finally, we will conclude the section by discussing alternative mesoscale computational models for capturing dislocation slip and deformation twinning.

2.3.1 Flow kinematics

The pseudo-slip model tracks the evolution of twin volume fractions through the variable $0 \geq \lambda \geq 1$, which will take a similar role to the plastic slip shear, γ, in crystal plasticity. The deformation gradient is multiplicatively decomposed into

$$\mathbf{F} = \mathbf{F}^{\mathrm{e}}\mathbf{F}^{\mathrm{in}}, \tag{2.13}$$

where now $\mathbf{F}^{\mathrm{in}}$ is the inelastic deformation gradient with combined contributions from plastic slip and deformation twinning. This decomposition assumes the order of twinning versus slip is unknown but instead occurs simultaneously [91], limiting the kinematic interactions between the two.

Modifying, the plastic velocity gradient from Section 2.1 we arrive at,

$$\tilde{\mathbf{L}}^{\mathrm{in}} = \dot{\mathbf{F}}^{\mathrm{in}}\mathbf{F}^{\mathrm{in}} = \tilde{\mathbf{L}}^{\mathrm{p}} + \tilde{\mathbf{L}}^{\mathrm{t}}, \tag{2.14}$$

where the inelastic velocity gradient is split into slip and twinning contributions. This split in the velocity further relies on the assumption that at the mesoscale, slip and twinning occur simultaneously. The plastic slip velocity gradient, $\tilde{\mathbf{L}}^{\mathrm{p}}$, is modified from equation 2.3 to account for dislocation activity on both the original, parent, slip systems and any twinned re-orientated slip systems (following concepts from Kalidindi [136] and Zhang and Joshi [159]),

$$\tilde{\mathbf{L}}^{\mathrm{p}} = \sum_{\alpha=1}^{N_s} \dot{\gamma}_{\alpha}^{\mathrm{p}} \left[\left(1 - \sum_{\beta=1}^{N_t} \lambda_{\beta}\right) \hat{\mathbf{b}}_{\alpha}^{\mathrm{p}} \otimes \hat{\mathbf{n}}_{\alpha}^{\mathrm{p}} + \sum_{\beta=1}^{N_t} \lambda_{\beta} \hat{\mathbf{b}}_{\alpha\beta}^{\prime\mathrm{p}} \otimes \hat{\mathbf{n}}_{\alpha\beta}^{\prime\mathrm{p}} \right], \tag{2.15}$$

where N_s and N_t are the number of slip and twin systems (respectively) present in the material, $(\hat{\mathbf{b}}_{\alpha}^{\mathrm{p}}, \hat{\mathbf{n}}_{\alpha}^{\mathrm{p}})$ are the slip systems on the parent lattice, and $(\hat{\mathbf{b}}_{\alpha}^{\prime\mathrm{p}}, \hat{\mathbf{n}}_{\alpha}^{\prime\mathrm{p}})$ are the twinned rotated slip systems. From crystallographic theory on deformation twinning (see Christian and Mahajan [49]), we can compute the twin-rotated slip systems as,

$$\hat{\mathbf{b}}_{\alpha\beta}^{\prime\mathrm{p}} = \mathbf{Q}_{\beta}\hat{\mathbf{b}}_{\alpha}^{\mathrm{p}}, \quad \hat{\mathbf{n}}_{\alpha\beta}^{\prime\mathrm{p}} = \mathbf{Q}_{\beta}\hat{\mathbf{n}}_{\alpha}^{\mathrm{p}}, \quad \text{with} \quad \mathbf{Q}_{\beta} = 2\hat{\mathbf{n}}_{\beta}^{\mathrm{t}} \otimes \hat{\mathbf{n}}_{\beta}^{\mathrm{t}} - \mathbf{I}, \tag{2.16}$$

using the twin plane normal $\hat{\mathbf{n}}_{\beta}^{\mathrm{t}}$, which along with the twin shear direction, $\hat{\mathbf{b}}_{\beta}^{\mathrm{t}}$, and shear magnitude $\gamma_{\beta}^{\mathrm{t}}$, describe the β twin system. Treating deformation twinning as a slip system, we can also arrive at its velocity gradient,

$$\tilde{\mathbf{L}}^{\mathrm{t}} = \sum_{\beta=1}^{N_t} \dot{\lambda}_{\beta}\gamma^{\mathrm{t}}\hat{\mathbf{b}}_{\beta}^{\mathrm{t}} \otimes \hat{\mathbf{n}}_{\beta}^{\mathrm{t}}. \tag{2.17}$$

Finally, combining equations 2.14, 2.15, and 2.17, we arrive at the full inelastic deformation update.

2.3.2 Energy and evolution equations

The equilibrium and evolution equations follow the crystal plasticity formulation, with the only difference being the augmentation of the twin energy and power terms. Here, we introduce the terms we amend and the resulting equations. The free energy will again be decomposed additively into,

$$W(\mathbf{F}^{\mathrm{e}}, \epsilon^{\mathrm{p}}, \lambda) = W^{\mathrm{e}}(\mathbf{F}^{\mathrm{e}}) + W^{\mathrm{p}}(\epsilon^{\mathrm{p}}) + W^{\mathrm{t}}(\lambda), \tag{2.18}$$

with the same elastic strain and plastic hardening energy and an additional twin hardening energy, $W^{\mathrm{t}}(\lambda)$. The dissipation potential will now have rate contributions for both slip and twinning, $\Psi^* = \Psi^{*\mathrm{p}}(\dot{\gamma}^{\mathrm{p}}) + \Psi^{*\mathrm{t}}(\dot{\lambda})$. The stationary point will now be with respect to both sets of internal variables leading to evolution equations,

$$\frac{\partial}{\partial \dot{\gamma}_\alpha^{\mathrm{p}}}\left(\dot{W} + \Psi^*\right) \ni 0 \qquad \text{and} \qquad \frac{\partial}{\partial \dot{\lambda}_\beta}\left(\dot{W} + \Psi^*\right) \ni 0 \tag{2.19}$$

$$-\tau_\alpha^{\mathrm{p}} + \frac{\partial W^{\mathrm{p}}}{\partial \dot{\gamma}_\alpha^{\mathrm{p}}} + \frac{\partial \Psi^*}{\partial \dot{\gamma}_\alpha^{\mathrm{p}}} \ni 0 \qquad \text{and} \qquad -\tau_\beta^{\mathrm{t}} + \frac{\partial W^{\mathrm{t}}}{\partial \dot{\lambda}_\beta} + \frac{\partial \Psi^{*\mathrm{t}}}{\partial \dot{\lambda}_\beta} \ni 0, \tag{2.20}$$

where τ_α^{p} and τ_β^{t} are the slip and twin resolved shear stresses on the α and β slip and twin system, respectively. Again, the evolution equations have a balance between the driving force (resolved shear stress) and strain/strain-rate hardening terms to determine the nucleation and propagation of each inelastic deformation mode.

2.3.3 Other approaches for combined twin and slip

The above pseudo-slip model aims to use efficient crystal plasticity implementations to describe twinning using average twin volume fractions within grains. Several crystal plasticity studies have aimed to expand the basic pseudo-slip model by including more necessary microscale physics to capture twin-slip interactions accurately. However, twinning's length scale is one major hurdle that needs to be added in most crystal plasticity-based twinning models. Although the physics of both twin and slip are discrete by nature, the characteristic size of deformation twins are much greater than that of dislocations [69, 71] and are often at the grain scale, as discussed in Section 1.1. This larger twin length scale means that although the length scale of dislocations allows for a homogenized representation within crystal plasticity methods, applying the same homogenized approximate representation for twinning is difficult. Thus, extensions to the crystal plasticity framework have been explored to account for an evolving twin interface, a few of which will be briefly mentioned here.

The first approach is a *discrete twin* evolution model, formulated by Ardelijan and Knezevic [12] and extended by several researchers [11, 47, 48]. The approach builds off of the classical crystal plasticity model to describe dislocation slip, with a separate twin model included to insert discrete twins. The twin model uses atomistic understandings of dislocation dissociation mechanisms to obtain an energy criterion for the nucleation of these discrete twins, along with stress-governed twin growth and propagation evolution equations. The second alternative approach is an *embedded deformation twinning* approach which uses weak discontinuities again in conjunction with a crystal plasticity model for dislocation slip. Jin *et al.* [87] developed the discrete twin model by building off existing shear band representations. Twin bands are inserted by assuming a jump in the velocity gradient (while continuity in velocity and displacement — motivated by velocity gradient flow rules in classical crystal plasticity models [99, 140]) and solving the resulting equilibrium equations across the interface to determine the local stress. A stochastic version of the resolved shear stress nucleation criteria, developed by Wang et al. [151], is utilized to dictate when discrete twins are embedded, along with length and thickness evolution equations. Both approaches' implementations can capture distinct twin bands in polycrystal specimens though at the cost of complex mesh manipulation, high computational costs during the insertion of rapidly forming twin bands, and a neglect of the twin surface energy.

A final extension explored for a few decades has been the phase field model for twinning, outlined in Section 2.2. Researchers have explored coupling phase field twinning with dislocation slip described using crystal plasticity. However, most early studies have focused on the single crystal scale or small strain limit. Only recently have studies focusing on the polycrystal scale with finite strains and complex twin-slip interactions [80, 97, 115, 139] been explored. These implementations can capture the complex twin morphology across several grains and explore texture influence. However, all these studies have only considered the presence of a single twin system, with the extension to multiple twin systems, by including several phase field variables left as a future a topic of interest.

Chapter 3

PHASE FIELD APPROACH TO TWINNING

3.1 Motivation

In recent decades there has been an increased interest in improving the performance of metallic alloys for various transportation, structural, and ballistic applications. Low symmetry metals, such as magnesium (Mg), zirconium (Zr), or titanium (Ti), exhibit excellent strength-to-weight ratios, making them ideal candidates for use in weight-crucial usages. While other classes of metals, such as cubic structured materials, for example, iron (Fe) or aluminum (Al), have high ultimate strengths, aiding their continual use in high-stress-strain situations. The first set of metals, Mg, Zr, and Ti, are under the class of hexagonal-close packed crystalline solids, which under even moderate deformation, exhibit complex inelastic deformations. The complex mechanisms result from the common inelastic deformation, dislocation slip, being less favorable when compared to deformation twinning. On the other hand, the second set of metals, Fe and Al, exhibit similar complex inelastic deformations in extreme strain or strain rate situations, where deformation twinning comes coupled with plastic slip. In either case, the successful implementation and improvement of many crystalline solids require suitable models to accurately describe, analyze and predict the complex inelastic material response.

The origin of these complex responses lies in the presence of deformation twinning, which adds several microscale complexities. Unlike slip, which involves the sliding of one plane of atoms over the other and is carried by dislocations or line defects, twins are planar defects across which a shear restores the lattice. Thus, unlike slip, which is typically more diffuse, twins manifest themselves as bands at the polycrystal scale, leading to length-scale effects distinct from slip. Further, twins involve a lattice rotation that interacts with anisotropic elasticity and dislocation slip's directional dependence. Finally, the shear in twinning has a specific sense (i.e., it can shear in one direction but not the other), while slip does not. Therefore, twinning can lead to an asymmetric response to imposed loading. We refer the reader to Mahajan and Christian [49] for a comprehensive introduction to twinning. The complexity is compounded by the interaction between slip and twinning, especially in polycrystal domains. Therefore, the interaction between twinning and slip in

crystalline materials has been a subject of interest in recent decades.

One line of work has focused on the atomistic scale where the energetics of twinning, nucleation of twins, the structure of twin boundaries, and the interaction of individual dislocations with a twin boundary are determined [38, 86, 110, 149, 156]. While these studies provide important insights and inputs to larger-scale models, they are insufficient to describe deformation morphology and overall macroscopic response.

There is also a large body of work at the polycrystalline scale. Since Kalidindi [91], various researchers [7, 42, 60, 61, 68, 148, 159] have studied the interaction between slip and twinning by treating twinning as a "pseudo-slip." Briefly, pseudo-slip does not seek to describe the morphology of individual twins but only an average twin volume fraction, allowing the incorporation of twins into full-field crystal plasticity or self-consistent studies of polycrystalline behavior. These studies have been invaluable in understanding the relationship between texture and the strength of the material. However, a detailed comparative study by Abdolvand and Daymond [2] on twinning in Zircaloy-2 between electron back-scatter diffraction (EBSD) observations and pseudo-slip based crystal plasticity simulations showed significant differences in the evolution of twins. Further, these models do not describe twins' morphology, which plays a critical role in material failure. The role of morphology, especially through the cooperative actions of grains, has been emphasized by several researchers [22, 129].

Phase-field models have long been used to study morphology in phase transitions (e.g., [14]). However, this has largely been in the context of small (geometrically linear) strains, which are inappropriate for deformation twins involving large shears and lattice rotations. Therefore, the phase-field approaches have also been extended to finite deformation in the context of twinning (e.g., [50]) and separately slip-based plasticity (e.g., [21]). Recently, Liu *et al.* [115] proposed a phase-field model that combines deformation twinning and plastic slip and used it to study single crystals in three dimensions and polycrystals in two dimensions. They emphasized the role of grain boundaries in twin nucleation and transmission into neighboring, poorly oriented grains. However, their model still uses an incremental update for the twinning deformation, borrowing from the pseudo-slip models. An alternate approach, by Jin *et al.* [87], inserted fully twinned regions (via strain discontinuities) when appropriate stochastic nucleation and propagation conditions were met. Two-dimensional polycrystal simulations correctly captured twin nucleation and propagation from grain boundaries under dynamic loading conditions. How-

ever, this model does not fully capture the nucleation and growth of twins and thus misses the full interaction with dislocations. Ardeljan and M. Knezevic [12] addressed this shortcoming by explicitly inserting discrete twin lamella based on total accumulated twin activity from pseudo-slip models while locally modifying the deformation history to account for the twinning shear. Several researchers have extended the model [11, 47, 48]; in particular, Cheng *et al.* [48] introduce discrete twin evolution with dislocation-motivated criteria and models for twin nucleation, propagation, and growth. However, all of these introduce twins in a discreet manner.

In this work, we develop a phase-field model to investigate the interactions between twinning and slip at the scale of multiple grains. We follow Mahajan and Christian [49] to describe deformation twinning and combine it with plastic slip. We incorporate general energetic and kinetic laws to describe nucleation barriers, surface energy, propagation drag, and rate hardening of twins and slip. We propose an implementation that is massively parallel and allows the use of graphical processing units (GPUs) to conduct large-scale studies. We first verify the implementation and subtle details of the phase field model through single crystal simulation. We then use the model and its implementation to conduct detailed studies in two-dimensional polycrystals with a single twin and slip system to provide insights into the interaction between the two deformation mechanisms. This work focuses on understanding the interaction and the resulting consequences of localized twin morphology on polycrystalline media in two dimensions, motivating future work in three dimensions with multiple twin and slip systems.

3.2 Model

We first describe the model for a single crystal with only one twin and slip system. At the end of the section, we will extend it to polycrystal domains, and in Chapter 4, we will further extend the model to include multiple twin and slip systems.

3.2.1 Kinematics

Consider a single crystal undergoing a deformation $\mathbf{y}$ from a stress-free reference configuration. We assume that the deformation gradient ($\mathbf{F} = \nabla\mathbf{y}$) is multiplicatively decomposed into elastic, plastic (related to slip), and twinning parts,

$$\mathbf{F} = \mathbf{F}^{\mathrm{e}}\mathbf{F}^{\mathrm{p}}\mathbf{F}^{\mathrm{t}}. \tag{3.1}$$

This decomposition naturally handles the situation where slip follows twinning at

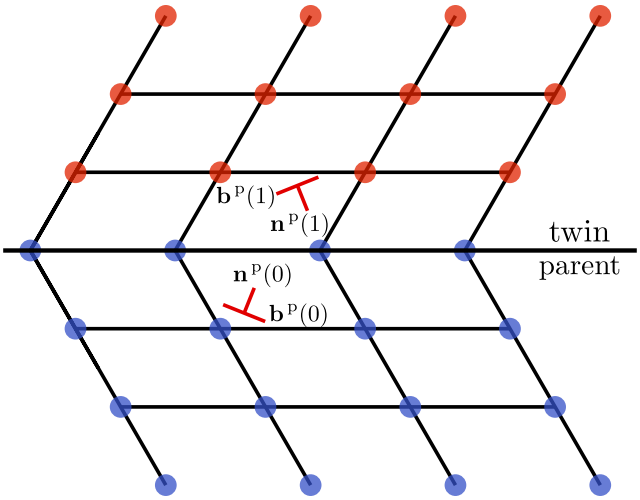

Figure 3.1: Twinning schematic. Parent and twinned lattice are shown with the respective dislocation slips in red.

any material point and matches the common decomposition within literature [60, 61, 87]. The other scenario, where twinning follows slip, requires the incorporation of transmutations and is ignored in this current work.

We assume that we have one twin system and one slip system. The *twin system* is characterized by a phase field variable η, twinning shear magnitude γ_0^{t}, twinning shear direction $\hat{\mathbf{b}}^{\mathrm{t}}$, twin plane normal $\hat{\mathbf{n}}^{\mathrm{t}}$, and twinning rotation $\mathbf{R}$. In this work, we consider a type I twin, so $\mathbf{R} = 2\hat{\mathbf{n}}^{\mathrm{t}} \otimes \hat{\mathbf{n}}^{\mathrm{t}} - \mathbf{I}$ is a two-fold rotation about the twin plane. The resulting twinning deformation is

$$\mathbf{F}^{\mathrm{t}}(\eta) = \mathbf{I} + \eta\, \gamma_0^{\mathrm{t}}\, \hat{\mathbf{b}}^{\mathrm{t}} \otimes \hat{\mathbf{n}}^{\mathrm{t}}, \tag{3.2}$$

where $\eta = 0$ in the untwinned region and $\eta = 1$ in the twinned region. We assume that $\eta \in H^1$ is smooth and changes from 0 to 1 in a narrow region with a corresponding interpolation of the twinning deformation. The *slip system* is characterized by the slip activity γ^{p}, slip direction $\hat{\mathbf{b}}^{\mathrm{p}}$ (respectively $\hat{\mathbf{R}}\hat{\mathbf{b}}^{\mathrm{p}}$), and glide plane normal $\hat{\mathbf{n}}^{\mathrm{p}}$ (respectively $\hat{\mathbf{R}}\hat{\mathbf{n}}^{\mathrm{p}}$) in the untwinned (respectively twinned) region, see Figure 3.1. The resulting plastic deformation evolves according to the classical flow rule; see [130] for example,

$$\dot{\mathbf{F}}^{\mathrm{p}} = \big(\dot{\gamma}^{\mathrm{p}} \hat{\mathbf{b}}^{\mathrm{p}}(\eta) \otimes \hat{\mathbf{n}}^{\mathrm{p}}(\eta)\big)\mathbf{F}^{\mathrm{p}}, \tag{3.3}$$

where $\hat{\mathbf{b}}^{\mathrm{p}}(\eta)$ and $\hat{\mathbf{n}}^{\mathrm{p}}(\eta)$ are unified descriptions of the plastic slip directions to capture the lattice dependence — i.e., whether the material point lies in the parent, twinned, or interface lattice.

The twin and slip directions description will be presented here for a simple two-dimensional case and extended to general three-dimensions later in Chapter 4. For the twin systems, we define the angle, θ^{t}, the shear direction $\mathbf{b}^{\mathrm{t}}$ makes with the horizontal and use trigonometry to then define $\mathbf{b}^{\mathrm{t}}$ and $\mathbf{n}^{\mathrm{t}}$. Similarly, we define $\theta^{\mathrm{p}}(\eta = 0)$ as the angle $\mathbf{b}^{\mathrm{p}}$ makes with the horizontal in the untwinned region. Rotating $\theta^{\mathrm{p}}(0)$ into the twinned domain we obtain $\theta^{\mathrm{p}}(1)$ and use the interpolation,

$$\theta^{\mathrm{p}}(\eta) = \eta\theta^{\mathrm{p}}(1) + (1-\eta)\theta^{\mathrm{p}}(0) \tag{3.4}$$

to obtain an unified description for $\mathbf{b}^{\mathrm{p}}(\eta)$ and $\mathbf{n}^{\mathrm{p}}(\eta)$.

Finally, we introduce the accumulated slip activity, ϵ^{p}, which evolves according to $\dot{\epsilon}^{\mathrm{p}} = |\dot{\gamma}^{\mathrm{p}}|$, and is used to govern plastic strain hardening. Note that $\eta \geq 0$ since twinning shear has a specific sense while γ^{p} can be both negative and positive since slip can lead to shear in either sense.

3.2.2 Free energy and stress

To derive evolution and equilibrium laws for the material, we postulate the free energy density to have the decomposition

$$W(\mathbf{F}^{\mathrm{e}}, \eta, \nabla\eta, \epsilon^{\mathrm{p}}) = W_{\mathrm{e}}(\mathbf{F}^{\mathrm{e}}, \eta) + \frac{\alpha}{2}\|\nabla\eta\|^2 + W_{\mathrm{t}}(\eta) + W_{\mathrm{p}}(\epsilon^{\mathrm{p}}), \tag{3.5}$$

where

$$W_{\mathrm{e}}(\mathbf{F}^{\mathrm{e}}, \eta) = \frac{1}{2}\mathbf{E}^{\mathrm{e}} : \mathbb{C}(\eta) : \mathbf{E}^{\mathrm{e}} \tag{3.6}$$

is the elastic energy density with non-linear strain measure $\mathbf{E}^{\mathrm{e}} = ((\mathbf{F}^{\mathrm{e}})^{\intercal}\mathbf{F}^{\mathrm{e}} - \mathbf{I})/2$ and (phase-dependent anisotropic) elastic modulus $\mathbb{C}(\eta)$.

$$W_{\mathrm{t}}(\eta) = \frac{M}{2}\eta^2(\eta-1)^2 \tag{3.7}$$

is a standard double-well potential and

$$\frac{\alpha}{2}\left\|\nabla\eta\right\|^2 \tag{3.8}$$

is an interfacial twin surface energy [50, 157]. The double-well parameter, M, and isotropic surface energy parameter, α, govern the phase-field variable, as described in Section 3.2.4.

$$W_{\mathrm{p}}(\epsilon^{\mathrm{p}}) = \sigma_{\infty}^{\mathrm{p}}\left[\epsilon^{\mathrm{p}} + \frac{\sigma_{\infty}^{\mathrm{p}}}{h}\exp\left(-h\frac{\epsilon^{\mathrm{p}}}{\sigma_{\infty}^{\mathrm{p}}}\right)\right] \tag{3.9}$$

describes the plastic self-hardening, similar to the Voce hardening law [7, 68], where $\sigma_{\infty}^{\mathrm{p}}$ is the ultimate stress and h is the hardening rate.

The first Piola-Kirchhoff stress is given by

$$\mathbf{P} = \frac{\partial W^{\mathrm{e}}}{\partial \mathbf{F}} = \frac{\partial W^{\mathrm{e}}}{\partial \mathbf{F}^{\mathrm{e}}}(\mathbf{F}^{\mathrm{p}}\mathbf{F}^{\mathrm{t}})^{-\intercal}. \tag{3.10}$$

3.2.3 Equilibrium and evolution

Mechanical equilibrium requires

$$\nabla\cdot\mathbf{P} = \mathbf{0}. \tag{3.11}$$

The evolution of the internal variables, γ^{p} and η, requires the introduction of a dual dissipation potential, $\Psi^*(\dot{\eta}, \dot{\gamma}^{\mathrm{p}})$, and the use of the principle of minimum dissipation potential [53] to obtain kinetic relations:

$$0 \in -\tau^{\mathrm{p}} + \frac{\partial W_{\mathrm{p}}}{\partial \epsilon^{\mathrm{p}}} + \partial_{\dot{\epsilon}^{\mathrm{p}}}\Psi^* \tag{3.12}$$

$$0 \in -\tau^{\mathrm{t}} + \frac{\partial W_{\mathrm{e}}}{\partial \eta} + \frac{\partial W_{\mathrm{t}}}{\partial \eta} - \alpha\nabla^2\eta + \partial_{\dot{\eta}}\Psi^*, \tag{3.13}$$

where τ^{p} and τ^{t} are the plastic and twin resolved shear stresses, respectively, defined as,

$$\tau^{\mathrm{p}} = \boldsymbol{\sigma}^{\mathrm{p}} : (\hat{\mathbf{b}}^{\mathrm{p}}\otimes\hat{\mathbf{n}}^{\mathrm{p}}), \quad \boldsymbol{\sigma}^{\mathrm{p}} = (\mathbf{F}^{\mathrm{e}})^{\intercal}\mathbf{P}\left(\mathbf{F}^{\mathrm{p}}\mathbf{F}^{\mathrm{t}}\right)^{\intercal}, \tag{3.14}$$

$$\tau^{\mathrm{t}} = \boldsymbol{\sigma}^{\mathrm{t}} : (\hat{\mathbf{b}}^{\mathrm{t}}\otimes\hat{\mathbf{n}}^{\mathrm{t}}), \quad \boldsymbol{\sigma}^{\mathrm{t}} = \gamma_0^{\mathrm{t}}\left(\mathbf{F}^{\mathrm{e}}\mathbf{F}^{\mathrm{p}}\right)^{\intercal}\mathbf{P}, \tag{3.15}$$

and physically correspond to driving forces for each inelastic mechanism, the remaining terms in Equations 3.12 – 3.13 correspond to different hardening terms contributing to the slip and twin yield stresses.

The dual potential accounts for the rate dependence of slip and twinning, which we postulate to be

$$\Psi^*\left(\dot{\gamma}^{\mathrm{p}}, \dot{\eta}\right) = \left[\tau_0^{\mathrm{p}}|\dot{\gamma}^{\mathrm{p}}| + \frac{\tau_0^{\mathrm{p}}\dot{\gamma}_0^{\mathrm{p}}}{m_{\mathrm{p}}+1}\left(\frac{|\dot{\gamma}^{\mathrm{p}}|}{\dot{\gamma}_0^{\mathrm{p}}}\right)^{m_{\mathrm{p}}+1}\right] + \left[\tau_0^{\mathrm{t}}|\dot{\eta}| + \frac{\tau_0^{\mathrm{t}}\dot{\gamma}_0^{\mathrm{t}}}{m_{\mathrm{t}}+1}\left(\frac{|\dot{\eta}|}{\dot{\gamma}_0^{\mathrm{t}}}\right)^{m_{\mathrm{t}}+1}\right], \quad (3.16)$$

based on the common approach within crystal plasticity literature [42, 43]. τ_0^{p} and τ_0^{t} are the critical resolved shear stresses, $\dot{\gamma}_0^{\mathrm{p}}$ and $\dot{\gamma}_0^{\mathrm{t}}$ the reference shear rates, and m_{p} and m_{t} are power rate hardening parameters for slip and twinning, respectively.

Note the dissipation potential Ψ^* is not continuously differentiable when $\dot{\gamma}^{\mathrm{p}} = 0$ or $\dot{\eta} = 0$ and therefore (3.12), (3.13) are formulated as differential inclusions. In particular, it means no evolution of the inelastic internal variables unless the resolved shear stress exceeds the critical yield values.

3.2.4 Twin interface thickness

The dependence of the twin interface thickness on material parameters is necessary to ensure sufficient mesh refinement is taken in simulations to match experimental observations of interfaces spanning a few atomic distances. The double-well energy, W_t, and gradient energy follow the Allen-Cahn model [9] and lead to a twin boundary whose thickness is on the order of $\sqrt{\alpha/M}$ and whose energy density is on the order of $\sqrt{\alpha M}$ per unit area.

We conduct several two-dimensional single-crystal simulations without dislocation slip (twinning is the only inelastic deformation present), with the values of α/M varying between simulations to determine the exact dependence of the interface thickness on material parameters. We find the interface thickness for each of these simulations by computing the distance over which η increases from 0.01 to 0.99 in a twin band. Figure 3.2 shows a linear trend between the computed twin interface thickness versus $\sqrt{\frac{\alpha}{M}}$. The resulting linear fit is also shown in Figure 3.2 and provides an estimate for the twin interface and resulting mesh refinement necessary for given material parameters.

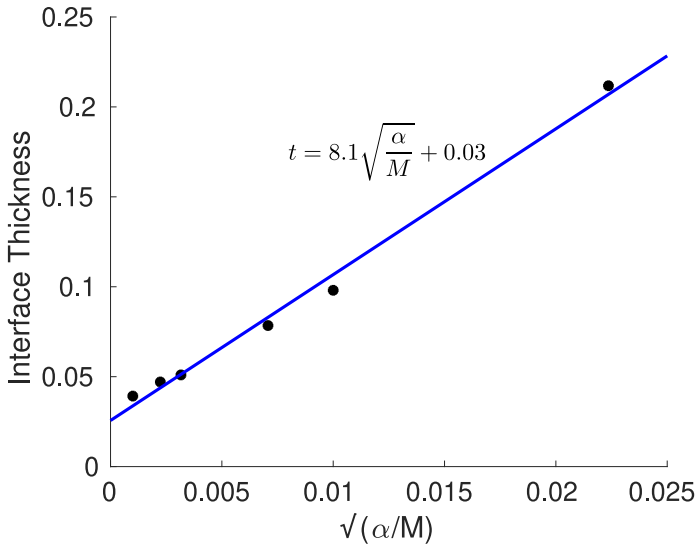

Figure 3.2: Twin interface thickness versus $\sqrt{\frac{\alpha}{M}}$ for displacement control simulations on a single crystals in the absence of plastic slip.

3.2.5 Twin nucleation and propagation

The twin evolution equation (3.13) becomes the equilibrium equation of [50] if we alternatively chose $\Psi^* = \Psi^*(\dot{\gamma}^{\mathrm{p}})$ and the time-dependent Landau Ginzburg equation of [124] if we take $\Psi^* = \Psi^*_{\mathrm{p}}(\dot{\gamma}^{\mathrm{p}}) + \nu/2|\dot{\eta}|^2$. We chose the form (3.16) because it provides both a critical stress τ^{t}_0 for the propagation of an existing twin boundary and a critical stress of $\tau^{\mathrm{t}}_0 + M/(6\sqrt{3})$ for twin nucleation. To see the latter, consider a material in the parent (untwinned) state, with a uniform $\eta = 0$, subjected to extremely slow loading. According to (3.13), η will evolve only when the resolved shear stress matches

$$\tau^{\mathrm{t}} = M\eta(\eta - 1)(2\eta - 1) + \tau^{\mathrm{t}}_0. \tag{3.17}$$

Thus, the nucleation of a twin, $\eta \to 1$, requires the resolved shear stress to overcome the maximum value of the first term (which is $M/(6\sqrt{3})$), in addition to τ^{t}_0.

We have confirmed this numerically by running several two-dimensional single-crystal simulations, again with plastic slip suppressed, the twinning rate hardening neglected ($\tau^{\mathrm{t}}_0 = 0$), and only M is varied. To explore the nucleation of twinning, the resolved shear stress (RSS), the driving force for twinning nucleation and growth, is computed at each load increment. Figure 3.3a shows the computed twinning RSS versus applied strain for different M parameters. We see that as the applied strain increases, the RSS increases until reaching a maximum point and then dropping.

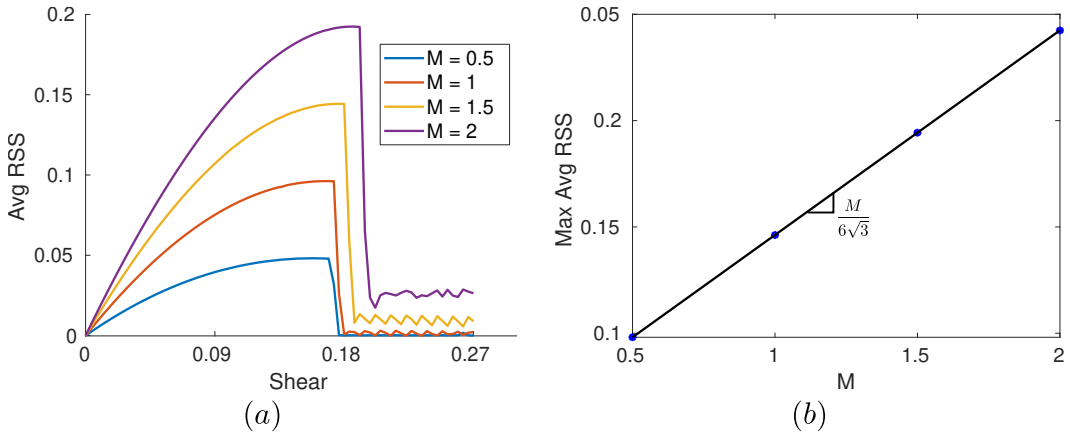

Figure 3.3: Twin resolved shear stress (RSS) (a) Twin RSS versus applied shear for varying M. (b) Twin length scale related critical RSS versus M.

The increasing RSS regime corresponds to η increasing uniformly throughout the domain. The sudden drop in the resolved shear stress corresponds to the complete formation of a twin band, i.e., $\eta \approx 0$ or $\eta \approx 1$ throughout the domain leading to the hardening term dropping to near 0. Hence, the maximum RSS corresponds to the nucleation stress required to overcome the length scale, i.e., τ_l^{t}. Figure 3.3b shows the maximum RSS versus M and through fitting we determine $\tau_l^{\mathrm{t}} = \frac{M}{6\sqrt{3}}$ consistent with our analysis.

In short, our twinning model provides a twin boundary energy $\sqrt{\alpha M}$ per unit area, critical stress for nucleation $\tau_0^{\mathrm{t}} + M/(6\sqrt{3})$, and a critical stress for propagation τ_0^{t}.

3.2.6 Polycrystal domains

The polycrystal is an assemblage of grains made of the same material but whose orientation differs from each other. We describe the texture of the polycrystal using the orientation function $\mathbf{Q}(\mathbf{X})$, that is, the rotation that takes the grain at $\mathbf{X}$ to a fiducial grain. The slip and twin systems in the grain $\mathbf{X}$ are now described by $\mathbf{Q}(\mathbf{X})\hat{\mathbf{b}}^{\mathrm{p}}, \mathbf{Q}(\mathbf{X})\hat{\mathbf{n}}^{\mathrm{p}}, \mathbf{Q}(\mathbf{X})\hat{\mathbf{b}}^{\mathrm{t}}, \mathbf{Q}(\mathbf{X})\hat{\mathbf{n}}^{\mathrm{t}}$ and the free energy density is similarly described as, $W(\mathbf{F}^{\mathrm{e}}, \eta, \nabla\eta, \epsilon^{\mathrm{p}}, \mathbf{X}) = W(\mathbf{F}^{\mathrm{e}}\mathbf{Q}(\mathbf{X}), \eta, \nabla\eta\mathbf{Q}(\mathbf{X}), \epsilon^{\mathrm{p}})$.

3.3 Implementation

We consider a periodic domain and prescribe a time-dependent average deformation gradient $\bar{\mathbf{F}}(t)$. So, $\mathbf{y} = \tilde{\mathbf{y}} + \bar{\mathbf{F}}\mathbf{X}$ where $\tilde{\mathbf{y}}$ is periodic, as are the rest of the kinematic quantities. We discretize the equilibrium equation (3.11) and evolution equations (3.12 and 3.13) in time using an implicit time discretization and rewrite them as

an incremental variational principle (e.g., [130]). We obtain the increment in the deformation gradient, twin, and slip as the solution to the variational problem,

$$\mathbf{y}_{n+1}, \eta_{n+1}, \gamma^{p}_{n+1} = \arg\min \int_{\Omega} \left(W(\nabla \mathbf{y}, \eta, \nabla \eta, \epsilon^{p}, \mathbf{X}) + \Delta t \Psi^{*}\left(\frac{\Delta \gamma^{p}}{\Delta t}, \frac{\Delta \eta}{\Delta t} \right) \right) d\Omega, \tag{3.18}$$

and the increment in plastic strain is

$$\mathbf{F}^{p}_{n+1} = \frac{1}{J^{d}_{p}} \left(\mathbf{I} + \Delta \gamma^{p} \hat{\mathbf{b}}^{p} \otimes \hat{\mathbf{n}}^{p} \right) \mathbf{F}^{p}_{n}. \tag{3.19}$$

where $J_{p} = \det\left(\mathbf{I} + \Delta \gamma^{p} \hat{\mathbf{b}}^{p} \otimes \hat{\mathbf{n}}^{p} \right)$ is used to normalize for an isochoric plastic deformation, d is the dimension (2 or 3), and subscripts $n+1$ and n represent current and previous time steps values of variables.

We solve the variational problem following the accelerated computation micromechanics approach [160]. The basic idea is to use both deformation $\mathbf{y}$ and its gradient $\mathbf{F}$ as independent variables and to similarly use both the twin phase-field, relabeled β, and its gradient $\nabla \eta$ as independent variables. We then treat the compatibility between the deformation/twin phase field and their respective gradients as a constraint that is implemented using an augmented Lagrangian. So we consider the augmented functional

$$\int_{\Omega} \left(W(\mathbf{F}, \beta, \nabla \eta, \epsilon^{p}, \mathbf{X}) + W_{\lambda}(\mathbf{F}, \nabla \mathbf{y}, \beta, \eta) + \Delta t \Psi^{*}\left(\frac{\Delta \gamma^{p}}{\Delta t}, \frac{\Delta \beta}{\Delta t} \right) \right) d\Omega, \tag{3.20}$$

where

$$W_{\lambda}(\mathbf{F}, \mathbf{y}, \eta, \beta) = \lambda_{F} : (\mathbf{F} - \nabla \mathbf{y}) + \lambda_{\eta}(\beta - \eta) + \frac{\rho_{F}}{2} \|\mathbf{F} - \nabla \mathbf{y}\|^{2} + \frac{\rho_{\eta}}{2} \|\beta - \eta\|^{2}. \tag{3.21}$$

Here, $\rho_{F} > 0, \rho_{\beta} > 0$ are fixed penalty constants and λ_{F} and λ_{η} are Lagrange multipliers. We now have a saddle point problem where we minimize the functional over $\mathbf{F}, \mathbf{y}, \eta, \beta$ and maximize over the Lagrange multipliers $\lambda_{F}, \lambda_{\eta}$. We use the alternating direction method of minimizers (ADMM), shown in Algorithm 1, to update our variables each time step.

A brief outline of the algorithm and reasoning is given here. We first use ADMM to update the twinning phase field variables ($\nabla \eta$, β) until twin dual and prime convergence. We then update the deformation variables ($\mathbf{y}$, $\mathbf{F}$) and the slip magnitude γ^{p}.

Finally, we alternate updating the twin phase field (inside a sub-ADMM algorithm), deformation gradient, and slip variables until the deformation prime and dual norms converge. We separately update the twin variables to resolve it before updating the total deformation and plastic slip. Although we can include the twinning sub-algorithm in the main loop, we found better convergence and behavior with this split, particularly when the phase parameter rapidly evolves.

The algorithm is known to converge for sufficiently large ρ_F, ρ_β, though too large values slow down the convergence. We use periodic boundary conditions and fast Fourier transforms (FFT) to solve the Helmholtz projections (steps 1ii and 3). This algorithm is known to perform well relative to other FFT-based algorithms but has the significant benefit of an easy parallel implementation. Steps 1i, 2, and 5 are local nonlinear problems solved in parallel using the steepest gradient descent or Newton-Raphson methods. Steps 1ii and 3 are Helmholtz projections for which there are efficient parallel algorithms. Finally, steps 1iii, 1iv, 4, and 6 are simple updates. Thus the entire iterative algorithm is implemented in parallel using Graphical Processing Units (GPUs), with Central Processing Units (CPUs) only necessary for initialization and saving data after each time step. GPUs provide thousands of cores for accelerated computations, allowing us to sufficiently refine the twin morphology while running simulations across several grains.

Finally, we discretize the domain using a uniform spacial grid to implement the method. The grid must be fine enough that we sufficiently resolve the details of the twin boundary and the deformation within individual grains, i.e., $\frac{L}{\sqrt{N_g}} \gg 8\sqrt{\frac{\alpha}{M}} \gg \frac{L}{N}$ where L is the size of the domain, N is the spatial discretization, and N_g is the number of grains.

3.4 Model verification and exploration

The model presented in Section 3.2 and our numerical implementation were tested extensively in incremental levels of complexity, i.e., exploring the presence of a single inelastic deformation in either single crystal or polycrystal domains. We compared the nucleation and propagation of each inelastic deformation for each case with our theoretical understanding.

Algorithm 1: Alternating direction method of minimizers (ADMM) algorithm for phase field twin and slip updates

Data: $\mathbf{F}_n$, $\mathbf{y}_n$, η_n, β_n, γ_n, λ_{Fn}, $\lambda_{\eta n}$, and $\bar{\mathbf{F}}_{n+1}$
Result: $\mathbf{F}_{n+1}$, $\mathbf{y}_{n+1}$, η_{n+1}, β_{n+1}, γ_{n+1}, λ_{Fn+1}, $\lambda_{\eta n+1}$
$\mathbf{F}^{(0)} \leftarrow \mathbf{F}_n$, $\mathbf{y}^{(0)} \leftarrow \mathbf{y}_n$, $\gamma^{\mathrm{p},(0)} \leftarrow \gamma_n^{\mathrm{p}}$, $\lambda_F^{(0)} \leftarrow \lambda_{Fn}$;
$i \leftarrow 0$;
while $r_{F,p} \geq r_{F,d}^{tol}$ *or* $r_{F,p} \geq r_{F,d}^{tol}$ **do**
  $\beta^{(0)} \leftarrow \beta_n$, $\eta^{(0)} \leftarrow \eta_n$, $\lambda_\eta^{(0)} \leftarrow \lambda_{\eta n}$;
  $j \leftarrow 0$;
  1. ADMM for twinning phase field;
  while $r_{\eta,p} \geq r_{\eta,d}^{tol}$ *or* $r_{\eta,p} \geq r_{\eta,d}^{tol}$ **do**
    i. Solve for $\beta^{(j+1)}$ from the local problem:
    $\partial_\beta W(\mathbf{F}^{(i)}, \beta^{(j+1)}, \nabla\eta^{(j)}, \epsilon^{\mathrm{p},(i)}) + \Delta t \partial_\beta \Psi^*(\beta^{(j+1)}) + \lambda_\eta^{(j)} + \rho_\eta(\beta^{(j+1)} - \eta^{(j)}) = 0$;
    ii. Solve for $\eta^{(j+1)}$ from Helmholtz projection of twin phase field variable: $\nabla^2\eta^{(j+1)} - \frac{\rho_\eta}{\alpha}\eta^{(j+1)} = -\frac{1}{\alpha}\left(\lambda_\eta^{(j)} + \rho_\eta\beta^{(j+1)}\right)$;
    iii. Update twin lagrange multiplier ($\lambda_\eta^{(j+1)}$):
    $\lambda_\eta^{(j+1)} = \lambda_\eta^{(j)} + \rho_\eta(\beta^{(j+1)} - \eta^{(j+1)})$;
    iv. Compute twinning primal and dual feasibility:
    $r_{\eta,p} = \left\|\beta_{j+1} - \eta_{j+1}\right\|_{L^2}$, $r_{\eta,d} = \rho_\eta / M \left\|\eta_{j+1} - \eta_j\right\|_{L^2}$;
    $j \leftarrow j + 1$
  end
  2. Solve for $\mathbf{F}^{(i+1)}$ from deformation local problem
  $\partial_F W(\mathbf{F}^{(i+1)}, \beta^{(j+1)}, \nabla\eta^{(j+1)}, \epsilon^{\mathrm{p},(i)}) + \lambda_F^{(i)} + \rho_F(\mathbf{F}^{(i+1)} - \nabla\mathbf{y}^{(i)}) = 0$;
  3. Solve for $\mathbf{y}^{(i+1)}$ from Helmholtz projection of deformation variables:
  $\nabla^2\mathbf{y}^{(i+1)} = \nabla \cdot \left(\mathbf{F}^{(i+1)} + \dfrac{\lambda_F^{(i)}}{\rho_F}\right)$;
  4. Update deformation lagrange multiplier ($\lambda_F^{(i+1)}$):
  $\lambda_F^{(i+1)} = \lambda_F^{(i)} + \rho_\eta(\mathbf{F}^{(i+1)} - \nabla\mathbf{y}^{(i+1)})$;
  5. Update slip shear magnitude $\gamma^{\mathrm{p},(i+1)}$:
  $\partial_{\gamma^{\mathrm{p}}} W(\mathbf{F}^{(i+1)}, \beta^{(j+1)}, \nabla\eta^{(i)}, \epsilon^{\mathrm{p},(j+1)}) + \Delta t \partial_{\gamma^{\mathrm{p}}} \Psi^*(\gamma^{\mathrm{p},(i+1)}) = 0$;
  6. Compute deformation primal and dual feasibility:
  $r_{F,p} = \|\mathbf{F}_{i+1} - \nabla\mathbf{y}_{i+1}\|_{L^2}$, $r_{F,d} = \rho_F/\mu \|\nabla\mathbf{y}_{i+1} - \nabla\mathbf{y}_i\|_{L^2}$.;
  $i \leftarrow i + 1$
end

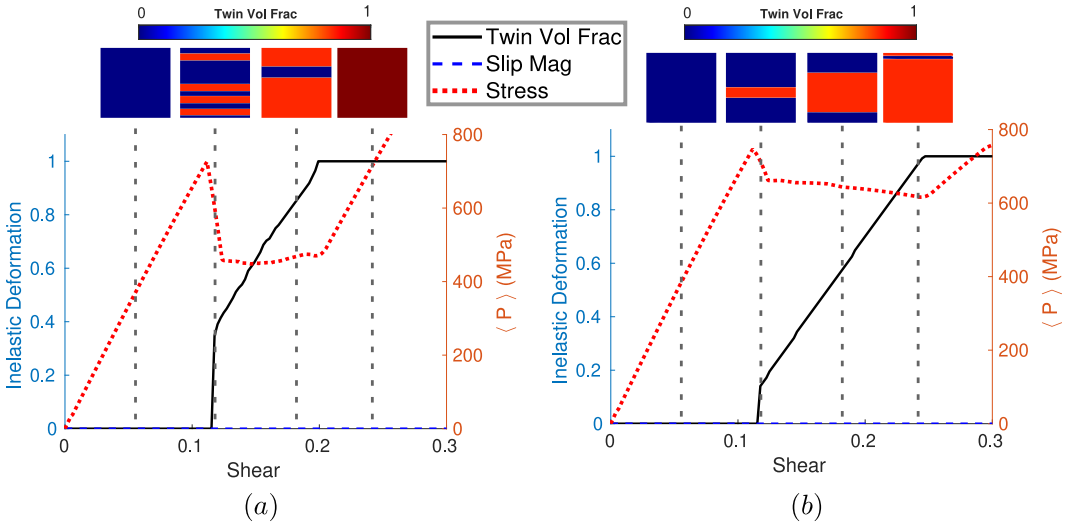

Figure 3.4: Monocrystal twinning simulations. Average shear stress (dotted red line) and twin volume fraction (solid black line) versus applied strain for simple shear along (a) vertical and horizontal unit cell axes and (b) $\pi/8$ rotated axes of the unit cell. Twin microstructure plots are shown for a few representative times.

3.4.1 Single crystal simulations

Deformation twinning

First, we considered only elasticity and twinning with the plastic slip internal variable suppressed, i.e., the evolution law was prevented from activating. We selected a single crystal domain of size $L = 20$ μm with a simple shear deformation applied along different directions. The twinning parameters used are $M = 1$ GPa, $\alpha = 4 \times 10^{-7}$ Pa$\cdot$ m^2, $\tau_0^{\mathrm{t}} = 2$ MPa, and $\gamma_0^{\mathrm{t}} = 0.129$, which following Section 3.2.5, would indicate a nucleation threshold stress of 98.2 MPa and propagation threshold of 2 MPa. Figure 3.4 shows the resulting stress-strain response (dashed red) and the twin volume fraction (solid black) for the case of (a) applied shear aligned with twin shear direction and (b) applied shear and twin shear direction rotated by 22.5°. We show representative twin microstructure snapshots above each plot.

We observe that both Figure 3.4 (a) and (b) have a significant linear elastic region since slip is suppressed and twinning has a large nucleation threshold until twin bands form, after which there is a stress drop due to the formation of a twin band. As the shear increases, the twin bands grow until the entire crystal has fully twinned, and the material begins to behave elastically again. Focusing on Figure 3.4 (a), where the applied shear and twin direction are aligned, we measure the point of twin nucleation to correspond to $P_{\mathrm{nuc}} = 758$ MPa shear stress and $\gamma_{\mathrm{nuc}} = 0.1164$ shear

strain. From these nucleation values, we can compute the twin resolved shear stress for this simple single crystal case as,

$$\tau^{\mathrm{t}} = \gamma_0^{\mathrm{t}} P_{\mathrm{nuc}} = 97.8 \text{ MPa}, \tag{3.22}$$

which closely matches the theoretical nucleation threshold discussed in Section 3.2.4. Lastly, looking at Figure 3.4 (b), we measure a slightly larger nucleation stress ($P_{\mathrm{nuc}} = 779$ MPa) due to the slight misalignment between the shear and twin directions.

Plasticity Second, the plastic slip was activated while suppressing twinning evolution. Simple shear deformations along different directions were applied to a single crystal domain of size $L = 20\,\mu$m again. The slip parameters used for the simulations were $\tau_0^{\mathrm{p}} = 50$ MPa and $\sigma_\infty^{\mathrm{p}} = 50$ MPa which would correspond to an initial yield stress 50 MPa and a final yield stress 100 MPa. Figure 3.5 shows the resulting slip resolved shear stress versus applied shear for simulations with different loading directions (0, $\frac{\pi}{8}$, $\frac{\pi}{4}$, $\frac{3\pi}{8}$, and $\frac{\pi}{2}$). We plot each simulation case's final slip magnitude distribution next to the RSS plot in Figure 3.5 with the border matching the specific simulation.

From Figure 3.5, we observe that each slip-resolved shear stress approaches $\sim$ 100 MPa as expected based on the parameters. Furthermore, we see that simulations $\psi = 0$ and $\frac{\pi}{2}$ reach the final yield stress first since they correspond to the best alignment between the slip applied shear direction, while the $\psi = \frac{\pi}{4}$ takes the longest since it is the least aligned requiring large rotations to occur before yielding. Lastly, we observe nearly uniform plastic slip magnitudes in each crystal since no heterogeneity is introduced from elasticity or twinning.

Twinning and plasticity Finally, a combination of one slip and twin system, with an angle of 45° between the two systems, was tested in single crystals for various load alignments. The twin and slip parameters are the same as the previous sets of simulations. Figure 3.6 shows the average stress, slip magnitude, and twin volume fraction versus applied shear along (a) the twin system, (b) between the twin and slip system, and (c) the slip system. Twin volume fraction and slip magnitude microstructure snapshots are shown at a few time steps above and below (respectively) the stress-strain curves.

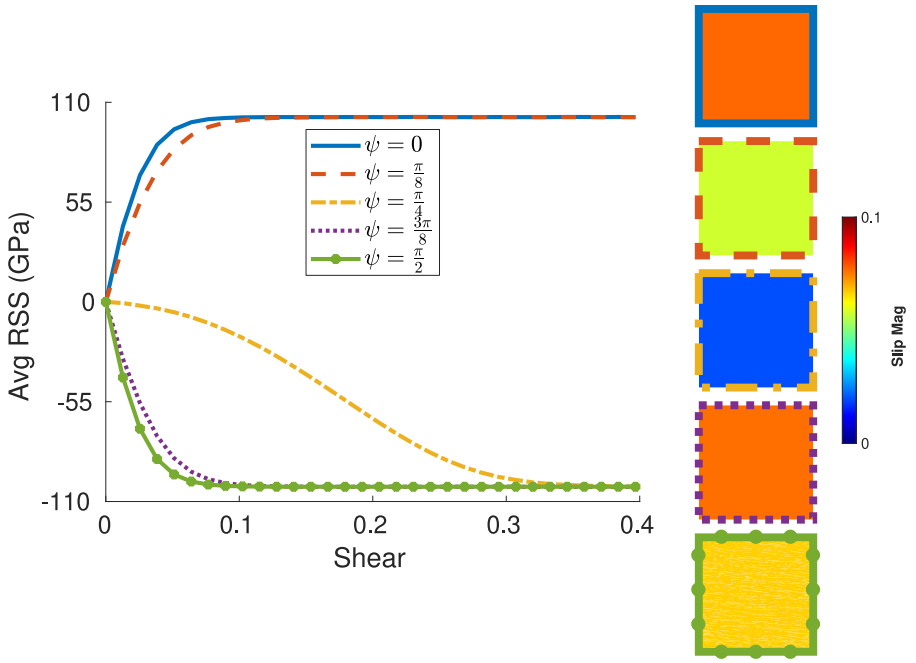

Figure 3.5: Monocrystal plasticity simulations. Plastic resolved shear stress versus strain for different crystal orientations, ψ is the relative angle between slip system and shear directions. Slip morphology at the final loading step are shown with border color and line type matching the stress curves.

Focusing on Figure 3.6 (b), when the applied shear is aligned between the twin and slip systems, we observe two regions. Region 1 corresponds to the early strains before twinning nucleates and slip is dominant. We see this with a gradually increasing slip magnitude and no twin volume fraction. In Region 2, twinning has nucleated in the form of thick bands; note that thick bands form due to the misalignment of the twin and loading. Incorporating a twinning rotation and sharp interfaces leads to slip arrest in the twin bands due to a now less favorable rotated slip system and slip accumulation outside the bands due to stress concentrations from the interface allowing slip propagation. We can also see this with a jump in the slip magnitude and the slip microstructure images showing bright spots in the untwinned regions. The other load cases, twin aligned in Figure 3.6 (a) and slip aligned in Figure 3.6 (c), show similar trends with now earlier twin (slip) nucleation and less slip (twin) deformations, respectively.

3.5 Twin-slip interactions in 2D polycrsytal material

We now present results highlighting various aspects of microstructure evolution and the interplay between slip and twinning in a model two-dimensional polycrystalline

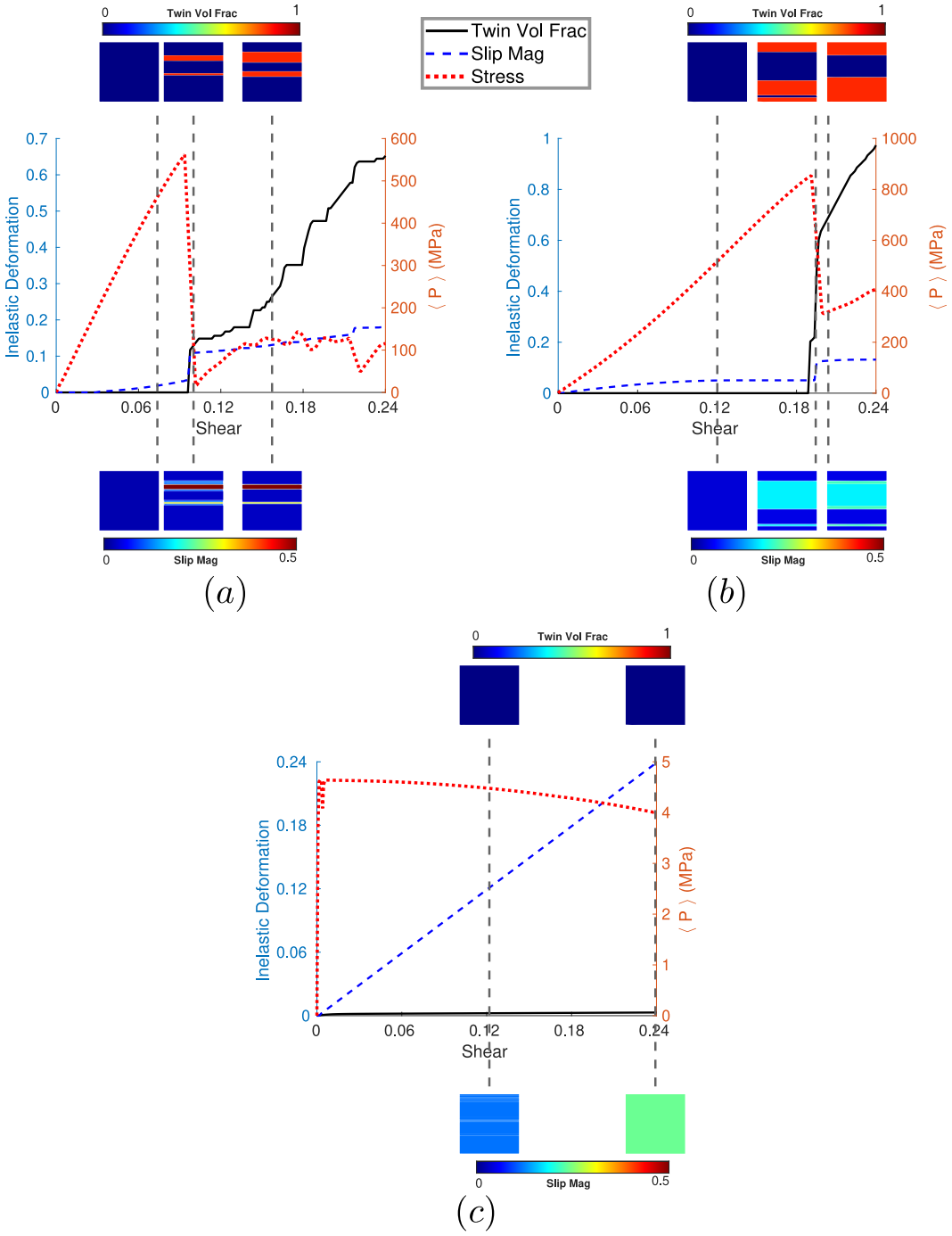

Figure 3.6: Monocrystal twin-slip simulations. Average stress (dotted red curve), slip magnitude (dashed blue curve), and twin volume fraction (solid black curve) versus applied shear strain for loading along (a) the unit cell axes (aligned with twin directions), (b) $\pi/8$ rotated axes of the unit cell (aligned with neither) and (c) $\pi/4$ rotated axes of the unit cell (aligned with slip).

Parameter	Value	Significance	Reference
Elastic Parameters			
λ_1	25 GPa	Stiffness C_{1111}	[150]
λ_2	15 GPa	Stiffness C_{1122}	[150]
μ	15 GPa	Stiffness C_{1212}	[150]
Twinning Parameters			
M	80 MPa	Double well	–
α	8×10^{-8} Pa$\cdot$ m^2	Surface energy	[98, 109, 151]
γ_0^{t}	0.129	Shear magnitude	[150]
$\dot{\gamma}_0^{\mathrm{t}}$	1.0 $1/s$	Reference shear rate	[150]
m_{t}	1.0	Rate hardening	[150]
τ_0^{t}	1 MPa	Critical RSS	[43]
θ^{t}	$-\frac{\pi}{8}$	Twin shear angle	–
Plasticity Parameters			
m_{p}	0.05	Rate hardening	[42]
$\dot{\gamma}_0^{\mathrm{p}}$	1.0 $1/s$	Reference shear rate	[42]
τ_0^{p}	4 MPa	Critical RSS	[42]
σ^{∞}	2 MPa	Ultimate stress	[42]
h	7.1 GPa	Hardening rate	[42]
θ^{p}	$\frac{\pi}{8}$	Slip shear angle	–

Table 3.1: Material parameters used for two-dimensional polycrystal simulations.

system. Material parameters are given in Table 3.1, unless otherwise specified, and are motivated by basal slip and tension twinning in magnesium, which is known to have profuse twinning. We conduct calculations on a 1024×1024 grid on a domain of length, $L = 80\mu$m, allowing us to resolve our twin boundaries to a size of ~ 150 nm.

3.5.1 Typical results

We consider a polycrystal of 30 grains, shown in Figure 3.7(a), obtained by Voronoi tessellation [64] from random seeds and sample the orientations from a uniform distribution between $\pm\frac{\pi}{2}$. We have verified that the results are typical for this texture by considering other samples. We apply a boundary condition corresponding to a simple shear along the horizontal axis at a strain rate of 1.0×10^{-2} until a maximum shear strain of 0.1. The stress-strain behavior, bulk slip activity, and twin volume

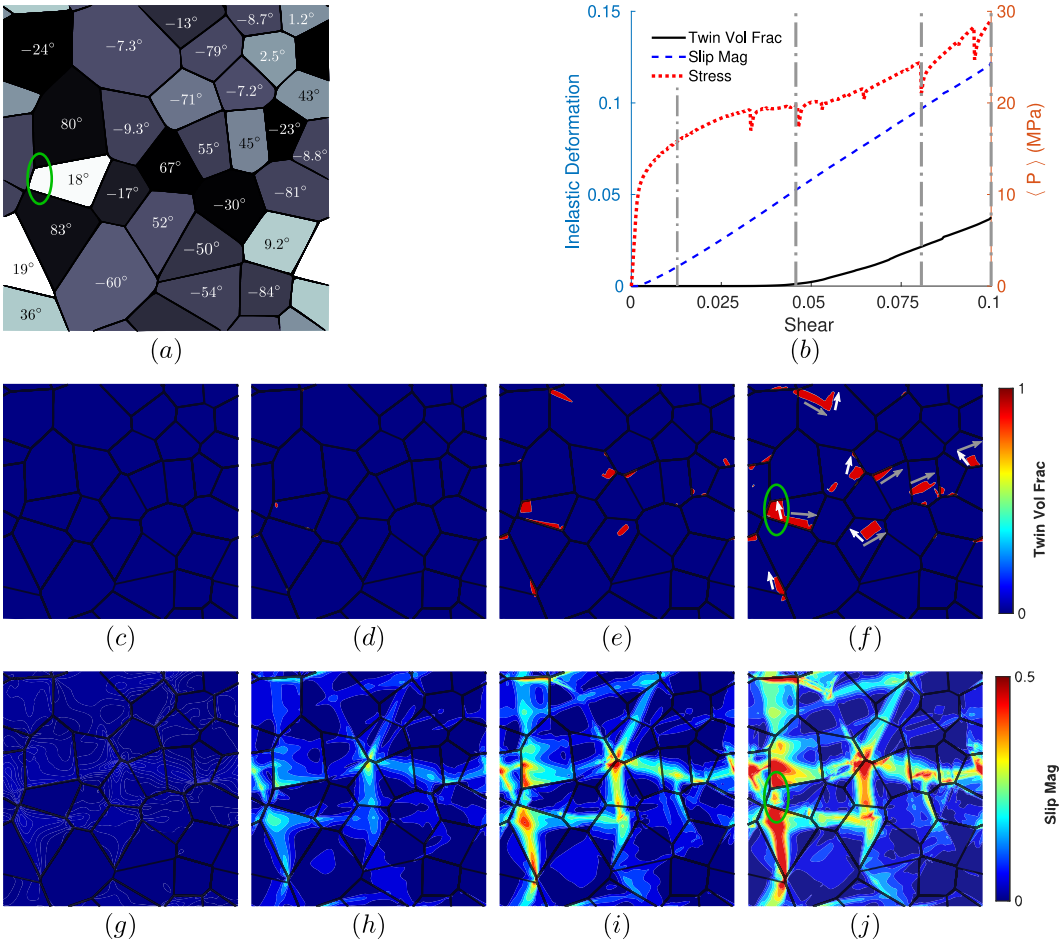

Figure 3.7: Deformation of polycrystalline specimen subjected to simple shear. (a) The polycrystalline specimen. The grayscale shows the propensity for twinning and slip. The darker grains are favorably oriented for slip and lighter grains for twinning, while the numbers indicate the grain orientation. (b) Stress-strain behavior and evolution of average slip magnitude and twin volume fraction. Vertical dashed lines indicate points at which microstructure is shown. (c–f) Snapshot of twin volume fraction (η) at strains of $\gamma = 0.01, 0.044, 0.07, 0.1$. Gray and white arrows show twin and reciprocal twin directions, respectively. (g–j) Snapshots of accumulated slip magnitude (ϵ^{p}) at strains of $\gamma = 0.01, 0.044, 0.07, 0.1$.

fraction are shown in Figure 3.7(b). Snapshots of the spatial evolution of twinning and slip are shown in Figure 3.7(c–f) and 3.7(g–j), respectively.

As loading begins, the response is initially elastic till the applied strain reaches a value of about $\gamma = 0.01$. At this point, plastic slip initiates across several grains — Figure 3.7(g) — and is accompanied by stress softening. The intensity of plastic activity increases with bands forming across grains till an applied strain of $\gamma = 0.04$, at which point twinning begins to nucleate — Figure 3.7(d). As the loading continues

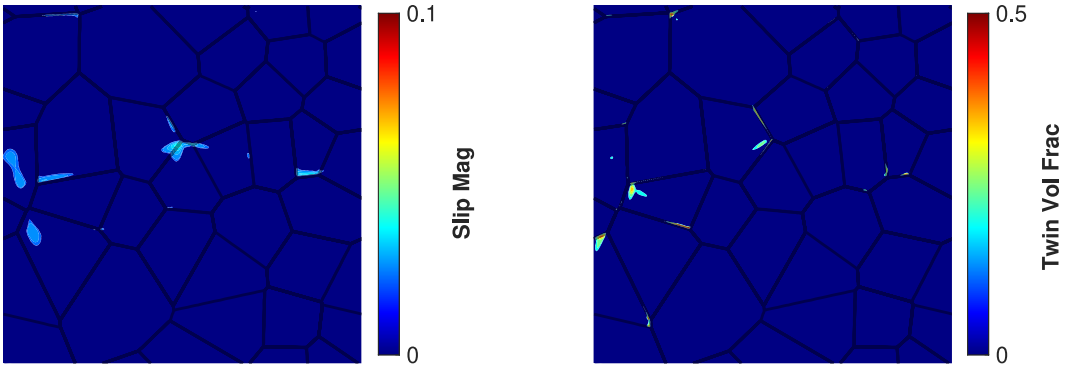

Figure 3.8: Nucleation. (a) Slip nucleation at $\gamma = 0.01$. (b) Twin nucleation at $\gamma = 0.04$.

increasing, existing twins grow, new twins appear, and the slip intensity grows. This twinning propagation is accompanied by further softening. Note that there are multiple minor load drops as micro-twins nucleate, but these quickly recover as the twins are pinned by either grain boundaries or plastic zones. Importantly both slip and twinning proceed as bands within favorable grains. Further, the twin boundaries are oriented according to the expected twin and reciprocal twin boundary orientations (indicated by gray and white arrows, respectively, in Figure 3.7(f)).

Propensity for slip and twinning The propensity, p, of the inelastic deformations is computed using the applied average deformation, $\bar{\mathbf{F}}$, local twin shear and normal directions, $\hat{\mathbf{b}}^{\mathrm{t}}$ and $\hat{\mathbf{n}}^{\mathrm{t}}$, and local slip shear and normal directions, $\hat{\mathbf{b}}^{\mathrm{p}}$ and $\hat{\mathbf{n}}^{\mathrm{p}}$, as follows:

$$p = \left[\bar{\mathbf{F}} : \mathrm{sym}(\hat{\mathbf{b}}^{\mathrm{t}} \otimes \hat{\mathbf{n}}^{\mathrm{t}})\right]_{+} - \left|\bar{\mathbf{F}} : \mathrm{sym}(\hat{\mathbf{b}}^{\mathrm{p}} \otimes \hat{\mathbf{n}}^{\mathrm{p}})\right|. \tag{3.23}$$

The operation $[\cdot]_{+}$ projects to the positive real axis, which is required to capture the asymmetry of twinning. The absolute value for the slip term captures its bidirectional behavior. The resulting values of $p \in (-1, 1)$ are plotted in Figure 3.7(a), with -1 indicating alignment with slip and 1 corresponding to alignment with twinning. Comparing the propensity values in Figure 3.7(a) to the final twin and slip configuration, Figure 3.7(f) and (j), we observe both slip and twinning dominating in the respective dark and light grains. However, there are still instances where the less preferable system is present inside a grain, indicating the highly heterogeneous interaction between the inelastic and anisotropic elasticity.

Nucleation The anisotropy of elastic moduli in each grain gives rise to a heterogeneous distribution of elastic moduli across the polycrystalline specimen. Consequently, the state of stress in the initial elastic phase is highly heterogeneous, with stress concentrations at grain boundaries. These stress concentrations lead to small amounts of slip occurring early in the loading. We see the first emergence of macroscopically significant slip at $\gamma = 0.01$; this is highlighted in Figure 3.8(a), which reproduces the results of Figure 3.7(g) with a magnified scale. We notice that higher levels of slip are concentrated at triple junctions of grains with a high degree of reorientation between the grains. In other words, slip nucleates near the triple junctions. This is also true for twinning, as seen in Figure 3.8(b), which shows results with a magnified scale at a strain of $\gamma = 0.04$, a time shortly before Figure 3.7(d). Thus, the elastic anisotropy leads to stress risers that enable nucleation at triple junctions.

Bridging Twinning can provide a bridge for a slip band to extend across a grain poorly oriented for slip activity. We highlighted this bridge by a circle in Figure 3.7(a), (f), and (j), which provides further evidence of the nonlocal nature of morphology and the interplay between inelastic deformation mechanisms.

Geometrically necessary dislocations The cooperative bridging of inelastic deformations across grains points to the role of kinematic compatibility of the inelastic deformations in driving the cooperative interaction between grains. In plasticity, Nye's dislocation tensor or the curl of the plastic deformation gradient describes the geometrically necessary dislocations — dislocations that are necessary to overcome the incompatibility of the plastic deformation [90, 127]. Figure 3.9 shows the magnitude of the curl of the slip, twinning, and combined inelastic deformations — we may regard them as geometrically necessary slip, twinning, and inelastic dislocations. We see a large density at grain boundaries where twin/slip bands kink or where dislocations bridge twin bands. We also see some twinning dislocations along twin boundaries as they may not be perfectly aligned.

Fluctuations The role of heterogeneity or fluctuations in slip and twin evolution is illustrated in Figure 3.10. Figure 3.10(a–c) displays heat maps of twin and slip activity versus local orientation, with the colors indicating the number of points active at that orientation and level of activity. We see large twin volume fractions and slip activity centered around favorable orientations, 22.5° for twinning and

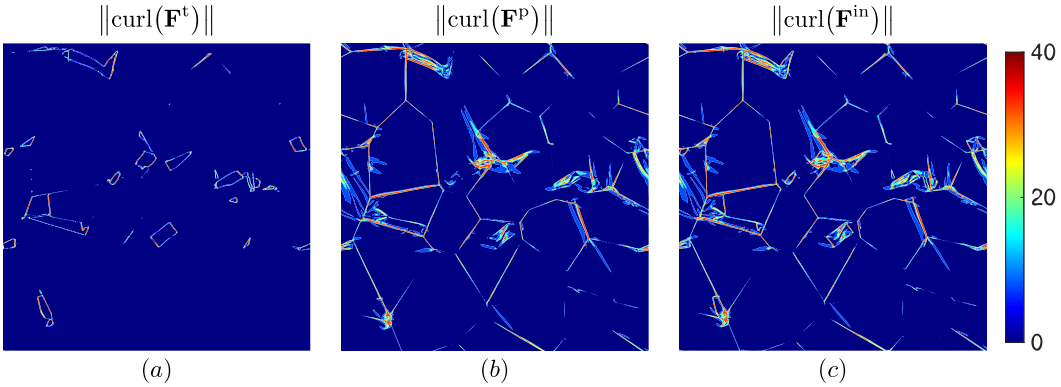

Figure 3.9: Geometrically necessary dislocation density. Magnitude of the curl of (a) twinning, (b) plastic slip, and (c) inelastic (plastic and twinning) deformations.

both 22.5° and −22.5° for slip. However, the activation for both spread across to more unfavorable grains. Additionally, we see a range of twin fraction and slip activity present at each orientation, indicating that the twin and slip activity can differ drastically in similarly orientated grains. Figure 3.10(d) and (e) show the cumulative histogram of the active inelastic systems versus the nominal driving force, computed by projecting the macroscopic load onto the local orientation. The histograms illustrate that the activation of slip and twinning is centered "near" their critical values, ±4MPa for slip and 9MPa for twinning. However, the peaks are shifted due to the rate dependence, hardening, and stress fluctuations. Further, we see the activation of twin/slip at various driving force values, even those close to zero or negative. These results illustrate that average values of micro-mechanical fields are insufficient to describe the complex behavior shown here.

Comparison with experimental observations The implementation presented in this work is in two dimensions; therefore, we can only compare the results of these simulations to experiments in a qualitative manner. Nonetheless, several qualitative results agree with experimental observations in hcp materials. First, Figure 3.7 shows that the current model predicts twins nucleating and propagating in sharp sub-granular bands as observed in experiments ([2] for example). Secondly, the current model predicts load drops as twins nucleate and grow, consistent with experiments. Both of these behaviors are not found in pseudo-slip models showing the importance of including a length scale, as done here.

Lastly, the cooperative behavior of inelastic deformations is captured in our phase-field model. Recently, Orozco-Caballero *et al.* [129] experimentally found, using

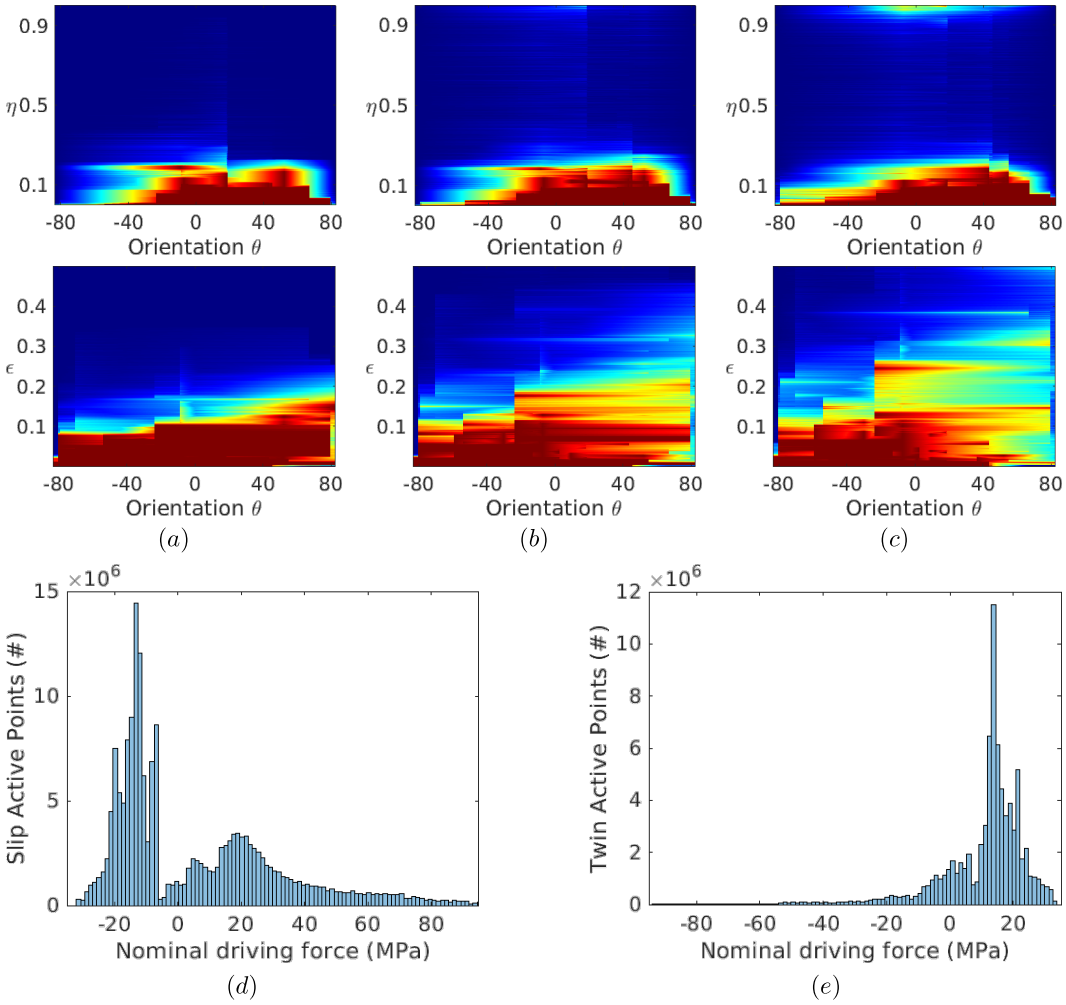

Figure 3.10: Statistical features of inelastic deformations for the Figure 3.7 case. (a–c) Heat map showing the distribution of twin volume fraction and plastic activity as a function of grain orientation at strains of $\gamma = 0.01, 0.044, 0.1$, respectively. Blue represents little activation at that orientation and inelastic value, while red represents a larger number of material points with that orientation and inelastic value. (d–e) Cumulative histogram of twin and slip activity v.s. nominal driving force.

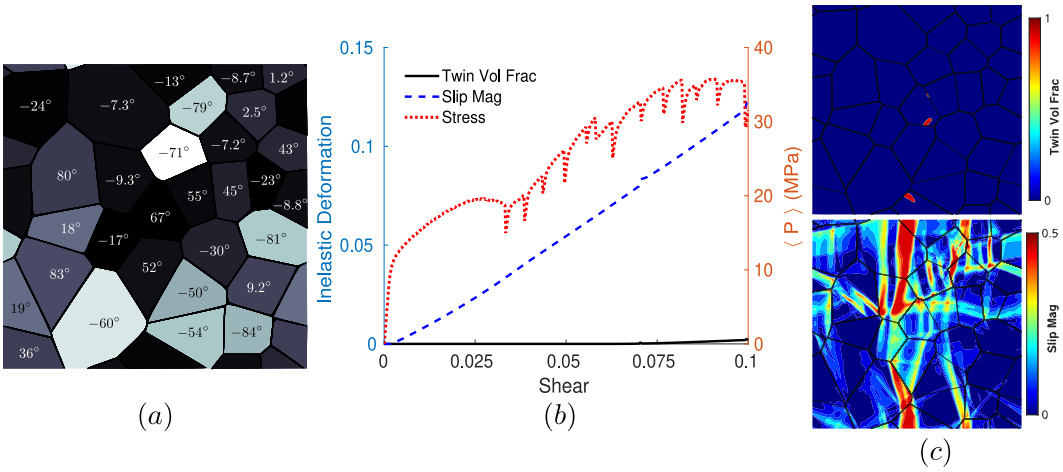

Figure 3.11: Asymmetry of response. Deformation of polycrystalline specimen subjected to reversed simple shear loading compared to Figure 3.7. (a) The polycrystalline specimen. The grayscale shows Schmidt factors for twinning and slip. Darker grains are favorably oriented for slip and lighter grains for twinning, while the numbers indicate the grain orientation. (b) Stress-strain behavior and evolution of average slip magnitude and twin volume fraction. (c) Snapshot of twin volume fraction (η) and slip magnitude (γ^{p}) at the final strain of $\gamma = -0.1$.

high-resolution digital image correlation and EBSD imaging of polycrystal magnesium alloys, that the activation of twinning and unfavorable slip systems help accommodate strain incompatibility at grain boundaries between drastically differing grains. Our observations of specimen-spanning deformation bands dominating the morphology and slip-twin bridging are in agreement with the experimentally observed behavior. These qualitative agreements motivate our current full three-dimensional implementation of this model and a detailed comparison with experiments.

3.5.2 Asymmetry of response

Starting with the same specimen as in Figure 3.7, we apply a shear in the opposite direction. The resulting twin and slip morphology, stress-strain curve, and average inelastic values are in Figure 3.11. Compared to the forward loading direction, we see much less twin activity and differing locations of twinning. Similarly, the slip activity changes drastically, with different grains exhibiting large plastic deformation. Finally, the changes in local inelastic deformations result in a macroscopic stress-strain curve with more stress hardening and stress drops. All of this is the analog in shear of the well-known tension-compression anisotropy in hcp materials.

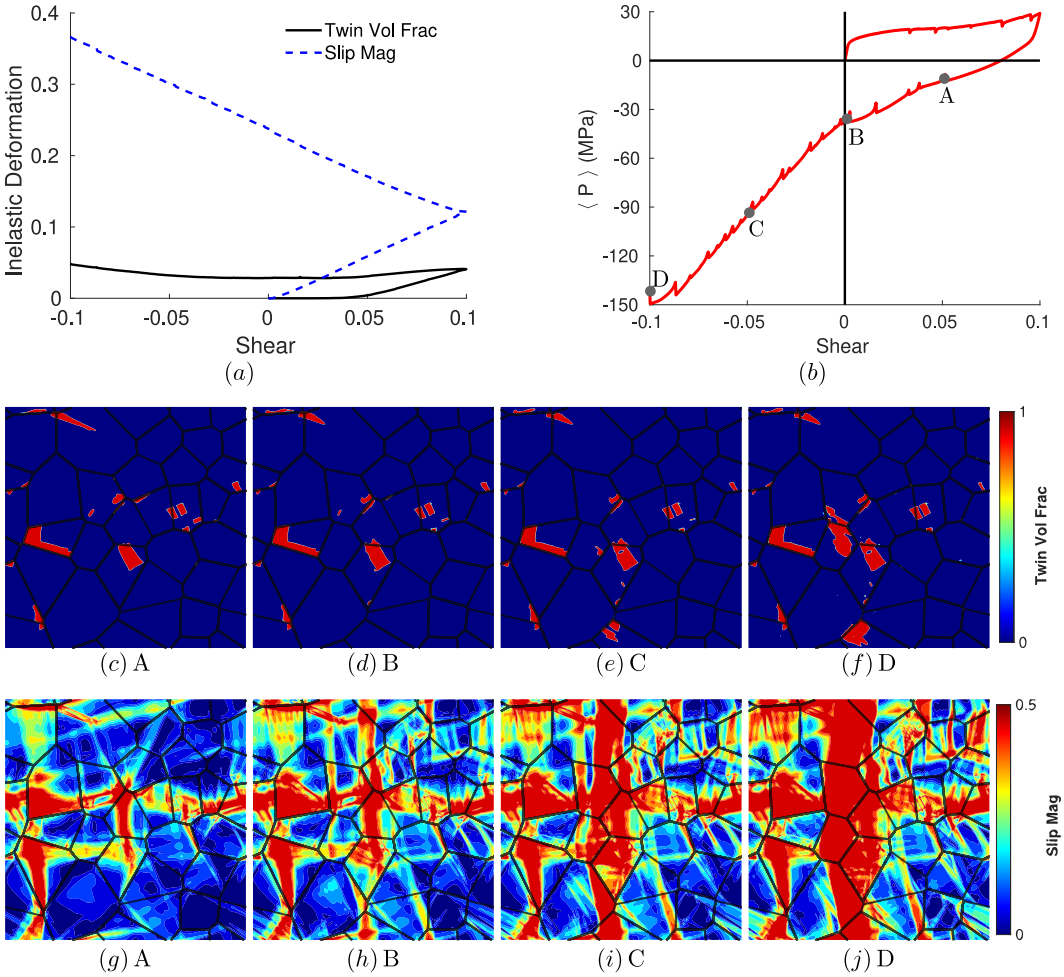

Figure 3.12: Proportional forward-reverse deformation. (a) Average twin volume fraction and slip magnitude versus shear strain. (b) Average stress-strain plot with markers indicating points at which microstructure plots are obtained. (c–f) Twin volume fractions at points during the reverse loading. (g–j) Slip magnitudes at points during the reverse loading.

3.5.3 Proportional loading-unloading-reverse loading

Once again, starting with the same specimen as in Figure 3.7, we apply a shear in the forward direction and then reverse the direction of shear till we have sheared it in the opposite direction. The results are shown in Figure 3.12. The forward shearing is as before. As the shear direction is reversed, we see significant residual strains. Further, there is a small amount of detwinning, though it is not complete, while the slip intensity continues increasing. Note that the detwinning would be more significant if we did not have slip. Thus, slip-induced deformation pins twins in place. As the applied shear goes through zero and eventually increases in the reverse direction, the twin volume fraction morphology remains relatively constant

till a large reverse shear, while the slip continues growing. We also see significant hardening. In particular, comparing Figures 3.11 and 3.12 at an applied shear of -0.1, we see that the stress is significantly higher and twin and slip morphology are drastically different as a result of the prior deformation. Thus, the interplay between slip and twinning provides a significant complexity in the role of prior deformation.

3.5.4 Non-proportional loading

Non-proportional loading is a crucial loading case for the failure analysis of materials and more closely matches applications. We consider two strain directions — shear $\mathbf{I} + \hat{\mathbf{u}}_0 \otimes \hat{\mathbf{w}}_0$ along 0° and shear $\mathbf{I} + \hat{\mathbf{u}}_{45} \otimes \hat{\mathbf{w}}_{45}$ along 45° where

$$\hat{\mathbf{u}}_0 = \{1, 0\},\ \hat{\mathbf{w}}_0 = \{0, 1\}; \quad \hat{\mathbf{u}}_{45} = 1/\sqrt{2}\{1, 1\},\ \hat{\mathbf{w}}_{45} = 1/\sqrt{2}\{1, -1\}. \tag{3.24}$$

We consider three strain paths — first shearing along 0° and then along 45°, first shearing along 45° and then along 0°, and a combined shear path — where the end macroscopic strain states are the same. The results are shown in Figure 3.13. We see that the end state of stress is different, as are the twin and slip morphologies. Interestingly, load paths 1 and 3 lead to a similar (though distinct) state of stresses, though the slip and twin morphologies are different. Path 2 leads to significantly higher hardening. This example again shows the complex history dependence of the state of stress and morphology.

3.5.5 Twin and slip activity

We explore the variation of twin and slip activity for differing nucleation threshold values by varying the parameters, τ_0^{p}, τ_0^{t}, and M, all of which impact the nucleation and propagation of twinning and slip. To isolate the effect of these material parameters, we fix the grain structure from Figure 3.7a. The resulting average stress, slip magnitude, and twin volume fraction, along with microstructure snapshots at the end of loading, are shown below in Figures 3.14, 3.15, and 3.16 for varying M, τ_0^{t}, and τ_0^{p}, respectively.

Surface energy As mentioned in Section 3.2.4, the double-well parameter, M, controls twin nucleation and is supported by earlier non-zero twin volume fractions for smaller M in Figure 3.14 (a). This earlier twin nucleation leads to larger final twin volume fractions and a smaller final slip magnitude for small M. The stress-strain curves exhibit an earlier twin yield and more stress softening for small M values. For larger values of M, the opposite is found, less (essentially negligible) twin volume fractions, more slip activity, and more stress hardening, as seen in

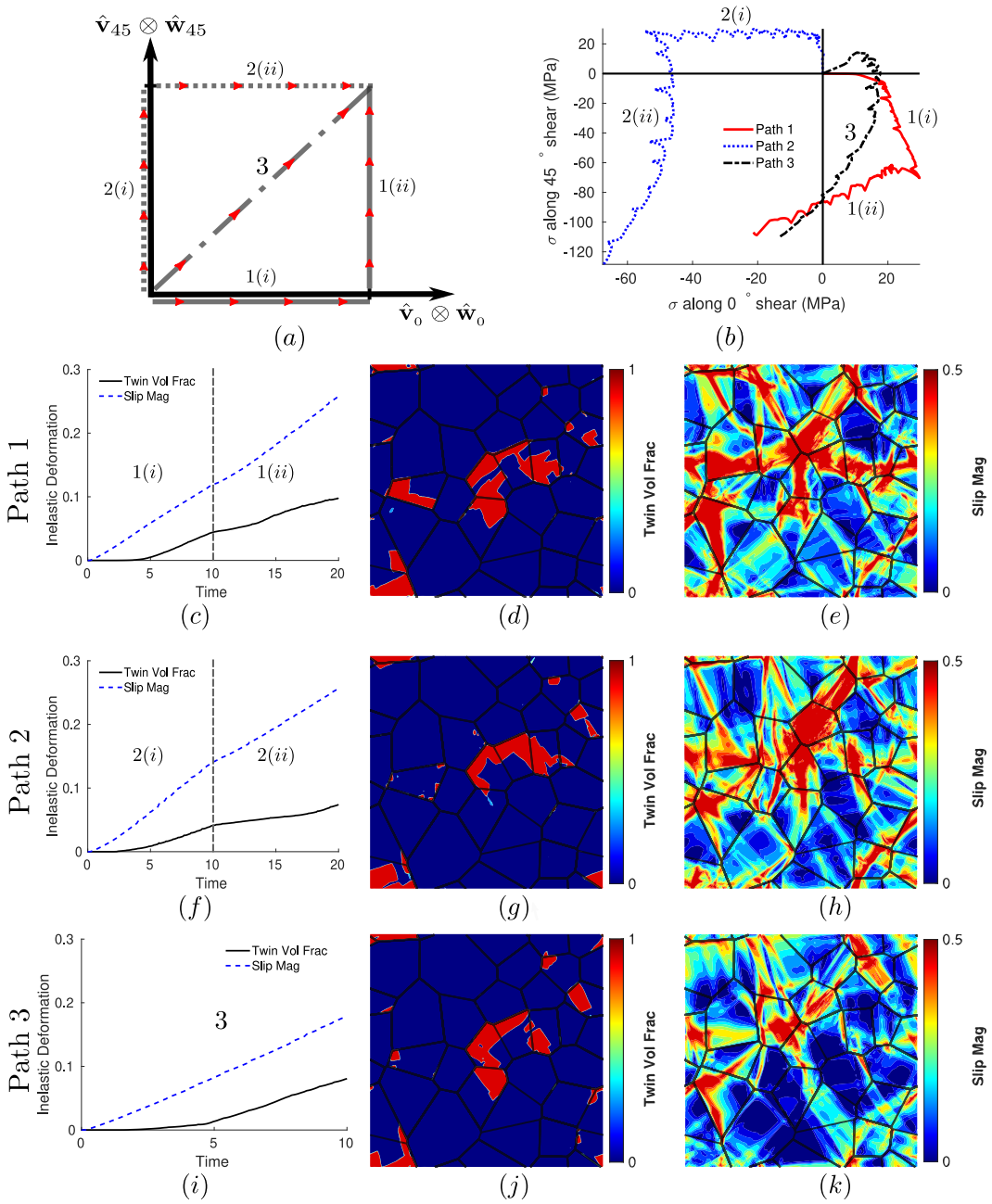

Figure 3.13: Non-proportional loading. Three macroscopic strain paths (a) are simulated with identical final strain. (b) Shear stress paths for each loading. Average twin volume fraction and slip magnitude and final twin and slip morphology for path 1 (c–e), path 2 (f–h), and path 3 (i–k).

Figure 3.14 (g). Finally, the twin morphology (and slip magnitudes) match these observations, with several twin bands present (and decreased slip) for the low M case and fewer twinned grains (and increased slip activity) as M increases.

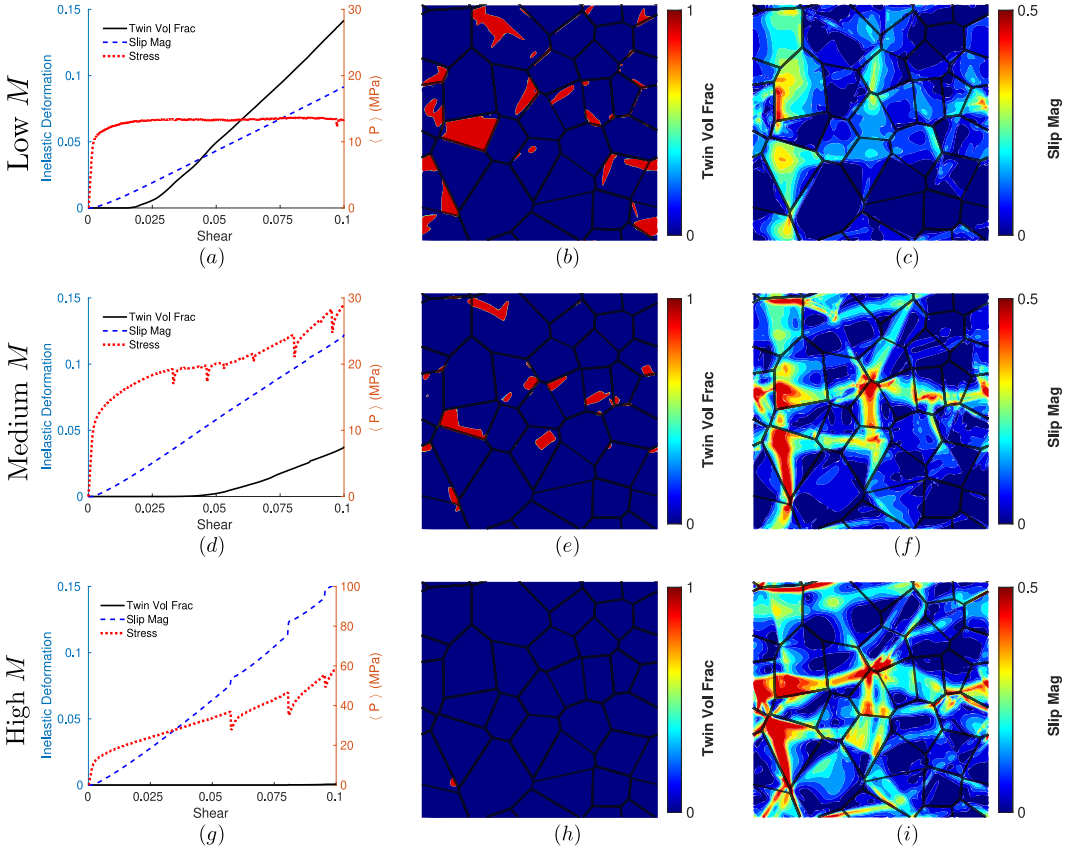

Figure 3.14: Role of surface energy. Average stress, twin volume fraction and slip magnitude, final twin, and slip microstructure for (a–c) $M = 8$ MPa (d–f) $M = 80$ MPa and (g–i) $M = 800$ MPa. All other parameters as before.

Twin rate hardening The rate hardening parameter, τ_0^t, affects both twin nucleation and propagation. Comparing Figure 3.15 (a), (d), and (g) as τ_0^t decreases, the twin nucleation change is relatively minor, compared to changing the surface energy parameter. However, there is a more noticeable increase in the final twin volume fraction. Consequently, with the decreasing τ_0^t, the slip magnitude decreases due to the higher presence of twinning. The stress-strain curve exhibits a slightly earlier twin yield and more stress softening for lower values of τ_0^t. For larger values of τ_0^t, we find the opposite, more slip activity, smaller average twin volume fraction, and more stress hardening. Lastly, looking at the twin morphology (and slip magnitude), we again see matching results — the presence of more and larger twin bands (and

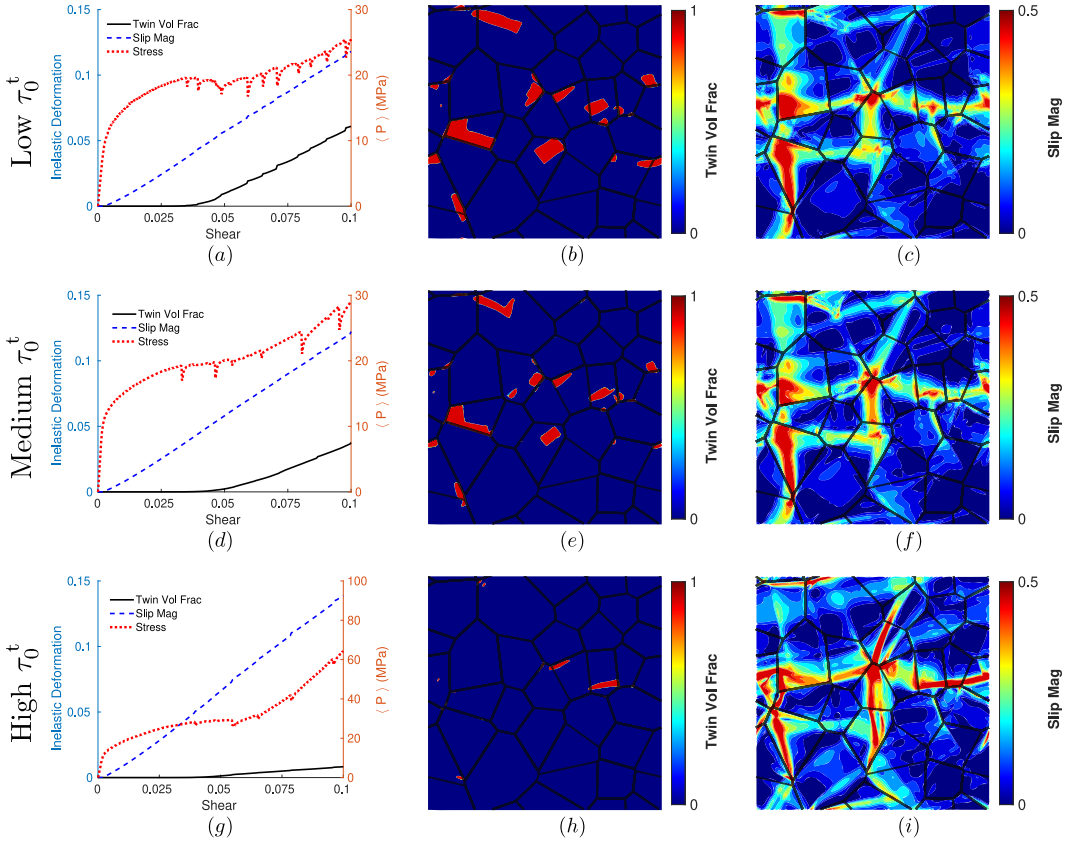

Figure 3.15: Effect of twin rate hardening. Average stress, twin volume fraction and slip magnitude, final twin, and slip microstructure for (a–c) $\tau_0^t = 0.1$ MPa, (d–f) $\tau_0^t = 1$ MPa and (g–i) $\tau_0^t = 10$ MPa.

decreased slip magnitudes) for lower τ_0^t.

Slip rate hardening The rate hardening parameter, τ_0^p, affects both slip nucleation and propagation. Looking at Figure 3.16 (a), (d), and (g), we observe for smaller τ_0^p values, the average slip magnitude shows earlier nucleation and higher final slip activity, while there is a decrease in the average twin volume fraction. The stress-strain curve exhibits an earlier slip yield point and larger hardening due to the suppression of twins for smaller τ_0^p. For larger values of τ_0^p, we find the opposite, less slip activity, more twinning activity, and a delayed slip yield point. Finally, looking at the final morphology, we again observe a clear coupling between slip and twinning. Despite the slip parameter varied, there is a noticeable effect on the twin volume fraction, which accommodates the applied strain when slip is less able to for the high τ_0^p case.

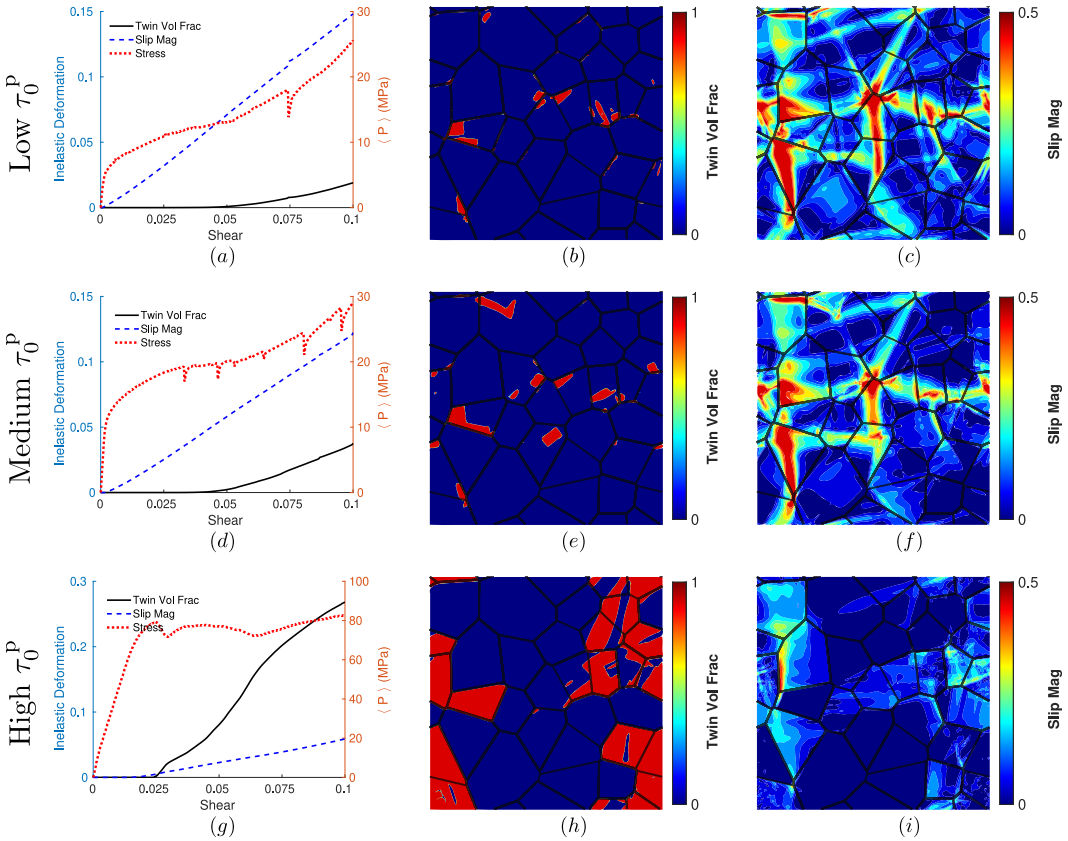

Figure 3.16: Effect of slip rate hardening. Average stress, twin volume fraction and slip magnitude, final twin, and slip microstructure for (a–c) τ_0^p = 0.4 MPa, (d–f) τ_0^p = 4 MPa and (g–i) τ_0^p = 40 MPa.

3.5.6 Texture

We consider the same grain structure, material parameters, and loading as Section 3.5.1 but with different grain orientations.

Twin centered texture The grain angles are now sampled from a Gaussian centered around the twin direction — seen in Figure 3.17(a). The resulting final twin and slip morphology, stress-strain curves, and average inelastic deformations are shown in Figure 3.17(c–e). Compared to the original case, we see more twin activity and its presence in different grains due to the change in favorable grains. Similarly, the slip activity changes drastically, with differing grains exhibiting large plastic deformation. Finally, the increased presence of twin bands leads to more stress drops in the stress-strain curve.

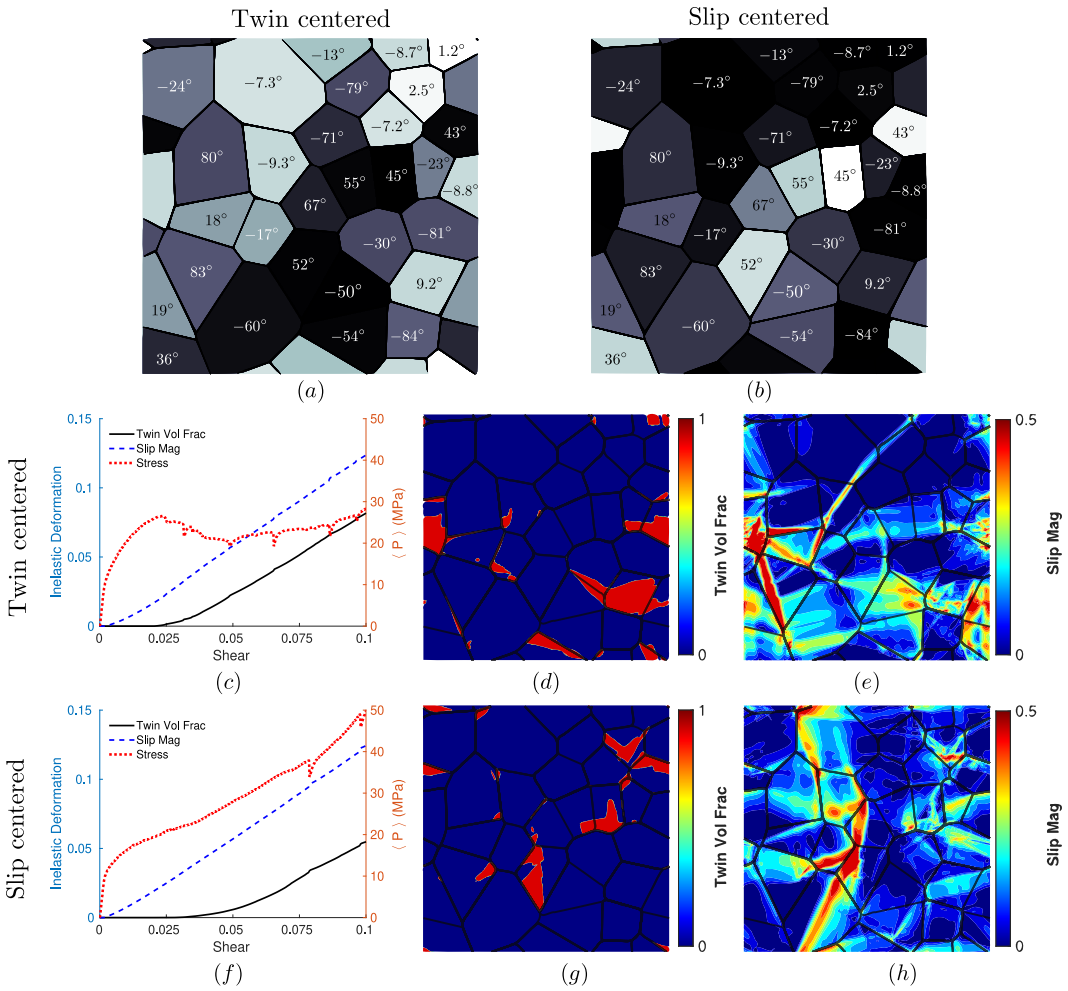

Figure 3.17: Role of texture. Deformation of the different polycrystalline specimens subjected to simple shear. Polycrystalline specimen for twin centered (a) and slip centered (b) grain angles. The grayscale shows Schmidt factors for twinning and slip. Darker grains are favorably oriented for slip and lighter grains for twinning, while the numbers indicate the grain orientation. Stress-strain behavior and average inelastic deformations for twin centered (c) and slip centered (f) grains. Final twin volume fraction (η) and slip magnitude (γ^{p}) at a final strain of $\gamma = 0.1$ for twin centered (d–e) and slip centered (g–h) grains.

Slip centered texture The grain angles are now sampled from a Gaussian about the slip direction — seen in Figure 3.17(b). The resulting final twin and slip morphology, stress-strain curve, and average inelastic deformations are shown in Figure 3.17(e–h). Compared to the original case, we see less twin activity and its presence in different grains due to the change in favorable grains. Similarly, the slip activity changes drastically, with more grains exhibiting large plastic deformation. Finally, the decrease in twin bands leads to more hardening in the stress-strain curve.

3.5.7 Comparison with the results of a pseudo-slip model

We now compare the results above with those obtained from a pseudo-slip model following [42]. The model details are provided in Chapter 2 with a computational implementation similar to that used for the phase field model. Briefly, pseudo-slip borrows ideas from crystal plasticity to obtain average twin volume fractions rather than resolving the specific morphology.

Figure 3.18 compares the results of the two models under identical parameters, initial microstructure, and loading. Figure 3.18(b) shows the pseudo-slip stress-strain curve has only one yield point due to slip and twinning now having identical nucleation criteria. Comparing the evolution of the average volume fractions and slip activity (Figure 3.18(a) and (b)), we see that twinning nucleates early and dominates the deformation in the pseudo-slip model compared to our model. Indeed, comparing Figure 3.18(c–f) to Figure 3.18(g–j), we see early and extensive twinning in the pseudo-slip model with drastically different morphology. Our model predicts well-defined twin bands, while the pseudo-slip model predicts diffuse twinning extending across the grains. All of this is expected since the pseudo-slip model does not seek to define thin twins, does not account for twin boundary energy that sets a length scale, and does not have any nucleation barrier. Finally, Figure 3.18(k–m) and Figure 3.18(n–q) show that slip is greatly suppressed in the pseudo-slip model. This slip reduction is due to twinning accommodating a more significant portion of the deformation and diffuse twins contributing smaller incompatibilities.

3.6 Discussion

In this work, we have presented a model that describes deformation twins and plastic dislocation slip at the scale of multiple grains, their morphology, their interaction, and their implications on macroscopic behavior. We start with the detailed kinematics of twinning following Mahajan and Christian [49] and implement it using a phase-field framework to incorporate detailed morphology, nucleation barrier, surface energy, propagation drag, and rate hardening. We treat dislocation plasticity in the framework of crystal plasticity. We implement the model on graphical processing units following [160]. This work aims to understand various aspects of the interaction between deformation twinning and dislocation slip in polycrystal domains. Therefore we use detailed simulations in two dimensions to study the nucleation and growth of twins, the evolution of slip, the cooperative mechanism of bridging across grains, geometrically necessary dislocations, and the role of fluctuations.

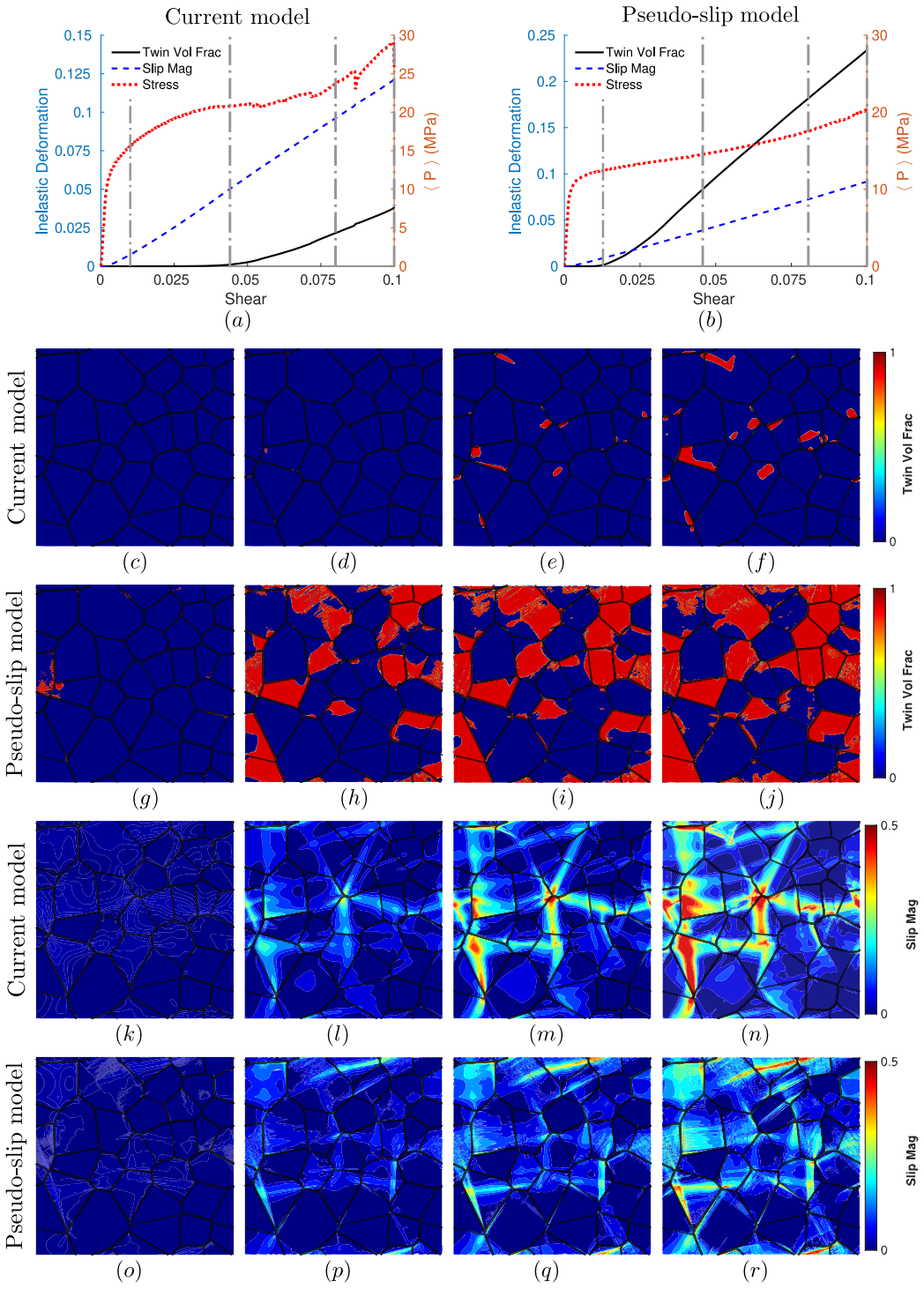

Figure 3.18: Comparison with pseudo-slip model. Stress strain curve and average slip magnitude and twin volume fraction for phase-field (a) and pseudo slip (b). The gray dashed lines correspond to points where the microstructure is plotted. Phase-field's twin volume fraction (c–f) and pseudo slip's twin volume fraction (g–j) at strains of $\gamma = 0.01,\ 0.044,\ 0.07,\ 0.1$. Phase-field's slip magnitude (k–n) and pseudo slip's twin volume fraction (o–r) at strains of $\gamma = 0.01,\ 0.044,\ 0.07,\ 0.1$.

We observe that macroscopic quantities like propensity for twinning and slip, and nominal driving force (Schmid factor) are suggestive but not predictive of the presence of twinning and slip in a grain. Grains well-oriented for slip were more likely to slip, and those oriented for twinning were more likely to twin (see Figure 3.7). However, grains with a similar orientation may behave differently, and one can observe twinning and slip even when the nominal driving force or Schmidt factor is negative (Figure 3.10). This is in agreement with observations in magnesium and its alloys [20, 67, 88], and zirconium and its alloys [2, 27, 40, 112].

There are two notable reasons for this non-Schmid behavior. The first is the anisotropy of the elastic modulus that leads to a heterogeneous state of stress. In particular, we have significant amounts of stress concentrations at triple junctions, which in turn leads to heterogeneous nucleation (see Figure 3.8). The second is an incompatibility between neighboring grains. This is evident both during nucleation, where it tends to occur in multiple grains, and during growth, where deformation mechanisms can bridge poorly oriented grains to connect well-oriented grains (see the circled regions in Figure 3.7). This is highlighted by examining the geometrically necessary dislocations (Figure 3.9). These are again in qualitative agreement with experimental observations. In situ electron backscatter diffraction (EBSD) observations of Guo *et al.* [70] in magnesium emphasize the simultaneous nucleation of twins in multiple grains and the formation of twin chains. Combined high-resolution digital image correlation (HRDIC) and EBSD observations of Orozco-Caballero *et al.* [129] in the magnesium alloy AZ31 show the heterogeneous nature of deformation at the sub-granular and multi-granular scales, and how hard slip can be activated to bridge deformation across grains. Similarly, EBSD observations of AZ31 of Jonas *et al.* [88] confirmed that twins formed in low Schmidt factor grains to bridge those formed in high Schmidt factor grains.

We also used simulations to study the asymmetric deformation response due to twinning and the history dependence in both proportional and non-proportional loading. Importantly, note that our simple model includes self-hardening slip, but neither self-hardening in twinning nor cross-hardening between twin-slip are considered. Still, we see that the deformation history significantly affects the response in proportional, shear direction change, and non-proportional loading. In other words, these examples show that the systems can interact through the microstructure and residual strain even in the absence of cross-hardening. All of these provide insights into the deformation behavior of low symmetry crystals where both deformation twinning

and dislocation slip are significant.

We then compare our model with previous work that treated twinning as a "pseudo-slip" in the crystal plasticity framework. A key observation is that the pseudo-slip removes the nucleation barrier from surface energy leading to the earlier and easier creation of twins. This is consistent with the detailed comparative study between (EBSD) observations and pseudo-slip based crystal plasticity simulations by Abdolvand and Daymond [2]; this study showed that the pseudo-slip model significantly over-predicted the extent of twinning. Additionally, Figure 3.18 shows that the current model predicts twins nucleating and propagating in sharp sub-granular bands as observed in experiments (for example, [14]). In contrast, the pseudo-slip model predicts pervasive twinning on the granular scale. Lastly, the current model predicts load drops as twins nucleate and grow, consistent with experiments, while the pseudo-slip model predicts a smooth yield. The pseudo-slip approach ignores twin-boundary energy and thus lacks a length scale leading to an under-prediction of the nucleation barrier.

Chapter 4

DEFORMATION TWINNING AND DISLOCATION SLIP INTERACTIONS IN POLYCRYSTALLINE MAGNESIUM

4.1 Motivation

Recent decades have seen increased interest in alloys with low symmetry, specifically hexagonal close-packed crystal structures, for structural applications due to their high strength-to-weight ratio. For example, magnesium alloys have amongst the highest strength-to-weight ratio (with a density of 1.8 g/cm^3 and yield strength exceeding 100 MPa) of known metals and have been explored for automotive, biomedical, and other engineering applications. However, these alloys often have limited ductility and suffer sudden, almost brittle-like failure. We refer the reader to recent reviews [46, 89, 102, 104] on magnesium for a comprehensive background.

The high strength-to-weight ratio and limited ductility originate from the low symmetry crystals' anisotropic elasticity and the resulting complexity in deformation modes (e.g., [94]). For example, magnesium, which is hexagonal close-packed, has an easy basal slip system and relatively easy tension twins but hard pyramidal and prismatic slip systems. Unfortunately, the basal slip and tension twin systems are deficient, i.e., they cannot accommodate an arbitrary deviatoric strain. Therefore, a polycrystal of these materials needs to engage the hard slip systems resulting in high strength. However, the mismatch between the strength of these systems leads to strain localization and other related phenomena that cause easy failure. This is in contrast with face-centered cubic crystals, where the slip systems are complete and of identical yield strength. Additionally, the easy presence of twinning adds several complexities. Unlike slip, twinning leads to a rotation of the lattice, experimentally appears as sharp bands, and has an asymmetric nucleation. Finally, the coexistence of twinning and slip in magnesium leads to rich microstructural phenomena and complex macroscopic responses.

Various approaches to understanding twinning within magnesium have been explored over the years, from atomistic to continuum-mechanics descriptions. Our focus here is on the latter in the context of mesoscale modeling, with the incorporation of as much microscale physics as necessary. Early models on describing twinning borrowed concepts from crystal plasticity and included twins as an addi-

tional slip system (often referred to as pseudo slip systems) [91, 132]. However, these first models did not account for the lattice reorientation. Thus, subsequent pseudo-slip models accounted for twin's lattice reorientation [7, 42, 43, 136]. In recent years, the importance of twin morphology has also been shown experimentally. For example, Abdolvand and Daymond [2] showed significant differences in twin evolution in Zircaloy-2 between electron back-scatter diffraction (EBSD) observations and pseudo-slip based crystal plasticity simulations. Thus, a focus on the role of morphology, especially through the cooperative actions of grains, has been emphasized by several researchers recently [22, 129]. Jin *et al.* [87] developed a model for inserting fully twinned regions (via strain discontinuities) when appropriate stochastic conditions were met. However, this model does not fully capture the nucleation and growth of twins and thus misses the interaction with dislocations. Several researchers addressed these shortcomings, for example, [11, 12, 47, 48], by explicitly inserting discrete twin lamella based on total accumulated twin activity from pseudo-slip models (modified with dislocation disassociation motivated criteria for nucleation, propagation, and growth), while locally modifying the deformation history to account for the twinning shear. However, all of these approaches introduce twins discreetly, removing the benefits of a continuous variable describing the twin morphology and surface energy specifics on twin nucleation.

Phase-field models have long been used to study morphology in the context of phase transitions (e.g., [14]) due to their natural evolution laws through a smooth variable to describe twinning. However, past studies have primarily been in the context of small (geometrically linear) strains, without complex twin-slip interactions (e.g., [50]), or limited to describing single twin systems [115]. Recently, Liu *et al.* [115] proposed a phase-field model that combines deformation twinning and plastic slip, and used it to study single crystals in three dimensions and polycrystals in two dimensions. However, their model still used an incremental update for the twinning deformation, borrowing from the pseudo-slip models. Hence, we plan to extend our phase-field model for twinning introduced in Chapter 3. We previously showed the model's capabilities to capture twinning's length scale and the resultant complex twin-slip interactions in two-dimensional single-crystal and polycrystal simulations. We now propose to follow crystal plasticity models to account for multiple of magnesium's slip systems, include multiple phase field variables to track the evolution of several twin systems, and finally adopt the massively parallel implementation by [160] to conduct high-resolution studies. The focus of this work is to showcase the model's capabilities and implementation to conduct detailed simulations capturing complex

twin-slip interactions in real polycrystal magnesium samples and conclude with proposed future works.

4.2 Extension of model

We now extend the model from Section 3.2 to include both multiple slip and twin systems. Suppose the material exhibits N_s slip systems and N_t twin systems, each with slip/shear and normal directions given by $(\hat{\mathbf{b}}^{\mathrm{p}}_{\alpha}, \hat{\mathbf{n}}^{\mathrm{p}}_{\alpha})$ and $(\hat{\mathbf{b}}^{\mathrm{t}}_{\beta}, \hat{\mathbf{n}}^{\mathrm{t}}_{\beta})$, respectively. We can track the evolution of the slip systems through a vector of plastic slip activity, $\boldsymbol{\gamma}^{\mathrm{p}} \in \mathbb{R}^{N_s}$ with components acting on each slip system. We evolve multiple twin systems through multiple phase variables, $\boldsymbol{\eta} = \{\eta_1, \cdots \eta_{N_t}\}$, with their specific combination describing the lattice state of any material point.

4.2.1 Kinematics

We, again, assume the body is undergoing a deformation with a gradient ($\mathbf{F} = \nabla \mathbf{y}$) decomposed into elastic, plastic, and twinning parts as,

$$\mathbf{F} = \mathbf{F}^{\mathrm{e}}\mathbf{F}^{\mathrm{p}}\mathbf{F}^{\mathrm{t}}. \tag{4.1}$$

The twinning deformation will be decomposed into an additive form, i.e., a sum of shears from each twin system,

$$\mathbf{F}^{\mathrm{t}} = \mathbf{I} + \sum_{\beta=1}^{N_t} \eta_\beta \gamma^{\mathrm{t}}_{0\beta}\, \hat{\mathbf{b}}^{\mathrm{t}}_{\beta} \otimes \hat{\mathbf{n}}^{\mathrm{t}}_{\beta}, \tag{4.2}$$

where $\gamma^{\mathrm{t}}_{0\beta}$ is the twin shear for twin system β. The plastic deformation in the parent (untwinned) lattice will follow classical crystal plasticity models [99, 140] with a rate update contributed from each slip system,

$$\dot{\mathbf{F}}^{\mathrm{p}} = \left[\sum_{\alpha=1}^{N_s} \dot{\gamma}^{\mathrm{p}}_{\alpha} \hat{\mathbf{b}}^{\mathrm{p}}_{\alpha} \otimes \hat{\mathbf{n}}^{\mathrm{p}}_{\alpha}\right] \mathbf{F}^{\mathrm{p}} \quad \text{in parent lattice.} \tag{4.3}$$

To arrive at a unified description across twinned and untwinned regions, we introduce slip and normal directions in each twinned region as, $\hat{\mathbf{b}}'^{\mathrm{p}}_{\alpha\beta}$ and $\hat{\mathbf{n}}'^{\mathrm{p}}_{\alpha\beta}$, respectively, which represents slip system α in the β twinned lattice. The slip systems in the twinned lattice are defined using the parent slip systems as,

$$\hat{\mathbf{b}}'^{\mathrm{p}}_{\alpha\beta} = \mathbf{R}_\beta \hat{\mathbf{b}}^{\mathrm{p}}_{\alpha}, \quad \hat{\mathbf{n}}'^{\mathrm{p}}_{\alpha\beta} = \mathbf{R}_\beta \hat{\mathbf{n}}^{\mathrm{p}}_{\alpha} \quad \text{with} \quad \mathbf{R}_\beta = 2\hat{\mathbf{n}}^{\mathrm{t}}_{\beta} \otimes \hat{\mathbf{n}}^{\mathrm{t}}_{\beta} - \mathbf{I} \quad \text{(no sum)}. \tag{4.4}$$

Thus, the plastic deformation is modified from the conventional crystal plasticity to account for dislocation activity on both the parent and twinned lattices [136, 159],

$$\dot{\mathbf{F}}^{\mathrm{p}} = \sum_{\alpha=1}^{N_s} \dot{\gamma}_{\alpha}^{\mathrm{p}} \left[(1 - \sum_{\beta=1}^{N_t} \eta_{\beta}) \hat{\mathbf{b}}_{\alpha}^{\mathrm{p}} \otimes \hat{\mathbf{n}}_{\alpha}^{\mathrm{p}} + \sum_{\beta=1}^{N_t} \eta_{\beta} \hat{\mathbf{b}}_{\alpha\beta}^{\prime\mathrm{p}} \otimes \hat{\mathbf{n}}_{\alpha\beta}^{\prime\mathrm{p}} \right] \mathbf{F}^{\mathrm{p}}. \tag{4.5}$$

Note that this form differs from the two-dimensional case in Section 3.2 — where we used linear combinations of slip angles — and instead, we work directly with the parent and twin lattice slip directions. The main motivation for this change is to more easily evolve the slip directions without having to track three-dimensional rotations, whose derivatives would increase the computation complexity.

Finally, we include the accumulated slip for each slip system, $\epsilon_{\alpha}^{\mathrm{p}}$, in order to dictate strain hardening. The accumulated slip of each system evolves identical to Section 3.2, as $\dot{\epsilon}_{\alpha}^{\mathrm{p}} = |\dot{\gamma}_{\alpha}^{\mathrm{p}}|$.

4.2.2 Free energy

We again postulate a free energy density with a similar decomposition and form as the single twin and slip system case,

$$W(\mathbf{F}^{\mathrm{e}}, \boldsymbol{\eta}, \nabla\boldsymbol{\eta}, \epsilon^{\mathrm{p}}) = W_{\mathrm{e}}(\mathbf{F}^{\mathrm{e}}, \boldsymbol{\eta}) + W_{\mathrm{t}}(\boldsymbol{\eta}) + \frac{\alpha}{2} \|\nabla\boldsymbol{\eta}\|^2 + W_{\mathrm{p}}(\epsilon^{\mathrm{p}}). \tag{4.6}$$

W_{e} is the elastic energy,

$$W_e(\mathbf{F}^{\mathrm{e}}, \boldsymbol{\eta}) = \frac{1}{2} \mathbf{E}^e : \mathbb{C}(\boldsymbol{\eta}) : \mathbf{E}^e, \tag{4.7}$$

with a non-linear strain measure and a weighted phase field average of the anisotropic modulus,

$$\mathbb{C}(\boldsymbol{\eta}) = \big(1 - \sum_{\beta=1}^{N_t} \eta_{\beta}\big) \mathbb{C}(\boldsymbol{\eta} = \mathbf{0}) + \sum_{\beta=1}^{N_t} \eta_{\beta} \mathbb{C}(\eta_{\beta} = 1), \tag{4.8}$$

to account for reorientation from each twin lattice. W_{t} is now a multi-well energy for twinning,

$$W_{\mathrm{t}}(\boldsymbol{\eta}) = \frac{M_s}{2} \sum_{\beta=1}^{N_t} \eta_{\beta}^2 (1 - \eta_{\beta})^2 + W_{\mathrm{t,\,lat}}(\boldsymbol{\eta}), \tag{4.9}$$

with M_s being the multi-well parameter. The first term in equation 4.9 enforces $\eta_\beta \in [0, 1]$, while the second term is a twin-latent hardening term to penalize the activation of multiple twin systems at any location at the same time. $\frac{\alpha}{2} \|\nabla \boldsymbol{\eta}\|$ is the isotropic twin surface energy, which now includes the gradient of the entire vector of phase field variables, with surface energy parameter α. Together M_s and α will dictate the twin surface energy, interface thickness, and nucleation threshold as was discussed in Section 3.2.5. W_p is the plastic work hardening,

$$W_p(\boldsymbol{\epsilon}^\mathrm{p}) = W_{\mathrm{p,\,self}}(\boldsymbol{\epsilon}^\mathrm{p}) + W_{\mathrm{p,\,lat}}(\boldsymbol{\epsilon}^\mathrm{p}). \tag{4.10}$$

The first term describes plastic self-hardening, which will be a sum of the exponential Voce hardening utilized prior [7, 42, 68],

$$W_{\mathrm{p,\,self}}(\boldsymbol{\epsilon}^\mathrm{p}) = \sum_{\alpha=1}^{N_s} \sigma_\alpha^\infty \left[\epsilon_\alpha^\mathrm{p} + \frac{\sigma_\alpha^\infty}{h_\alpha} \exp\left(- \frac{h_\alpha \epsilon_\alpha}{\sigma_\alpha^\infty} \right) \right], \tag{4.11}$$

and the second term is a plastic latent hardening term accounting for the penalization of multiple slip systems present at one material point,

$$W_{\mathrm{p,\,lat}}(\boldsymbol{\epsilon}^\mathrm{p}) = \frac{1}{2} \boldsymbol{\epsilon}^\mathrm{p} \cdot \mathcal{K} \boldsymbol{\epsilon}^\mathrm{p}, \tag{4.12}$$

where $\mathcal{K}$ is a symmetric matrix containing the hardening moduli on the off-diagonal entries and zeros along the diagonal.

4.2.3 Equilibrium and evolution

We, again, obtain the equilibrium and internal variable evolution through the use of the principle of minimum dissipation potential, which requires the use of the dual dissipation potential, $\Psi^*(\dot{\boldsymbol{\eta}}, \dot{\boldsymbol{\gamma}}^\mathrm{p})$. We assume the contributions to the dual potential are additive for each system [42],

$$\Psi^*(\dot{\boldsymbol{\eta}}, \dot{\boldsymbol{\gamma}}^\mathrm{p}) = \sum_{\alpha=1}^{N_s} \Psi_\mathrm{p}^*(\dot{\gamma}_\alpha^\mathrm{p}) + \sum_{\beta=1}^{N_t} \Psi_\mathrm{t}^*(\dot{\eta}_\beta), \tag{4.13}$$

with the individual twin and slip contributions following the forms,

$$\Psi^*(\,\cdot\,) = \left[\tau_0 |\,\cdot\,| + \frac{\tau_0 \dot{\gamma}_0}{m+1} \left(\frac{|\,\cdot\,|}{\dot{\gamma}_0} \right)^{m+1} \right]. \tag{4.14}$$

The resulting mechanical equilibrium is,

$$\nabla \cdot \mathbf{P} = \mathbf{0}, \quad \text{with} \quad \mathbf{P} = \frac{\partial W^{\mathrm{e}}}{\partial \mathbf{F}} = \frac{\partial W^{\mathrm{e}}}{\partial \mathbf{F}^{\mathrm{e}}} (\mathbf{F}^{\mathrm{p}} \mathbf{F}^{\mathrm{t}})^{-\intercal}, \tag{4.15}$$

while the evolution of the internal variables $\boldsymbol{\gamma}^{\mathrm{p}}$ and $\boldsymbol{\eta}$ is,

$$0 \in -\tau_{\alpha}^{\mathrm{p}} + \frac{\partial W_{\mathrm{p}}}{\partial \epsilon_{\alpha}} + \partial_{\dot{\epsilon}_{\alpha}} \Psi_{\mathrm{p}}^{*} \quad \forall \alpha \in [1, N_s], \tag{4.16}$$

$$0 \in -\tau_{\beta}^{\mathrm{t}} + \frac{\partial W_{\mathrm{e}}}{\partial \eta_{\beta}} + \frac{\partial W_{\mathrm{t}}}{\partial \eta_{\beta}} + \alpha \nabla^2 \eta_{\beta} + \partial_{\dot{\eta}_{\beta}} \Psi_{\mathrm{t}}^{*} \quad \forall \beta \in [1, N_t], \tag{4.17}$$

where $\tau_{\alpha}^{\mathrm{p}}$ and $\tau_{\beta}^{\mathrm{t}}$ are the slip and twin resolved shear stress, respectively, for the α slip system and β twin system,

$$\tau_{\alpha}^{\mathrm{p}} = \boldsymbol{\sigma}^{\mathrm{p}} : \left[\left(1 - \sum_{\beta=1}^{N_t} \eta_{\beta} \right) \hat{\mathbf{b}}_{\alpha}^{\mathrm{p}} \otimes \hat{\mathbf{n}}_{\alpha}^{\mathrm{p}} + \sum_{\beta=1}^{N_t} \eta_{\beta} \hat{\mathbf{b}}_{\alpha\beta}^{\prime\,\mathrm{p}} \otimes \hat{\mathbf{n}}_{\alpha\beta}^{\prime\,\mathrm{p}} \right], \ \boldsymbol{\sigma}^{\mathrm{p}} = \mathbf{F}^{\mathrm{e}\,T} \mathbf{P} (\mathbf{F}^{\mathrm{p}} \mathbf{F}^{\mathrm{t}})^{T} \tag{4.18}$$

$$\tau_{\beta}^{\mathrm{t}} = \boldsymbol{\sigma}^{\mathrm{t}} : \hat{\mathbf{b}}_{\beta}^{\mathrm{t}} \otimes \hat{\mathbf{m}}_{\beta}^{\mathrm{t}}, \ \boldsymbol{\sigma}^{\mathrm{t}} = \gamma_{0\beta}^{\mathrm{t}} (\mathbf{F}^{\mathrm{e}} \mathbf{F}^{\mathrm{p}})^{T} \mathbf{P}. \tag{4.19}$$

Note that the slip-resolved shear stress form differs from Section 3.2 due to the change in the parent and twin lattice dislocation formulation in equation 4.5.

4.2.4 Twinning latent hardening

Here we mention the significance of the twin latent hardening energy, $W_{\mathrm{t,\,lat}}(\boldsymbol{\eta})$, as well as comment on the forms explored. $W_{\mathrm{t,\,lat}}(\boldsymbol{\eta})$ represents a twin latent hardening term which would penalize the coalescence of different twin variants at the same material point and time. Although experiments show evidence of higher-order twin patterns, i.e., the nucleation of a second (or more) twin in an already twinned region (see, e.g., Hong *et al.* [77] or other researchers [24, 59, 108]), details on the exact order of evolution and forming of the double twins is not clear. Hence, the only criteria we choose for $W_{\mathrm{t,\,lat}}(\boldsymbol{\eta})$ is to increasingly penalize the formation of a second twin system during the formation of a first twin band.

The common phase-field approach for the latent hardening term is,

$$W_{\mathrm{t,\,lat}}^{(1)}(\boldsymbol{\eta}) = \frac{M_l}{2} \left(\sum_{\beta=1}^{N_t} \eta_{\beta} \right)^2 \left(1 - \sum_{\beta=1}^{N_t} \eta_{\beta} \right)^2, \tag{4.20}$$

which would have a zero energy state when a material point is in the parent or a twin lattice. However, an additional, undesirable, zero energy state is $\sum_{\beta=1}^{N_t} \eta_{\beta} = 1$,

such as $\eta_\beta = 1/N_t$, which would allow regions where a material point is at the interface of multiple twin regions, rather than entirely in one. Practically from numerical experiments, this led to regions where twin band formation was delayed, or completely stopped, in favor of multiple twin interfaces.

As an alternative, we explored the form of $W_{\text{t, lat}}(\boldsymbol{\eta})$,

$$W^{(2)}_{\text{t, lat}}(\boldsymbol{\eta}) = M_l \sum_{\beta=1}^{N_t} \eta_\beta \Big[1 - (1 - \sum_{\zeta=1,\zeta\neq\beta}^{N_t} \eta_\zeta)^3\Big]. \tag{4.21}$$

The goal of this form is to non-linearly increase the yield stress for a twin system based on the activation of the other twin systems, i.e., if a region is twinning by one variant, then a hardening term forms for all other twin systems. This hardening term non-linearly increases from 0 (in the case of no twin band $\eta_1 \approx 0$) up to $4M_s$ when the first twin band has fully formed ($\eta_1 \approx 1$). Thus, we can control the penalization of second (or more) twins but still allow their formation through the parameter M_s.

In short, a twin latent energy of the form in equation 4.21 improves twin bands fully forming and is applied in subsequent simulations.

4.2.5 Implementation

The numerical implementation will closely follow Chapter 3 with only a few modifications we mention here. First, after the time discretization of the plastic flow rule, its update at the new time step $(n+1)$ is now,

$$\mathbf{F}^{\text{p}}_{n+1} = \frac{1}{J^d_{\text{p}}}\left(\mathbf{I} + \sum_{\alpha=1}^{N_s} \Delta\gamma^{\text{p}}_\alpha \left[(1 - \sum_{\beta=1}^{N_t} \eta_\beta)\hat{\mathbf{b}}^{\text{p}}_\alpha \otimes \hat{\mathbf{n}}^{\text{p}}_\alpha + \sum_{\beta=1}^{N_t} \eta_{\beta\, n} \hat{\mathbf{b}}'^{\text{p}}_{\alpha\beta} \otimes \hat{\mathbf{n}}'^{\text{p}}_{\alpha\beta}\right]\right)\mathbf{F}^{\text{p}}_n, \tag{4.22}$$

where J_{p} normalizes the plastic update to preserve an isochoric deformation and d is the dimension. Second, we need to introduce ADMM variables (auxiliary variables and Lagrange multipliers) for each twin phase field variable, η_β, to decouple the non-linear and non-local problems in each twin evolution equation. This decoupling will lead to N_t local non-linear problems, which are solved using Newton-Raphson, and N_t linear non-local problems, solved using FFT, to update the phase field variables and their gradients. Lastly, solving mechanical equilibrium and twin/slip evolution is done using the ADMM in Chapter 3 (and discussed in detail by Zhou and Bhattacharya [160]), however now the ordered solution of the different slip/twin systems could lead to differing microstructure — and consequently large effects on

C_{11}	C_{33}	C_{44}	C_{66}	C_{12}	C_{13}	Units
59.72	57.26	17.28	16.96	25.81	21.93	GPa

Table 4.1: Experimentally-determined transversely-isotropic elastic constants of pure Mg at 280 K (Slutsky and Garland, 1957).

the stress-strain response. To mitigate this, we solve the twin and slip systems in order of most violated yield criteria [54, 123].

4.3 Magnesium material parameters

For a full three-dimensional simulation of magnesium we must carefully consider all relevant inelastic systems present, along with the proper anisotropic elasticity, twin/slip hardening, propagation, and phase field variables.

4.3.1 Anisotropic elasticity

Pure magnesium has been shown to have a transverse-isotropic response which we match here by defining the elastic stiffness tensor components, following Slutsky and Garland's [146] experimental measurements, shown in Table 4.1.

4.3.2 Plastic slip

Here we will consider three slip systems: basal, prismatic, and pyramidal $\langle a+c \rangle$. The first system, basal slip, is magnesium's most dominant plastic system due to significantly lower critical resolved shear stresses. The second plastic slip system, prismatic, is frequently observed when activation of basal slip is suppressed [36, 138]. The last system, pyramidal $\langle a+c \rangle$, accommodates compression along the c-axis since the earlier slip systems lie along the basal plane and cannot activate along the c-axis. There are additional slip systems, such as pyramidal $\langle a \rangle$, that can be included; however, it has been found that its effects are similar to the prismatic ones but at considerably higher resolved shear stresses [3, 44]. Additionally, using only basal, prismatic, and pyramidal $\langle a+c \rangle$ slip systems, Agnew *et al.* [5, 6] have already provided realistic results for alloy AZ31B magnesium and reproduced experimental results [7]. Therefore, we choose only to include the basal, prismatic, and pyramidal $\langle a+c \rangle$ systems, shown in Figure 4.1 with directions and planes given using Miller indices. Finally, each system's plastic slip hardening/dissipation parameters are given in Table 4.2 with values motivated from the literature [42, 43].

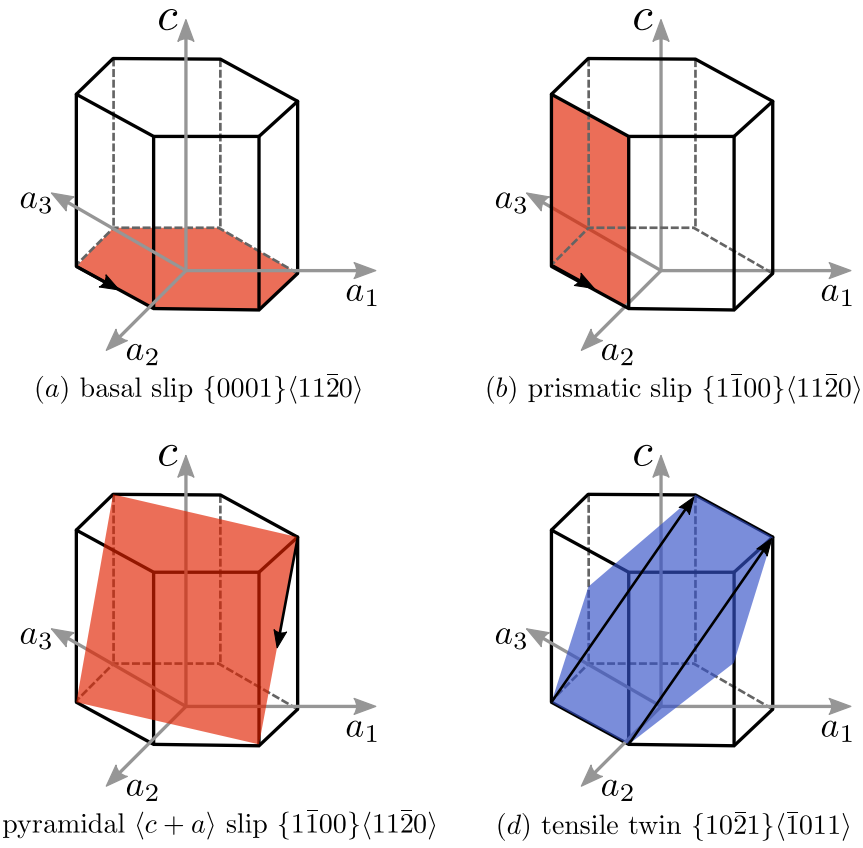

(a) basal slip $\{0001\}\langle 11\bar{2}0\rangle$ (b) prismatic slip $\{1\bar{1}00\}\langle 11\bar{2}0\rangle$

(c) pyramidal $\langle c+a\rangle$ slip $\{1\bar{1}00\}\langle 11\bar{2}0\rangle$ (d) tensile twin $\{10\bar{2}1\}\langle\bar{1}011\rangle$

Figure 4.1: Magnesium inelastic systems accounted for in simulations. (a) – (c) are the dislocation slip systems and (d) is the deformation twinning system.

4.3.3 Deformation twinning

Deformation twinning is the most common inelastic mode in magnesium (when considering c-axis loading), with a considerably lower activation threshold than the non-basal slip systems and the ability to accommodate c-axis deformations. The two types of twin systems are tension and compression, activated under c-axis tension and compression, respectively. Tension twins are the more dominant system of the two due to easier nucleation thresholds and higher mobility. In contrast, compression twins are difficult to nucleate due to their much higher critical resolved shear stress and larger shear strain, as seen experimentally by Brown *et al.* [34] and understood through differences in twinning structures [49]. Thus, we only consider tension twins here, shown in Figure 4.1 along with directions and planes given in Miller indices.

The parameters for tensile twins are motivated by a combination of experimental/atomistic understanding. First, the twinning hardening and dissipation parameters (γ_0^{t}, $\dot{\gamma}_0^{\mathrm{t}}$, τ_0^{t}, m_{t}) are motivated from literature on twin structures and propagation

m_{p}	$\dot{\gamma}_0^{\mathrm{p}}$	τ_0^{p}	σ^{∞}	h	k
		Basal Slip			
0.05	1 1/s	4 MPa	2 MPa	7.1 GPa	0 MPa
		Prismatic Slip			
0.05	1 1/s	4 MPa	85 MPa	9 GPa	2 MPa
		Pyramidal $\langle a+c \rangle$ Slip			
0.05	1 1/s	4 MPa	150 MPa	30 GPa	25 MPa

Table 4.2: Plastic slip hardening and dissipation parameters for magnesium simulations [42, 43].

kinetics [42, 43, 49]. Second, the phase field double well parameter, M_s, is estimated based on surface energy contributions from our model compared to atomistic simulation values for tensile twin boundaries in magnesium.

Assume we have a *single* twin interface in equilibrium under a stress-free state with no plastic slip history. The twin surface energy, Γ, simplifies to an integration of the twin energy over the interface thickness, l,

$$\Gamma = \int_0^l \frac{M_{\mathrm{s}}}{2}\eta^2(\eta-1)^2 + \frac{\alpha}{2}\left\|\nabla\boldsymbol{\eta}\right\|^2 \, d\hat{y}, \tag{4.23}$$

where $\hat{y}$ is along the normal to the twin interface. Since the twin interface thickness is much smaller than any characteristic lengths, we can approximate the surface energy using a linear form of $\eta(\hat{y})$ and a finite difference of $\nabla\eta$ to arrive at,

$$\Gamma = \frac{M_{\mathrm{s}} l}{60} + \frac{\alpha}{2l}. \tag{4.24}$$

Using the fitted twin thickness relationship, $l = 8\sqrt{\frac{\alpha}{M_{\mathrm{s}}}}$, from Section 3.2.4 we can remove the α dependence to arrive at,

$$M_{\mathrm{s}} = \frac{480\Gamma}{47l}. \tag{4.25}$$

Finally, using atomistic results for typical twin boundary surface energies (Γ = 70 mJ/m^2 [125, 151, 153, 158]) and twin interface thickness (chosen to be l = 7 nm — motivated by the fact that twin boundaries can be up to several twin plane distances thick [98, 109]) in magnesium. Combining the experimental and atomistic results, we arrive at M_{s} = 100 MPa.

We will use the surface energy parameter, α, to define a non-dimensional length scale used for implementation. Finally, the latent twin hardening parameter, M_L,

γ_0^{t}	M_s	M_L	α	$\dot{\gamma}_0^{\mathrm{t}}$	τ_0^{t}	m_{t}
			Tension Twin			
0.129	100 MPa	5 MPa	5×10^{-7} Pa·m^2	1 1/s	1 MPa	1

Table 4.3: Twin hardening and dissipation parameters for magnesium simulations from [42, 43, 49, 118], phase field parameters informed from simulations and theory [50, 98, 109, 125, 151, 153, 158].

is kept small to avoid large effects on the nucleation of individual twins. The final twin-related phase-field, hardening, and dissipation parameters are given in Table 4.3.

4.4 Results

Here we present magnesium simulations with multiple twin and slip systems to explore twin-slip interactions. For all simulations, we consider the full 12 slip systems discussed in Section 4.3 and two of the tension twin systems, i.e., $N_s = 12$ and $N_t = 2$. Note that we only consider two tension twins instead of the full six to emphasis the capabilities of the phase field model while keeping the computational cost minimal. Calculations are conducted on a 128^3 grid on a cubic domain of side lengths, $L = 30$ μm and a strain rate of 5×10^{-3} s^{-1}.

4.4.1 Bi-crystal twin transmission

First, we explore twin transmission across misorientated grains by conducting simulations on a bicrystal sample, shown in Figure 4.2. For all simulations, we keep

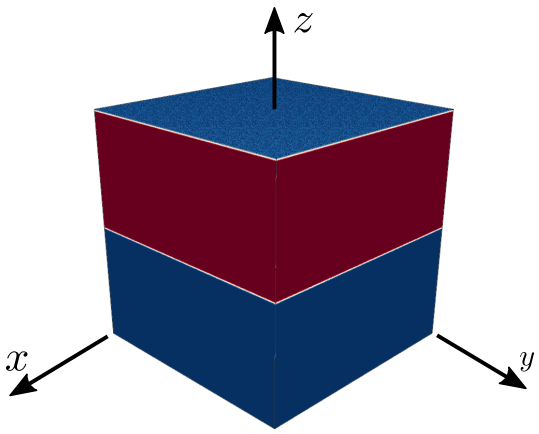

Figure 4.2: Bicrystal sample.

the bottom (blue) grain fixed, with its c-axis aligned with the z-axis, and rotate the

top (red) grain by varying amounts (15°, 30°, and 45°) about the x-axis to arrive at the starting texture. Then, we apply z-axis tension while allowing lateral directions to contract freely to ensure tensile twins dominate the bottom grain's inelastic deformation. Table 4.4 shows the macroscopic Schmid factors for both grains.

x-axis rotation Schmid Factors				
Angle	Tensile twin	Basal slip	Prismatic slip	Pyramidal slip
0°	0.499	0	0	0.446
15°	0.465	0.217	0.029	0.492
30°	0.357	0.375	0.108	0.420
45°	0.203	0.433	0.217	0.251

Table 4.4: Twin and slip Schmid factors for bicrystal simulations.

From the Schmid factors, we expect tensile twinning and pyramidal slip to be the dominant inelastic systems at low angles of grain reorientation, with little to no basal or prismatic slip. Conversely, basal slip becomes the most favorable system at high angles, with the remaining systems being roughly equal. Hence, from a macroscopic Schmid factor perspective, we expect that twins can no longer transmit across the grains as we increase the rotation angle, leaving basal and prismatic slip to accommodate the strains in the top grain.

We conduct tension simulations for each rotation case with an initial twin seed of radius 2.2 μm, inserted in each crystal to assist in twin nucleation. The resulting twin-slip morphology at a strain of 6%, corresponding to shortly after twin nucleation, is shown in Figure 4.3. We see twin bands forming in the bottom grain for all misalignment cases. However, we see bulkier twins forming for higher angles. For low grain misalignment, Figure 4.3 (a) – (d), we see twin bands can transmit to the top grain (though are not able to span the entire grain) with plastic slip hot spots from all systems present near twin interfaces and inside twin bands. As we increase the grain rotation, we see that twin bands can no longer form in the top grain. However, we observe areas near the grain boundary where twins attempt to transmit. Further, the plastic slip becomes more uniform with increasing angle since the bulkier twinned regions decrease the heterogeneity from the twin bands.

To further emphasize the arrest of deformation twinning near the grain boundary, we show the twin configuration at the same instance for the 30° and 45° cases (with a zoomed-in axis) in Figure 4.4. From Figure 4.4 (a), we see that at the intermediate

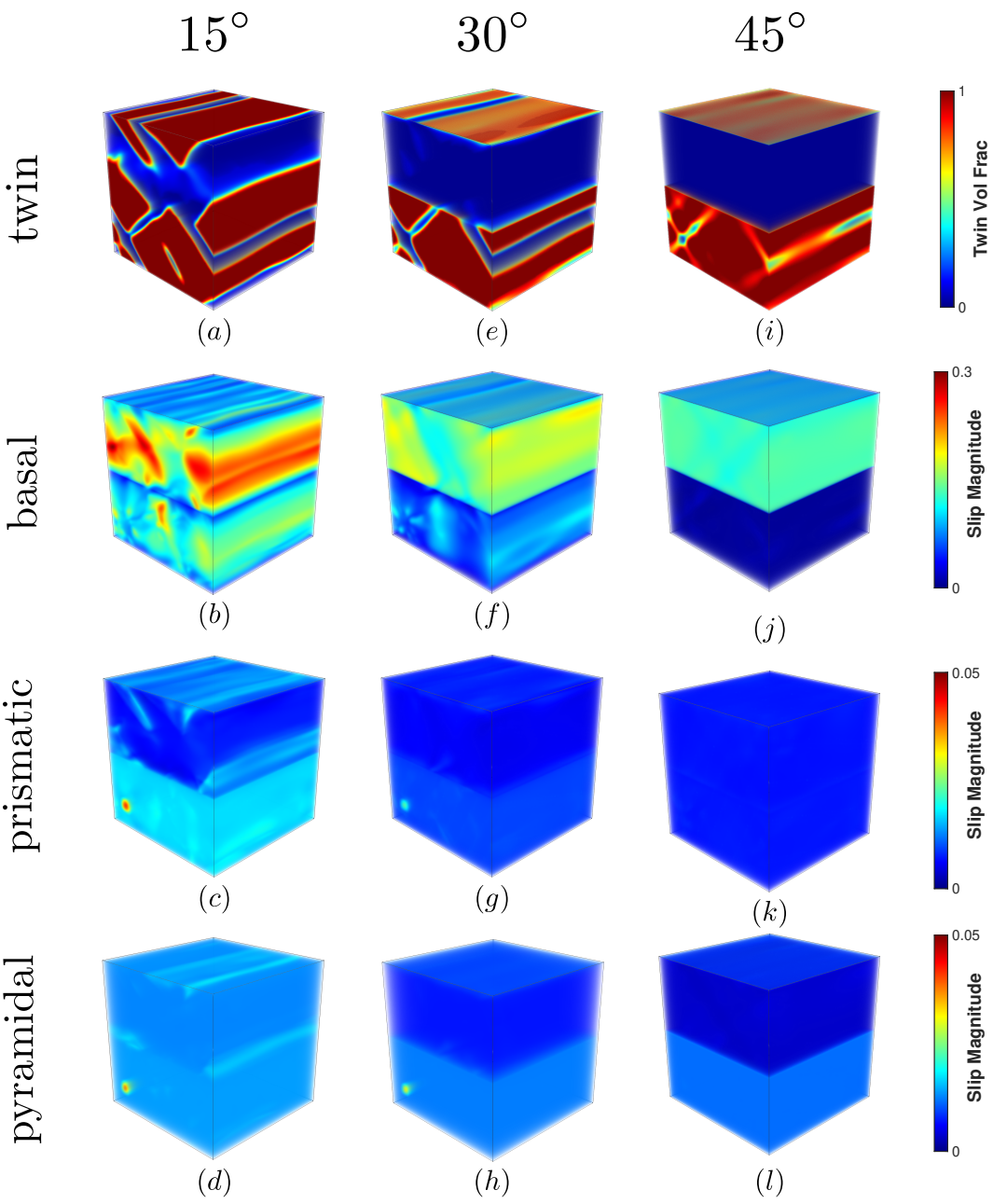

Figure 4.3: Twin-slip configurations for twin transmission through x-axis rotated bicrystal. The twin configuration (a, e, i), basal slip (b, f, j), prismatic slip (c, g, k), and prismatic slip (d, h, l) are shown at a strain of $\varepsilon = 0.06$ for the angles listed.

angle, twin bands (of low twin volume fraction) are propagating from the grain boundary where neighboring twins terminate. These twin spots indicate areas of relatively high twin-resolved shear stress due to the stress heterogeneity created by the grain boundary and twin bands. However, if we look at Figure 4.4 (b), we see a more uniform zero twin activity due to the poor twin alignment mitigating the

effects of stress concentrations in the resolved shear stress.

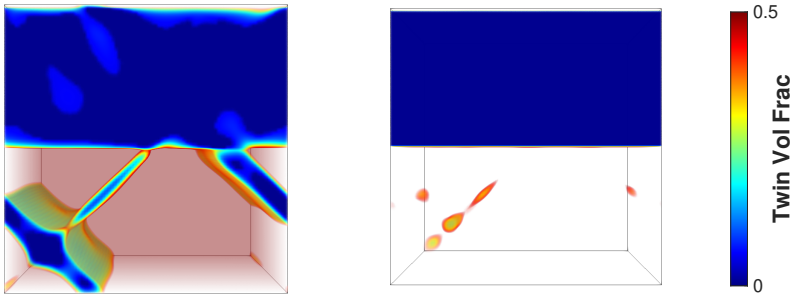

(a) (b)

Figure 4.4: Twin arrest at grain a boundary with (a) 30° and (b) 45° rotation at a strain of $\varepsilon = 0.06$.

Lastly, we compute the average stress and inelastic deformations versus applied strain in Figure 4.5. Looking at the stress-strain curves, Figure 4.5 (c, f, i), we observe a linear elastic region until plastic yielding, after which there is a continued stress increase until twin bands can nucleate, leading to a stress drop. Next, comparing the different misalignment cases, we see a more significant stress drop with an angle increase due to bulkier twin bands forming in the bottom grain. Lastly, for lower misalignment cases, we see the basal slip magnitude (and, to a lesser degree, prismatic and pyramidal) rapidly increasing shortly after twin nucleation. However, as we increase the angle, this rapid slip increase becomes less evident since the bulkier twin bands decrease the twin surface area and the resulting twin-slip interactions at interfaces.

Finally, identical simulations were conducted for y-axis rotations with similar Schmid factor, twin transmission, and slip interaction trends observed.

4.4.2 Twin-slip evolution in polycrystal magnesium specimens

We now present results highlighting the complex microstructure evolution and the interplay between slip and twinning for a polycrystal magnesium sample. Material parameters are given in Section 4.3 unless otherwise specified. We consider a polycrystal of nine grains, shown in Figure 4.6, obtained by Voronoi tessellation from random seeds and angle (axis) of rotation sampled from a uniform distribution between $\pm\frac{\pi}{2}$ ($x-$, $y-$ $z-$ axis). We apply a boundary condition corresponding to a $z-$axis tension (with lateral directions free to contract) up to a strain of 6%.

Note, the orientation mapping in Figure 4.6 is plotting the propensity for slip and

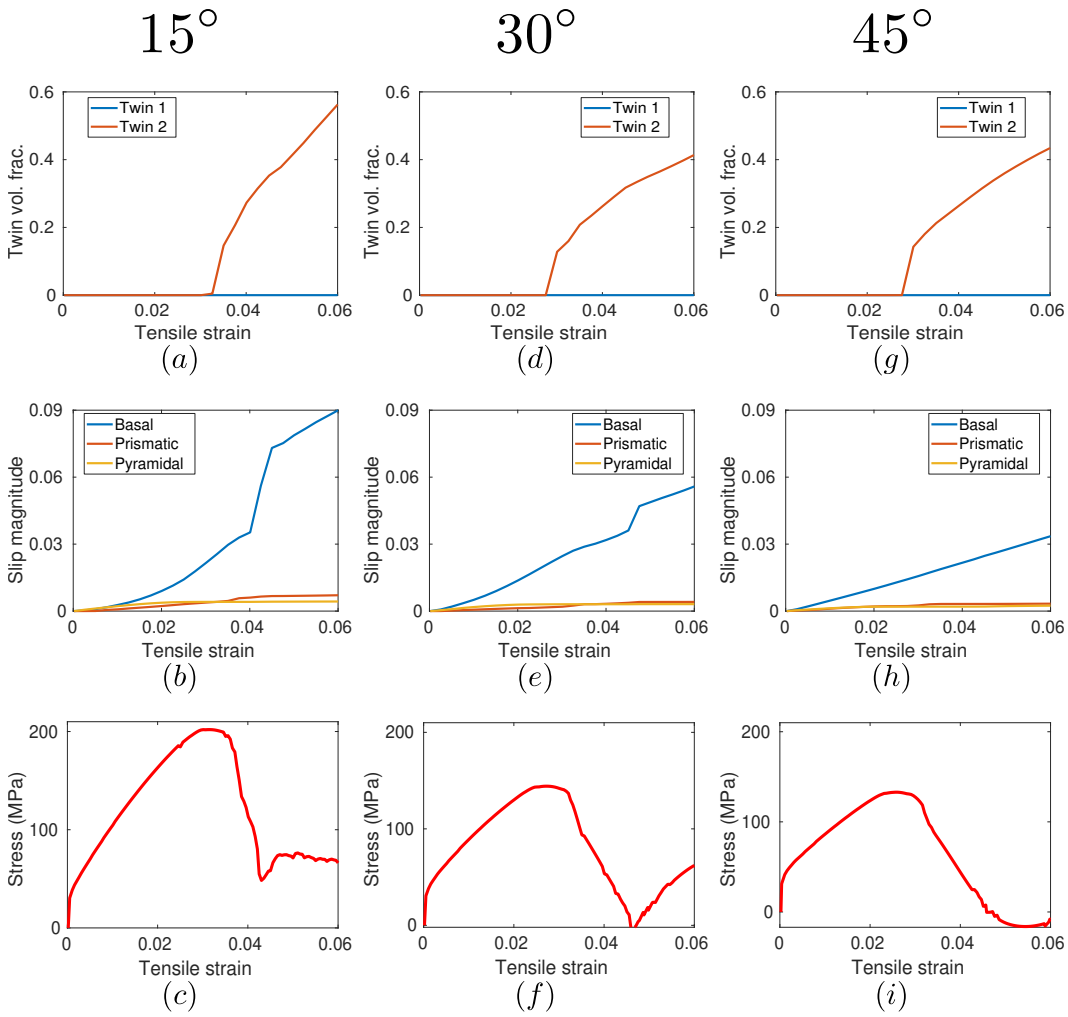

Figure 4.5: Bulk response for bicrystal study. (a, d, g) Average twin volume fraction, (b, e, h) bulk slip magnitudes, and (c, f, i) stress-strain response for misalignment angles shown.

twin, p, computed following Section 3.5.1 as,

$$p = \max_{\beta \in N_t} \left[\bar{\mathbf{F}} : \mathrm{sym}(\hat{\mathbf{s}}_\beta \otimes \hat{\mathbf{m}}_\beta) \right]_+ - \max_{\alpha \in N_s} \left| \bar{\mathbf{F}} : \mathrm{sym}(\hat{\mathbf{b}}_\alpha^{\mathrm{p}} \otimes \hat{\mathbf{n}}_\alpha^{\mathrm{p}}) \right|, \tag{4.26}$$

where $\bar{\mathbf{F}}$ is the applied deformation, $(\hat{\mathbf{s}}_\beta, \hat{\mathbf{m}}_\beta)$ the β^{th} local twin system, $(\hat{\mathbf{b}}_\alpha^{\mathrm{p}}, \hat{\mathbf{n}}_\alpha^{\mathrm{p}})$ the α^{th} local slip system, and the maximum used to determine the most favorable twin and slip system. The resulting values of $-1 \leq p \leq 1$ indicate alignment with a slip (or twin) system if $p = -1$ (or $p = 1$). Although this measure of alignment loses the details of which slip or twin system is most favorable, it provides an easy way to differentiate between slip or twin alignment.

The stress-strain behavior, bulk slip activity, and twin volume fraction are shown in Figure 4.7 along with snapshots of twin and slip evolution in Figure 4.8 for increasing

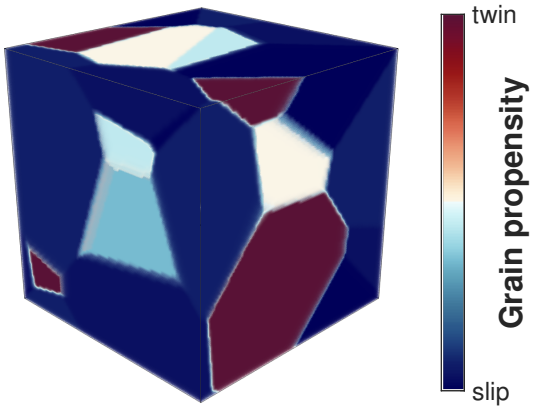

Figure 4.6: Polycrystal (nine grains) sample with color mapping showing propensity for slip (blue) or twinning (red).

strain (left to right). At low strains, $\varepsilon = 0.02$, plasticity is the dominant inelastic mechanism; basal and prismatic slip initiated across several grains — Figure 4.8 (g) and (j) — while the pyramidal slip is concentrated near grain boundaries — Figure 4.8 (m). This slip nucleation is confirmed with bulk slip magnitudes increasing in Figure 4.7 (b) and stress softening in Figure 4.7 (c). The plastic activity increases relatively uniform across grains, with only hot spots near triple grain junctions, until a strain of $\varepsilon = 0.0325$, at which point twinning nucleates — Figure 4.8 (b) and (e). This twin nucleation is again confirmed with an increase in twin volume fraction and a stress drop in Figure 4.7. As the loading continues until the final strain, $\varepsilon = 0.06$, twin bands nucleate/propagate across grains leading to increased plastic heterogeneity — confirmed with a rapid basal (and to a lesser degree prismatic and pyramidal) slip increase after twin bands form.

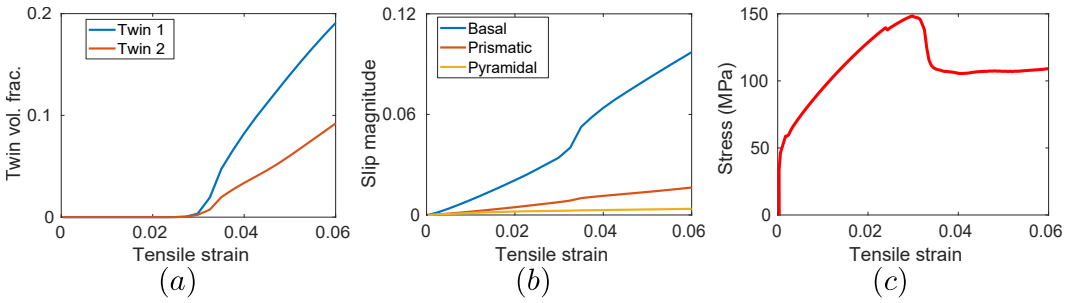

Figure 4.7: Bulk response for nine grain sample. (a) Average twin volume fraction, (b) bulk slip magnitudes, and (c) stress-strain response.

Twin-slip interactions The highly heterogeneous response of slip after twin nucleation, in both favorable and unfavorable grains, points to the cooperation of

twin-slip activity. To explore this interaction, we take a two-dimensional slice of the polycrystal sample and show the basal slip and twin activity at a few strains. Figure 4.9 (a) shows the texture, with labels given for grains of interest, which have a reorientation of 30° and 60° across grains $1-2$ and $1-3$, respectively. Figure 4.9 (b) shows the basal slip magnitude, at a strain of 3% (corresponding to shortly before twin nucleation), with concentrated plastic activity near grain boundaries and inside the slip favored grains 2 and 3. Figure 4.9 (c) shows the twin volume fraction, at a strain of 3.25%, with a twin nucleating at the grain boundary and inside the 1 and 3 grains. Lastly, Figure 4.9 (d) and (e) shows the basal and twin configuration at a strain of 3.5%, where we can see a fully formed twin band and a rapid increase in basal activity inside the twinned domain.

All these points to the cooperation of slip and twinning to address local strain incompatibility. Orozco-Caballero *et al.* has recently experimentally shown the activation of twinning and unfavorable slip near grain boundaries to accommodate drastically different grains. Although we alluded to this in our previous two-dimensional study of phase field twinning (Chapter 3), here, we can show this for a three-dimensional magnesium specimen. Specifically, the activation of both twinning and basal slip at the triple grain junction occurs to accommodate the strain incompatibility introduced by the grain misalignment coupled with the anisotropic elasticity. Lastly, the increase of the basal slip inside and near the twin band (even into the unfavorable grain 1) provides an example of the complex coupling between the twin morphology and plastic deformation.

4.4.3 Texture influence

Starting with the grain configuration from Section 4.4.2, we conduct separate uniaxial tension simulations with different starting textures. The initial textures considered are for fixed angles with (1) grain rotations about the x-axis and (2) grain rotations about the y-axis. These alignments of the grains about an external direction are similar to texture results from cold rolling [145].

The final inelastic configuration and average stress response are shown in Figure 4.10 and 4.7, respectively, for each case (along with the case from Section 4.4.2 repeated). Looking at the twin-slip morphology for each texture, we see complex twin bands that span through/across several grains and plastic slip with peaks near grain and twin interfaces. Comparing the different textures, we see drastically different twin/slip responses due to the grain orientation changes. For x-axis and

y-axis rotations, we see more bulky twin bands and only one tensile twin active (rather than both). Both result from the texture aligning more with one of the tensile twins. We also observed higher concentrations of pyramidal slip in the x and y texture cases for similar reasons as twinning. Comparing the stress-strain curves, we observe similar trends across all textures. However, we see slightly more stress softening and fewer stress drops in the x or y texture than the random texture — both are due to an overall smaller twin volume fraction since only one tensile twin actives. Comparing the bulk slip magnitudes, we see a more rapid slip increase after twin nucleation for the random texture; this is due to only one twin system (with bulkier bands) nucleating in the x and y texture cases.

4.5 Discussion and conclusion

In this study, we have extended the phase field model introduced in detail in Chapter 3 to describe multiple twin and slip systems at the scale of multiple grains. We start by accounting for multiple slip systems through classical crystal plasticity theories and twin systems through multiple phase field variables. Then, we carefully consider detailed twin morphology, nucleation barriers, surface energy, propagation drag, cross hardening, and rate hardening. Finally, we implement the model on graphical processing units following [160] to achieve accelerated computations. This study aims to understand various aspects of the interaction between deformation twinning and dislocation slip observed from the phase field model in polycrystal magnesium specimens. Therefore we use detailed simulations in three dimensions to study twin transmission/arrest at grain boundaries, cooperation of twin-slip to accommodate strain incompatibility and the influence of texture.

We first observe a non-local nature of twinning (and plastic slip) to accommodate grain heterogeneity. This non-local interaction is observed through neighboring grains affecting twin/slip nucleation and morphology. For the bicrystal case, despite the bottom grain remaining unchanged, we observe a transition from lamella-like twin bands to bulkier, grain-spanning twins. The transition is in response to the increased incompatibility across the grains, requiring larger inelastic deformations that eventually slip fails to accommodate. Similarly, the polycrystal case illustrated the same phenomenon, with twin nucleation observed within seemingly less favorable grains. We emphasized the non-local interaction in Figure 4.9 where we see grain boundaries between highly misaligned grains initially promoting basal slip until twinning begins to nucleate to accommodate high strain incompatibilities. These observations qualitatively match studies on the effect neighboring grains and

their plastic deformation have on twin behavior. Orozco-Caballero *et al.* [129] were able to use DIC and EBSD observations to show slip activity in one grain can allow for twin nucleation in the same or neighboring grain. While Lind *et al.* [112] utilized high energy x-ray diffraction microscopy to show that both the nucleation and morphology of twins are highly dependent on neighboring grains, with higher twin volume fraction found inside grains with a higher number of neighbors — effectively increasing the likelihood of cross grain interactions.

Second, we clearly observe the benefits of explicitly computing the twin morphology through increased slip activity at twin interfaces and inside twin bands. In the bicrystal study, during low misalignment, where twins are lamella-like, we notice a highly heterogeneous basal and prismatic slip that disappears as we transition to bulkier twins. This observation indicates that the loss of twin interfaces in the bulkier case leads to a more homogeneous state and diminished high slip areas. While in the polycrystal case, we captured instances of high slip magnitude bands forming inside twin bands, and growing alongside twinning, see Figure 4.9. Both of these observations indicate the highly non-local nature of twin and slip evolution that the phase field model is able to capture near both grains and twin interfaces.

Lastly, we also explored the influence of texture on twin morphology and bulk response through a simple study of three starting microstructures. A key observation is the forming of bulkier twins when the texture is biased to one tensile twin, which leads to different stress and bulk responses. For example, the x-axis rotated polycrystal exhibited bulkier twins, leading to a softer behavior and less rapid changes in slip activity after nucleation. These initial texture studies match studies by Beyerlein *et al.* [22] where thicker (bulkier) twins were observed in grains (or textures) more favorably aligned to a twin variant. However, the influence of texture on twin morphology and resulting stress hardening/softening is a complex topic with many factors affecting observed bulk behaviors (such as grain sizes, grain orientations, plastic history, and loading/boundary conditions). Thus, this study only illustrates the model's capabilities to capture detailed microstructure evolution. We leave more detailed texture studies and quantitative experimental comparisons of the model as future work.

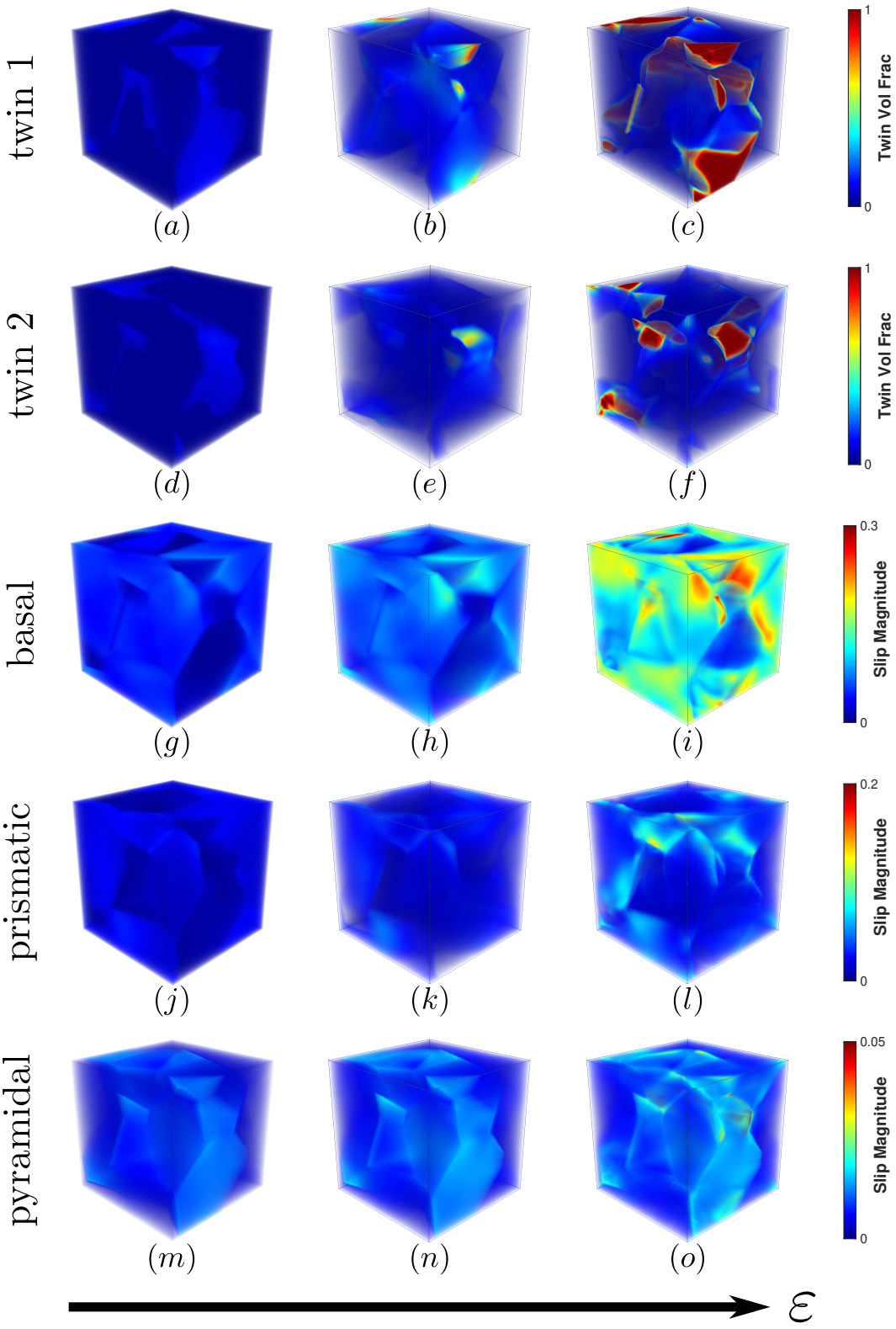

Figure 4.8: Polycrystal magnesium simulation. The configuration for both twin systems (a – c) and (d – f), basal slip (g – i), prismatic slip (j – l), and pyramidal slip (m – n) are shown for strains of $\varepsilon = 0.02,\ 0.0325,\ 0.06$.

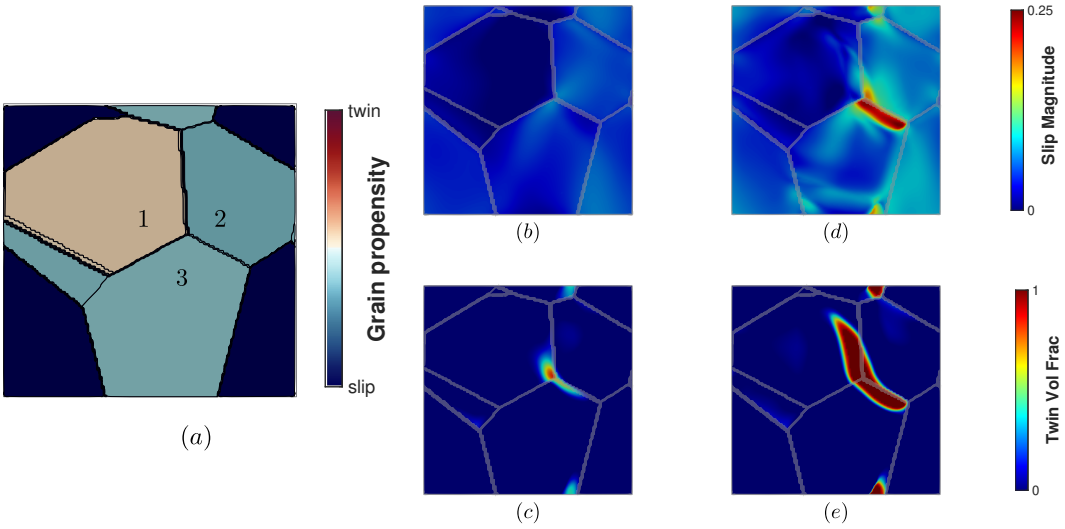

Figure 4.9: Twin-slip nucleation in slice of polycrystal magnesium specimen. (a) Grain texture with grain misalignment across grains $1-2:\ 30^\circ$ and $1-3:\ 61^\circ$. (b) and (d) Basal slip magnitude at strains of $\varepsilon = 0.03$ and $\varepsilon = 0.035$, respectively. (c) and (e) Twin volume fraction at strains of $\varepsilon = 0.0325$ and $\varepsilon = 0.035$, respectively.

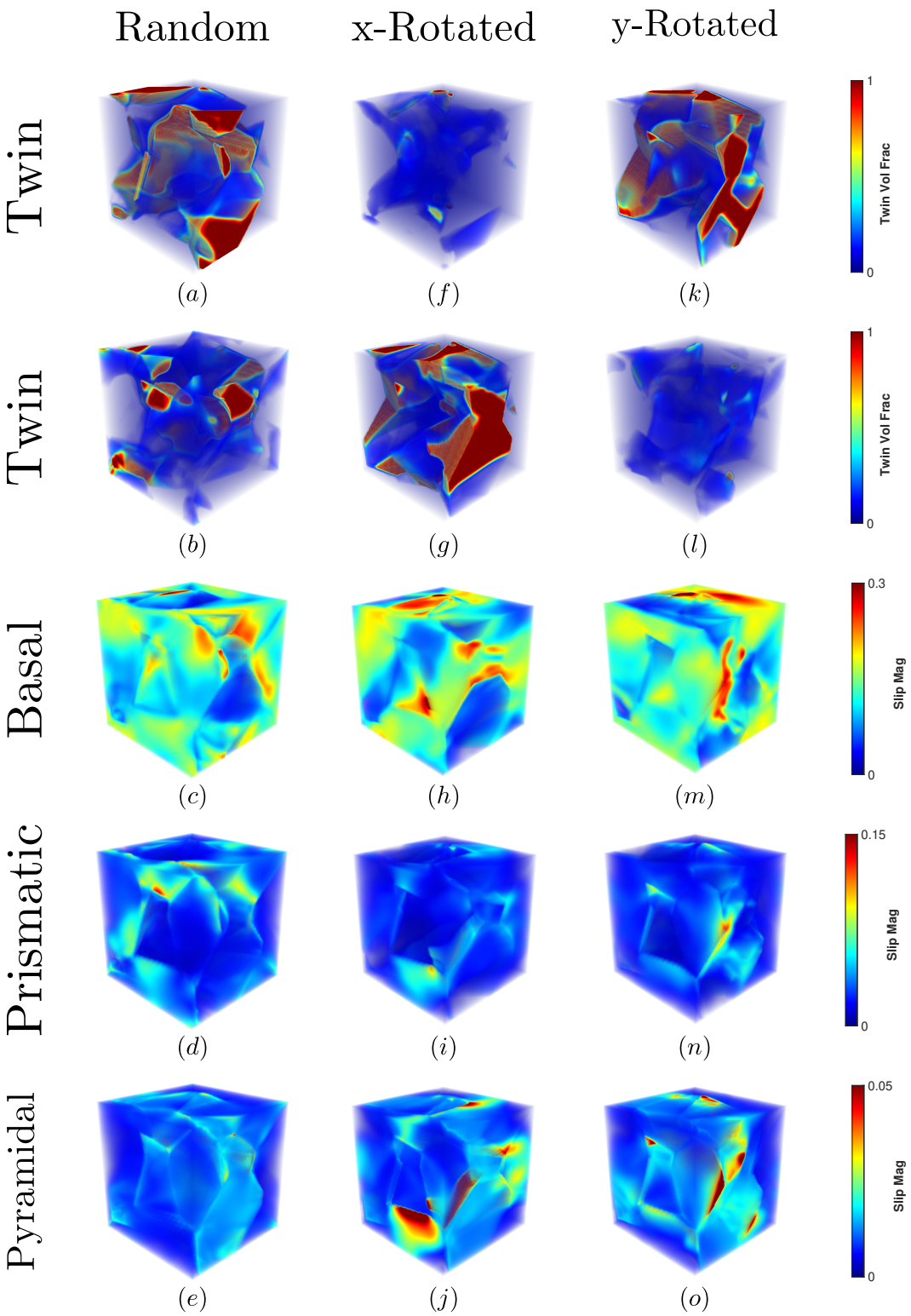

Figure 4.10: Polycrystal texture simulation. The configuration for both twin systems (a – b, f – g, k – l), basal slip (c, h, m), prismatic slip (d, i, n), and pyramidal slip (e, j, o) shown at a strain of $\varepsilon = 0.06$ for the three texture listed.

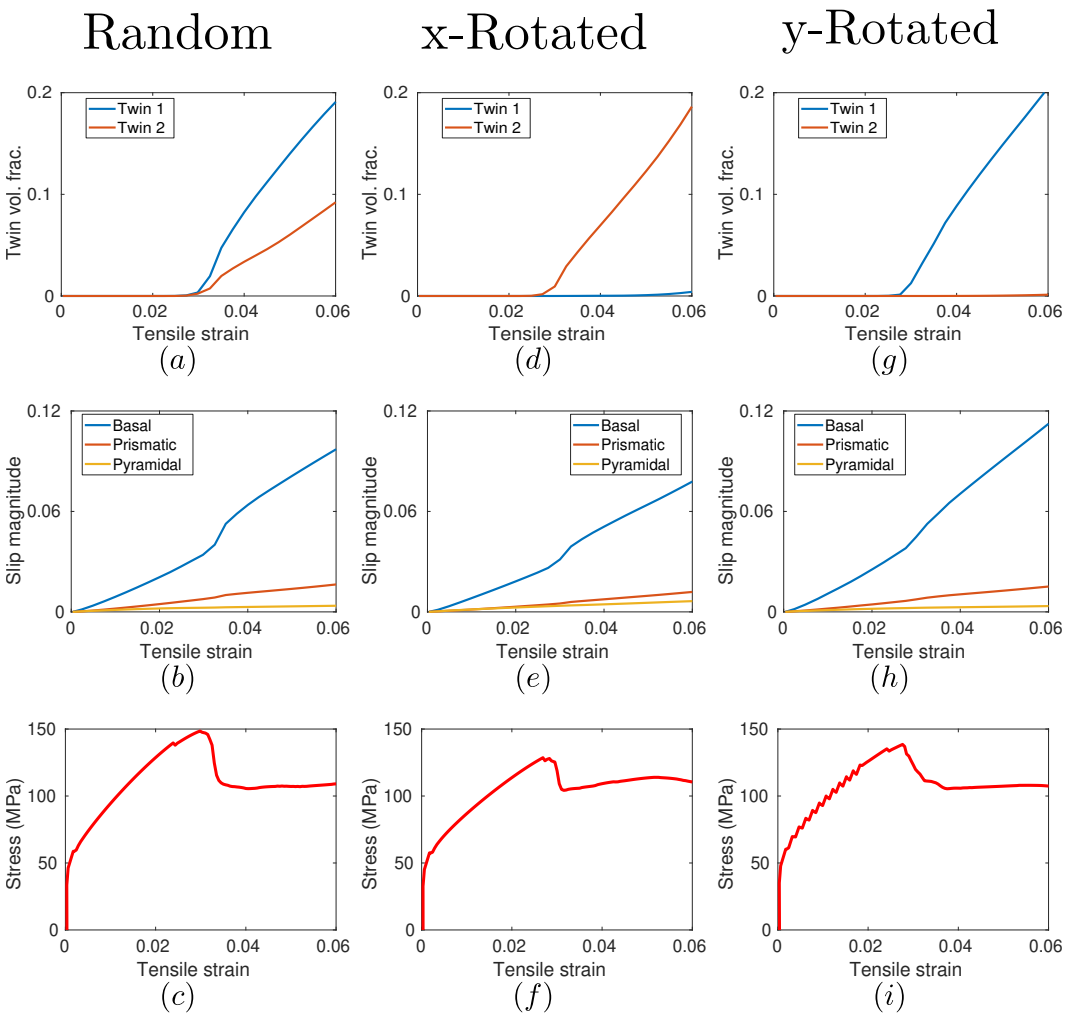

Figure 4.11: Polycrystal texture bulk response. (a, d, g) Average twin volume fractions, (b, e, h) average slip magnitudes, and (c, f, i) stress strain response for the listed initial texture cases.

Chapter 5

LEARNING MACROSCOPIC INTERNAL VARIABLES AND HISTORY DEPENDENCE FROM MICROSCOPIC MODELS

The work presented in this chapter has been adapted from the following publication:

[1] B. Liu, E. Ocegueda, M. Trautner, A. M. Stuart, and K. Bhattacharya. "Learning macroscopic internal variables and history dependence from microscopic models". In: *Journal of the Mechanics and Physics of Solids* (2023), p. 105329. ISSN: 0022-5096. DOI: https://doi.org/10.1016/j.jmps.2023.105329. URL: https://www.sciencedirect.com/science/article/pii/S0022509623001333.

5.1 Introduction

The engineering properties of materials are determined through complex interactions of mechanisms that operate over a range of time and length scales (e.g., [134]). Over the last few decades, the multiscale modeling framework has emerged, providing means of understanding this complexity. The entire range of material behavior is divided into a hierarchy of scales, the relevant phenomenon is identified and modeled at each scale, and the hierarchy is reassembled assuming a pair-wise interaction between the scales (e.g., [66]). Statistical mechanics and the theory of homogenization provide the basis for this pair-wise reassembly: the coarser scale regulates the finer scale while observing the averaged or filtered response from the smaller scale.

Of particular interest in this work is the link between two continuum scales where the physics is specified on a significantly smaller scale than the application scale. Consider, for example, a polycrystalline solid with grains significantly smaller than the overall dimensions, where each grain is governed by crystal plasticity while the solid is subjected to macroscopic loads. The theory of homogenization [19, 131] states that we may solve the balance laws at the application or macroscopic or coarse scale using a constitutive relation that is determined implicitly by solving a problem on a unit cell or representative volume at the microscopic or fine-scale at which the physics is specified. Unfortunately, implementing this framework is prohibitively computationally expensive since one needs to solve a microscopic scale unit cell

problem at each point and time of the macroscopic calculation. This computational cost provides the first motivation for this study.

Also of interest in this work are history and rate-dependent phenomena (like crystal plasticity with hardening and rate dependence). While the history dependence is specified at the microscopic scale, the process of homogenization or averaging over the unit cell adds significant complexity. In particular, heterogeneous strain and strain-rate distributions within the unit cell mean that phenomena at distinct rates interact. Thus, the history dependence at the macroscopic scale can be very different. For example, it is easy to show that a composite material made of constituents governed by a linear Kelvin-Voigt model, where the stress depends only on strain and strain rate, can have infinite memory (i.e., the stress depends on the entire history of strain) at the macroscopic scale (e.g., [63, 144]). In fact, Brenner and Suquet [33] provide examples where the macroscopic response can only be described using a fractional time derivative of the strain. The situation in nonlinear history-dependent phenomena like plasticity is far more complex, and very little is known theoretically. This provides the second motivation for our work.

These issues have motivated a growing body of work in computational mechanics that seeks to use machine learning in multiscale modeling. In an early work, Lefik, Boso, and Shrefler [107] apply machine learning to the multiscale modeling of composite materials. More recently, various researchers have used a recurrent neural network (RNN) to approximate history-dependent behavior. Ghavamian and Simone [65] suggested that an RNN with long short-term memory (LSTM) can be used to describe effective plastic behavior of a representative volume and then be used in FE^2 calculations. They demonstrated it in an "academic example" of a bar governed by isotropic Perzyna viscoplasticity with a periodic line of holes. Mozaffar *et al.* [126] showed that an RNN with gated recurrent units (GRUs) is able to approximate the homogenized behavior of a composite medium consisting of isotropic elastic inclusions in an isotropic rate-independent plastic matrix. Wu *et al.* [154] used an RNN to approximate the overall unit cell behavior of a particulate composite consisting of dilute circular elastic particles in an isotropic matrix undergoing J2 plasticity, isotropic hardening, and no rate-effects, and then used the trained macroscopic (GRU) RNN in macroscopic simulations. Wu and Noels [155] seek to predict macroscopic response and microscopic strain distribution using a (GRU) RNN combined with principal component analysis (PCA) of the strain field. They again apply it to a particulate composite consisting of dilute circular elastic

particles in an isotropic matrix undergoing J2 plasticity, isotropic hardening, and no rate effects. There is a similar study of plasticity in particulate composites by Logarzo, Capuano, and Rimoli [117]. There is also emerging literature on using RNNs to accelerate large-scale finite element calculations (e.g., [28, 83]). One issue in this approach is the complexity of the LSTM/GRU architecture, with a very large number of parameters (e.g., millions in [126]).

In this Chapter, we examine the use of machine learning and, specifically, deep neural networks to harness data generated by repeatedly solving the finer scale model: (i) to gain insights into the history dependence and the macroscopic internal variables that govern the overall response; and (ii) to create a computationally efficient surrogate of its solution operator, that can directly be used at the coarser scale with no further modeling.

We draw inspiration from the established literature on the use of internal or state variable theories in continuum mechanics [72, 141] (and more broadly, the use of order parameters in physics) to develop the architecture for our machine-learned approximation. These theories postulate that all prior deformation history can be represented through state or internal variables that evolve with the deformation. So the stress at any point at any instant of time is determined locally from the deformation gradient and the state variable at that point at that instant using a "stress-strain" relation. Further, the rate of change of the state variable at any point at any instant of time again depends locally on the deformation gradient and state variable at that point at that instant through a "kinetic relation" or "evolution law." Therefore, we introduce two feed-forward neural networks, one for the stress-strain relation and one for the kinetic relation. Importantly, the internal variables are not specified *a priori* but are discovered through training using macroscopic data.

Further, we formulate the approximation in continuous time, and therefore this architecture represents a functional that maps the history of the deformation gradient to the stress. In practice, both the training data and the application involve discretized data, so one could formulate the architecture for the discrete data. However, in such situations, the architecture and the training embed the discretization, providing poor approximation when applied to other discretizations. This is problematic because the training and application of the approximation may involve different time discretizations. This is indeed the case in multiscale modeling since the coarse-scale time step is dictated by the application and the coarse-scale numerical method. We overcome this by formulating the approximation in a time-continuous

manner and then discretizing it as necessary during training and application. An alternate approach in the context of LSTM-based RNNs has recently been proposed by Bonatti and Mohr [28].

We describe the resulting architecture as a recurrent neural operator (RNO). We use the same feed-forward networks at every instant of time, and therefore, we regard this architecture as "recurrent." Further, we use the word "operator" to emphasize the time-continuous formulation. Once discretized in time, the resulting architecture is similar to an RNN. However, it differs from the usual standard LSTM or gated RNNs in how it introduces history. In fact, our architecture is much simpler and requires a significantly smaller number of parameters and, thus, less training data.

Here, we focus on elasto-viscoplastic polycrystals. The behavior of the single crystal is governed by crystal plasticity and, therefore, can be highly anisotropic with rate-dependent evolution. Therefore, we expect the macroscopic behavior to be complex with non-trivial history dependence. We use repeated solutions of the unit cell problem subject to various average deformation gradient trajectories to generate the data in the form of average deformation gradient trajectory and average stress pairs. We use this data to train our approximation and show that the proposed RNO provides an accurate and efficient representation. We examine the insights the RNO can provide into hidden physics from data about the deformation gradient and stress. As already noted, we anticipate a highly complex history dependence, and there is no established method to identify the macroscopic internal variable (or even its dimensionality) either through homogenization theory or experimentally. So even identifying the number of internal variables required to represent the data can be meaningful. In some cases, it is also possible to obtain further insight.

The remainder of the Chapter is organized as follows. Section 5.2 provides the background, proposed architecture, and training procedure. We study an academic example of three-dimensional laminates in Section 5.3. We show that the RNO and training lead to an accurate approximation but with fewer internal variables than that suggested by theory. We explore this with a detailed study of the RNO trained with the macroscopic response and the micromechanical internal variables. Next, we turn to polycrystals in Section 5.4. We study a two-dimensional example where each grain has two slip systems and use data generated by full-field numerical simulations. We show that the RNO can provide a highly accurate surrogate and that the internal variables can provide some insights into the underlying physics. We conclude in Section 5.5 with a discussion on the current work and further studies.

5.2 Background, proposed architecture, and training

We are interested in problems where there is a separation of scales between the scale at which the physics is specified (e.g., the crystal plasticity model at the scale of an individual grain) and the scale of the application (e.g., an impact problem). The theory of homogenization [19, 131] states that we may solve the balance laws at the application scale using a constitutive relation,

$$\Psi : \{F(\tau) : \tau \in (0,t)\} \mapsto \sigma(t), \tag{5.1}$$

that links the macroscopic deformation gradient history to the macroscopic Cauchy stress. This constitutive relation is determined implicitly by solving the fine-scale problem at which the physics is specified on a unit cell or representative volume. The macroscopic deformation gradient history provides the boundary condition for the unit cell problem; the returned macroscopic stress is the average of the stress in the unit cell. See [114] for additional details.

This framework raises two issues. The first concerns the implementation of the framework: the evaluation of this map Ψ is expensive in most problems of interest since the unit cell problem has to be solved at each instant of time (numerically at each time step) at each material point (numerically at each quadrature point). Therefore, it would be useful to have an accurate and inexpensive approximation to evaluate. The second concerns an understanding of the underlying physics. Since the unit cell problem involves solving a complex system of equations, the nature of the dependence of the stress on strain history at the macroscopic scale and whether such history can be encoded into an internal variable is unclear.

In this work, we address these two issues by seeking to approximate the map Ψ using a recurrent neural operator (RNO). Specifically, we consider an RNO approximation of the form,

$$\begin{cases} \sigma(t) = f(F(t), \{\xi_\alpha(t)\}_{\alpha=1}^k), \\ \dot{\xi}_i(t) = g_i(F(t), \{\xi_\alpha(t)\}_{\alpha=1}^k) \quad i = 1, \dots k \end{cases} \tag{5.2}$$

where $f : \mathbb{R}^{d\times d} \times \mathbb{R}^k \to \mathbb{R}^{d\times d}_{\text{symm}}$ and $g_i : \mathbb{R}^{d\times d} \times \mathbb{R}^k \to \mathbb{R}$ are neural networks. We call $\{\xi_\alpha(t)\}_{\alpha=1}^k$ the *internal variables*, and these encapsulate the history. We do not identify the internal variables *a priori*; instead, they are identified as a part of the training process. Note that while the architecture maps trajectories to trajectories, the architecture is local and identifies the stress simply on the value of the deformation gradient and internal variable at that instance, making the proposed architecture causal.

We now make a series of comments about the RNO and its training.

Discretization and discretization independence The RNO (5.2) is an operator that maps functions (deformation gradient history over a time interval) to a matrix (stress). However, in practice, both training and application data are discretized in time, although they do not necessarily have the same discretization/resolution. In order to construct an architecture that is independent of the time discretization, we use the following forward Euler discretization: for a time-discretization with time-steps $\{(\Delta t)_n\}$, we evaluate the RNO at the n^{th} time step to be

$$\begin{cases} \sigma^n = f(F^n, \{\xi_\alpha^n\}_{\alpha=1}^k), \\ \xi_i^n = \xi_i^{n-1} + (\Delta t)_n \, g_i(F^n, \{\xi_\alpha^{n-1}\}_{\alpha=1}^k) \quad i = 1, \dots k. \end{cases} \tag{5.3}$$

In this work, we use uniform discretization so that $(\Delta t)_n = (\Delta t)$ is independent of n. For this approximation to be meaningful, it should be independent of the time discretization. In other words, we should be able to train it at one time discretization and use it at another time discretization without any loss of accuracy. This is also important in practice because the training data may need to be generated at smaller time steps due to the underlying microscale physics compared to that used in a macroscale application.

RNO architecture and training We train the RNO, i.e., identify the parameters of the neural networks f, g_i and the internal variables $\{\xi_\alpha\}_{\alpha=1}^k$, using data generated by the numerical solution of the unit cell problem. Specifically, we repeatedly solve the unit cell problem to obtain various realizations of the map

$$\Psi_T : \{F(t) : \tau \in (0, T)\} \mapsto \{\sigma(t) : t \in (0, T)\}. \tag{5.4}$$

for some fixed $T > 0$.

We use fully connected neural networks [105] to model the feed-forward functions f and g. By default, we assume that each of f and g is comprised of four intermediate linear layers, each with 200 nodes, with a nonlinear activation function applied using the scaled exponential linear unit (SELU) [96]. The networks are trained with the ADAM optimization algorithm [95] with an error corresponding to a mean of relative L^2 norms over the time interval,

$$\text{error} = \frac{1}{S} \sum_{s=1}^{S} \left(\frac{\int_0^T |\sigma_s^{\text{truth}}(t) - \sigma_s^{\text{approx}}(t)|^2 dt}{\int_0^T |\sigma_s^{\text{truth}}(t)|^2 dt} \right)^{1/2} \tag{5.5}$$

where "truth" and "approx" refers to the unit cell solution and RNO prediction, respectively, S indexes over the considered strain paths, and $|\cdot|$ is a Frobenius norm of the stress tensor.

Training data A crucial issue in generating numerical data is to balance the cost of generating the data with the need to sample sufficient input (average deformation gradient histories) to provide an accurate enough approximation for the inputs encountered in application. This leads to the question of identifying an optimal distribution of input data, which remains an active area of research. In our planned application to impact problems, we anticipate encountering trajectories of macroscopic deformation gradients that vary smoothly with time but change directions arbitrarily. To this end, we divide $(0, T)$ into M intervals $(\Delta t)^m = t^m - t^{m-1}, m = 1, \dots M$ where $0 = t^0 < t^1 < \cdots < t^M = T$ and set $(F_{ij})^m = (F_{ij})^{m-1} + (\nu_{ij})^m F_{\max}\sqrt{(\Delta t)^m}$, $i, j = 1, \dots, d, i \le j$ where $(\nu_{ij})^m \in \{-1, 1\}$ follow a Rademacher distribution for each i, j. We take $F_{ij}(t)$ to be the cubic Hermite interpolation of $\{(t^m, (F_{ij})^m)\}$. We take $T = 1$, $M = 100$, and random time intervals drawn from a uniform distribution. We clarify that the subintervals $(\Delta t)^m$ used here to determine loading paths are distinct from the time step (Δt) we use to train or use the RNO.

Internal variables In our formulation, we have to decide *a priori* the number k of internal variables (though not the internal variable themselves). Our approach is to train the neural network separately for various numbers of internal variables and then test the resulting approximation over a set of test data. We find that the test error initially decreases with increasing k but then saturates beyond a particular value. In fact, we find that the transition from decrease to saturation is sharp. We take the value of k at this sharp transition as the number of internal variables present.

As already noted, the internal variables have no inherent meaning. In fact, it is easily verified from (5.2) that any reparametrization or smooth one-to-one and onto change of variables $\{\xi_\alpha\} \to \{\eta_\alpha\}$ of the form

$$\eta_i = \varphi_i(\{\xi_\alpha\}) \tag{5.6}$$

yields an equivalent RNO:

$$\begin{cases} \sigma(t) = \hat{f}(F(t), \{\eta_\alpha(t)\}_{\alpha=1}^k), \\ \dot{\eta}_i(t) = \hat{g}_i(F(t), \{\eta_\alpha(t)\}_{\alpha=1}^k) \quad i = 1, \dots k \end{cases} \tag{5.7}$$

where

$$\hat{f}(F, \{\eta_\alpha\})_{\alpha=1}^k) = f((F, \{\varphi_\alpha^{-1}(\{\eta_\beta\}_{\beta=1}^k)\})_{\alpha=1}^k),$$
$$\hat{g}_i(F, \{\eta_\alpha\})_{\alpha=1}^k) = \sum_{j=1}^k \frac{\partial \varphi_i}{\partial \xi_j}(\{\eta_\alpha\}_{\alpha=1}^k) g_j((F, \{\varphi_\alpha^{-1}(\{\eta_\beta\}_{\beta=1}^k)\})_{\alpha=1}^k).$$

This invariance also has implications on the training: the same data can produce different (but equivalent) choices of the internal variable depending on the initialization.

Internal or state variable theories The form of the RNO (5.2) is similar to the internal or state variable theories that are widely used to describe inelastic behavior in continuum mechanics and physics [72, 141]. We may regard the learned internal variables as those representing the state of the material; we take the first of the two equations to be the stress-strain relation and the second to be the kinetic relation for the evolution of the state variables. However, the choice of state variables postulated in theories of mechanics reflects physical intuition, while those in the RNO reflect the behavior of the training data and are not unique due to the invariance under reparametrization (5.6).

Thermodynamic and symmetry restrictions In this work, we do not impose any thermodynamic or material symmetry restrictions on the functions f, g_i in (5.2). Physical laws and mathematical well-posedness require the constitutive relations to satisfy some thermodynamic restrictions. In our setting, we expect the constitutive stress function, f, to be the derivative of a quasiconvex strain energy functional, while we expect the evolution laws, g_i, to be dissipative (or the derivative of a non-negative and convex dissipation potential). Similarly, in some problems, we may know *a priori* the overall material symmetry. For example, in the polycrystals, we study in Section 5.4, we expect the overall behavior to be isotropic. It is possible to build architectures with these conditions (e.g., [119] for dissipative processes and [16] for hyperelasticity). We do not do so here. However, since our data is generated from numerical solutions of well-posed problems, we anticipate the model automatically learning such restrictions from the data. For example, Liu *et al.* demonstrated in [114] that a PCA-Net automatically learns isotropy from the data. We discuss this further in Section 5.5.

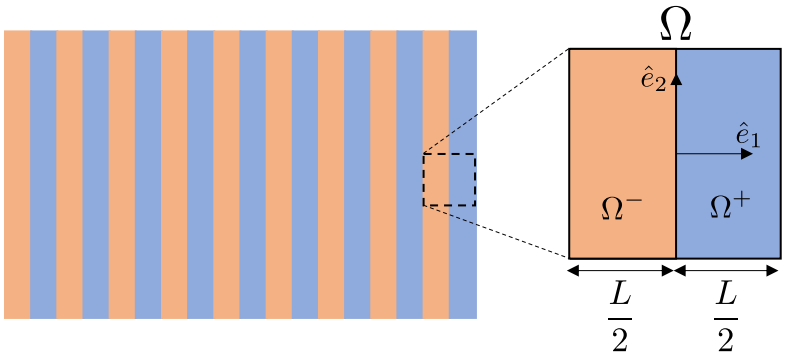

Figure 5.1: A laminate composite and the unit cell domain.

5.3 Elasto-viscoplastic laminated composite

We first start with a study of a laminated composite with alternating layers of equal width of two different elasto-viscoplastic materials at the microscopic scale. We postulate a plasticity model in infinitesimal strain limit at the microscopic scale, solve these equations repeatedly over a unit cell subjected to various (average) strain trajectories as the boundary condition, and calculate the corresponding stress trajectory. We then use the resulting pairs of average strain and average stress trajectories to train the RNO.

The governing equations in the unit cell are

$$\varepsilon = \frac{1}{2}(\nabla u + \nabla u^T), \quad \nabla \cdot \sigma = 0, \tag{5.8}$$

$$\sigma = \mathbb{C}(\varepsilon - \varepsilon^p), \quad \dot{\varepsilon}^p = \frac{3}{2}\frac{s}{\bar{s}}\dot{q}, \tag{5.9}$$

$$-\bar{s} + \sigma_0 \left(H(q) + \left(\frac{\dot{q}}{\dot{q}_0} \right)^m \right) \geq 0, \quad \dot{q} \geq 0, \tag{5.10}$$

$$\left(-\bar{s} + \sigma_0 \left(H(q) + \left(\frac{\dot{q}}{\dot{q}_0} \right)^m \right) \right) \dot{q} = 0 \tag{5.11}$$

where u is the displacement, ε the strain, σ the stress, $\mathbb{C}$ the elastic modulus (assumed to be isotropic with Lamé and shear modulus λ and μ respectively, and homogeneous), ε^p the plastic strain, q the accumulated plastic strain, s the deviatoric stress, $\bar{s} = \sqrt{\frac{3}{2}}|s|$ the effective stress ($|\cdot|$ denoting Frobenius norm), σ_0 the yield strength, $H(q)$ is the isotropic strain hardening function,

$$H(q) = \begin{cases} 1 & \text{no strain hardening} \\ 1 - \exp\left(-h\frac{q}{\sigma_0}\right) & \text{exponential strain hardening} \end{cases} \tag{5.12}$$

for some hardening coefficient h, $\dot{q}_0$ the reference plastic strain rate, and m the rate-hardening exponent. The first line describes the strain-displacement and the equilibrium equation, the second line the stress-strain and evolution of the accumulated plastic work, the third line the yield criterion and the flow rule, and the fourth line the Kuhn-Tucker conditions (rewritten from line three). We further assume plane stress conditions,

$$\sigma_{i3} = 0, \tag{5.13}$$

and prescribe the history of the in-plane average strain $\bar{\varepsilon}(t)$. We solve the governing equations subject to the prescribed history of the in-plane average strain $\langle \varepsilon_{\text{inplane}}(x,t)\rangle_x = \bar{\varepsilon}(t)$, and find the average in-plane stress $\bar{\sigma}(t) = \langle \sigma_{\text{inplane}}(x,t)\rangle_x$. We are interested in understanding the map

$$\{\bar{\varepsilon}(\tau) : \tau \in [0,t]\} \mapsto \bar{\sigma}(t). \tag{5.14}$$

For our laminate, the unit cell consists of two layers shown in Figure 5.1. All the parameters of the model in each of the two layers (such as rate-hardening m, for example) are distinguished by the use of $\pm$ ($m^{\pm}$ for example). We look for a solution to the governing equations (5.8-5.11) that is uniform in the strain, plastic strain, stress, and accumulated plastic strain in each region ($\varepsilon^{\pm}$,$\varepsilon^{p\pm}$, $\sigma^{\pm}$, $q^{\pm}$, respectively). The first two equations (5.8) are automatically satisfied in the interior of each region and reduce to the jump conditions on the interface

$$\varepsilon^{+} - \varepsilon^{-} = a \otimes \hat{e}_1 + \hat{e}_1 \otimes a, \quad (\sigma^{+} - \sigma^{-})\hat{e}_1 = 0. \tag{5.15}$$

We can use this condition along with the plane-stress condition to conclude that

$$a_1 = \frac{\mu}{\lambda + 2\mu}\left(\varepsilon_{11}^{\mathrm{p}+} - \varepsilon_{11}^{\mathrm{p}-}\right), \quad a_2 = \varepsilon_{12}^{\mathrm{p}+} - \varepsilon_{12}^{\mathrm{p}-}, \quad a_3 = \varepsilon_{13}^{\mathrm{p}+} - \varepsilon_{13}^{\mathrm{p}-} = 0. \tag{5.16}$$

Given the average strain history $\bar{\varepsilon}(t)$, we can now solve (5.9 – 5.11) to obtain the average stress history $\bar{\sigma}(t)$ and obtain the map (5.14). Note that we have four state variables in each region ($\varepsilon_{11}^{p,\pm}, \varepsilon_{12}^{p,\pm}, \varepsilon_{22}^{p,\pm}, q^{\pm}$) for a total of eight state variables.

5.3.1 No strain hardening

Looking at the no strain hardening case first, we only have six internal variables ($\varepsilon_{11}^{p,\pm}, \varepsilon_{12}^{p,\pm}, \varepsilon_{22}^{p,\pm}$) in the formulation, i.e., no accumulated plastic strain $q^{\pm}$. We consider various combinations of material parameters representing both small and large plastic contrast; the values are given in Table 5.1. We generate data by picking

Elasticity: $\mu = 24$ GPa, $\mu = 25$ GPa					
Plasticity:					
Case	σ_0^+ (MPa)	σ_0^- (MPa)	m^+	m^-	$\dot{q}_0^\pm$ (s^{-1})
MH (green)	500	500	0.2	0.2	1
M1 (blue)	250	500	0.1	0.2	1
M2 (red)	100	500	0.04	0.2	1
M3 (yellow)	50	500	0.02	0.2	1
M4 (purple)	250	500	0.4	0.2	1

Table 5.1: Material parameters used for laminates along with labels (and colors) used for plotting.

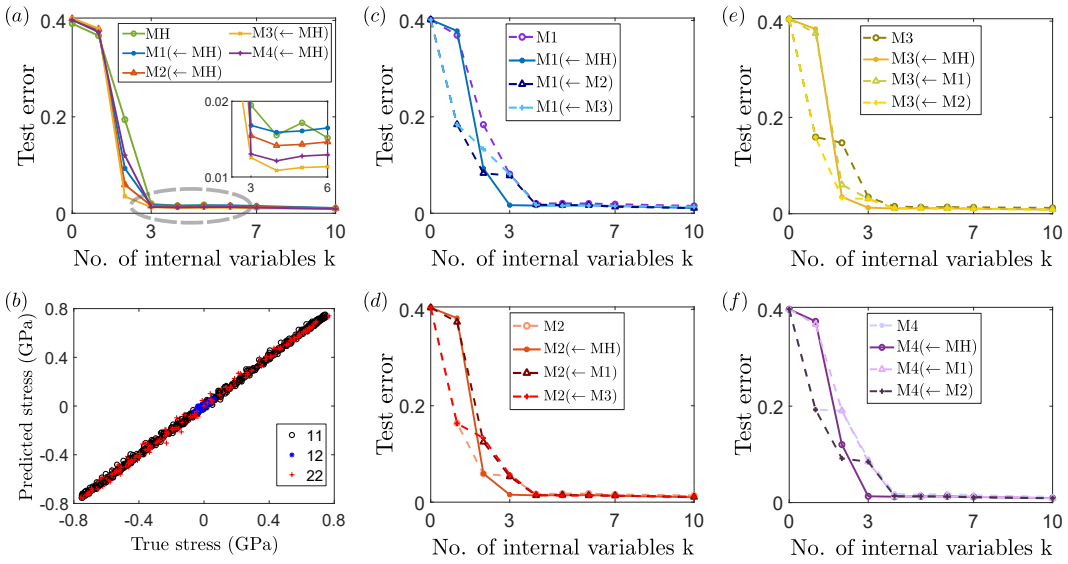

Figure 5.2: Approximating an elasto-viscoplastic laminate with no-strain hardening with a recurrent neural operator. (a) Training RNOs with various numbers of internal variables. In each case, we train the homogeneous material (MH) and then use transfer learning. The notation A ($\leftarrow B$) indicates the case A was trained using transfer learning from B. (b) Comparison of the ground truth and RNO prediction of the stress for eight arbitrarily chosen test strain trajectories for the case M3 with three internal variables. (c–f) Training RNOs with various numbers of internal variables both directly and with transfer learning.

average strain histories (applying the approach described in Section 5.2 to each strain component with a maximum strain of 33%) and computing the resulting stress histories. We generate 800 trajectories, using 640 for training and 160 for testing.

Figure 5.2 describes the results of training an RNO for the various cases. Figure 5.2(a) shows the test error as a function of the number of internal variables for each of the choices of material parameters. Here, we fix the number of internal variables, train the homogeneous material (MH), and then use transfer learning — defined as using the trained RNO for MH as a starting point for training other models — for the four cases (M1–M4) corresponding to different material parameters. In each case, we see a sharp decline in error at two internal variables and a further (often more modest) drop in error when we increase from two to three internal variables. Increasing the number of internal variables beyond three has little effect. Further, the relative test error is small, approximately 1-1.5% relative error in each case. Figure 5.2(b) compares the "truth" versus the predictions of the trained RNO with three internal variables for the high contrast case M3. Again, we see that the errors are very small. The results are similar in other cases.

Figure 5.2(c–f) studies the ability to train an RNO with and without transfer learning. In each of the cases, M1–M4, we train the RNO with a fixed number of internal variables and then apply transfer learning from the other material cases. In each case, direct training suggests the need for four internal variables. However, transfer learning from the homogeneous case (MH) always leads to three internal variables. This shows that the training can get stuck in local minima, a phenomenon which is not uncommon in neural networks in general, and may have a more marked effect when data volume is low [57, 92, 111, 142, 143]. Starting from the homogeneous case (MH) puts the RNO in a suitable basin and leads, in the experiments we have conducted, to a better local minimizer.

The approximation of the elasto-viscoplastic behavior by an RNO with three internal variables as demonstrated in Figure 5.2(a) (or four as seen in Figure 5.2(c–f)) is surprising in a system with six internal variables. The possibility that the training process gets stuck in a local minimum would lead to a larger, not a smaller, number of internal variables. Instead, the good approximation suggests that the equations of the system force the six state variables in the model ($\{\varepsilon_{ij}^{p,\pm}(t)\}$ which we refer to as model variables in this section to distinguish them from the learned internal variables of the RNO) to close proximity of a three dimensional manifold. Similarly, notice that the test error decreases with the contrast MH–M3. This is also surprising as one would expect larger fluctuations with higher contrast.

We examine the range of values the model variables take using an auto-encoder to gain insight into these observations. Briefly, an auto-encoder is a deep neural net-

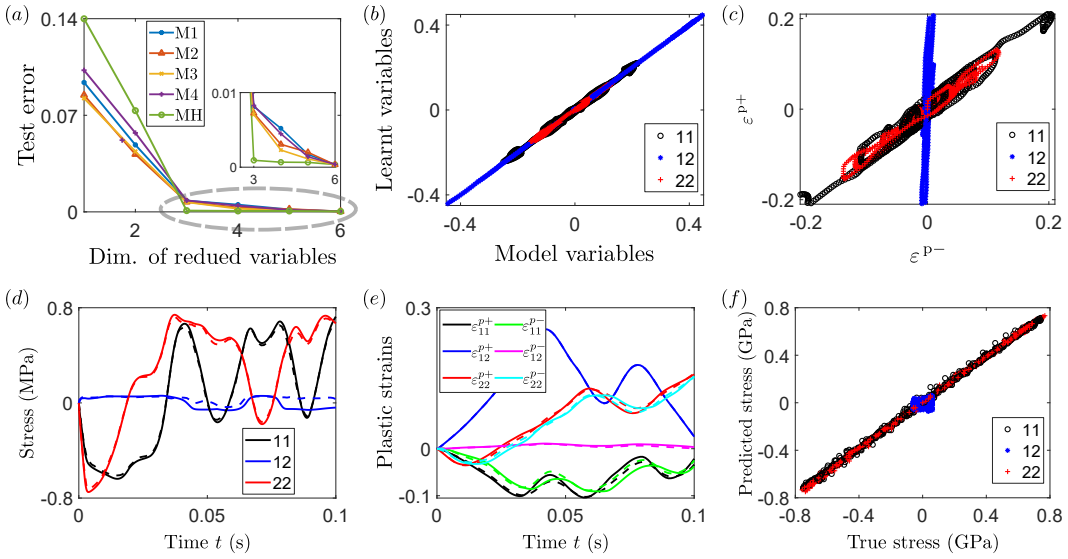

Figure 5.3: Reducing the number of the model variables using an auto-encoder. (a) The error of approximating the model variables (state variables in the original laminate model) with an auto-encoder for various reduced dimensions. (b) Comparison between the computed values of the model variables and the recovered values from the trained auto-encoder for eight arbitrarily chosen trajectories in the test data for the case M3 with three reduced variables. (c) The computed values of the model variables in the the two layers for eight arbitrarily chosen trajectories in the test data for the case M3. (d) Comparison of the computed stress response (solid) with the learnt stress response (dashed) for a typical test trajectory for the case M3. (e) Comparison of the computed plastic strains model variables (solid) with the reconstructed plastic strain (dashed) for a typical test trajectory for the case M3. (f) Comparison of the computed stress with the learnt stress for eight test trajectories for the case M3.

work approach to dimension reduction. It is a deep neural network approximation of the identity map on some data in $\mathbb{R}^n$; it has a symmetric structure and an intermediate layer with a small latent dimension $m < n$. In other words, we may think of the auto-encoder as a map $A : \mathbb{R}^n \to \mathbb{R}^n$ such that $A = \psi_{\text{AE}} \circ \phi_{\text{AE}} \approx id$ on some set of data where $\phi_{\text{AE}} : \mathbb{R}^n \to \mathbb{R}^m, \psi_{\text{AE}} : \mathbb{R}^m \to \mathbb{R}^n$ are neural networks. For any $x \in \mathbb{R}^n$, we call $\phi_{\text{AE}}(x) \in \mathbb{R}^m$ the reduced variables. If we are able to successfully train an auto-encoder on the data, it means that for any data point, $x \approx \psi_{\text{AE}}(\phi(_{\text{AE}}(x))$; the reduced variable $\phi(x)$ "encodes" all the information in the data [105]. In other words, the n-dimensional data lives on a m-dimensional manifold.

We take each of the trajectories and take the values of the model variables at each computed instant t, $\{\varepsilon^{p,\pm}(t)\}$, as a six-dimensional data point. Since we generate 800 trajectories, each with 100 time steps, we have a rich data set of 8×10^4 data

points. We use 6.4×10^4 (corresponding to 640 trajectories) of these for training an auto-encoder, consisting of one layer with 50 nodes in both the encoding and decoding portions, and 1.6×10^4 for testing. We train auto-encoders with varying reduced dimensions. The results are shown in Figure 5.3. We see that in Figure 5.3(a) that for all cases, the results are well approximated with a reduced dimension of three using a relative reconstruction error,

$$\text{error} = \frac{1}{S} \sum_{s=1}^{S} \frac{\left| \varepsilon_s^{p\pm,\,\text{model}} - \varepsilon_s^{p,\,\text{learned}} \right|}{\left| \varepsilon_s^{p\pm,\,\text{model}} \right|} \tag{5.17}$$

where s indexes the 8×10^4 data points and $|\cdot|$ denotes an l^2 norm of the six-dimensional data points $\{\varepsilon^{p,\pm}(t)\}$. Figure 5.3(b) compares the actual values of the model variables and those that are reconstructed from the reduced variables. We observe good reconstruction, indicating that the auto-encoder is able to correctly encode the model variables. All of this leads us to the conclusion that the equations of the system force the six model variables to (the close proximity) of a three-dimensional manifold in all cases. This agrees with what we anticipated from the RNO.

We explore this further in Figure 5.3(c) by comparing the values of the model variables (plastic strain) in the + layer with that in the − layer. Figure 5.3(c) shows that the 11 and 22 components of the plastic strain are almost equal in both layers while the 12 component in the (harder) − remains relatively small. This observation provides a heuristic insight into why we only need three internal variables in the RNO approximation. When the imposed strain is small, the response is largely elastic, and therefore one does not need internal variables. When the imposed strain is large (so that the plastic strain is much larger than the elastic strain), the strain compatibility $(5.15)_1$ forces the 22 and 33 components of plastic strain to be approximately equal, $\varepsilon_{22}^{p,+} \approx \varepsilon_{22}^{p,-}, \varepsilon_{33}^{p,+} \approx \varepsilon_{33}^{p,-}$. Since the plastic strain is trace-free (isochoric), $\varepsilon_{33}^{p,\pm} = -\varepsilon_{11}^{p,\pm} - \varepsilon_{22}^{p,\pm}$, and we conclude that the 11 component of the plastic strains are also equal, $\varepsilon_{11}^{p,+} \approx \varepsilon_{11}^{p,-}$. Furthermore, the stress continuity condition $(5.15)_2$ means that the 11, 12 components are the same and that the stress can only differ in the 22 component. This limits the fluctuation in the deviatoric stress, and we expect plastic yield in the softer layer (+ layer) to dominate over the other. Since only the 12 components of plastic strain can differ from one another, we expect the value in the softer + material to be significantly larger than that in the harder − material, $\varepsilon_{12}^{p,+} >> \varepsilon_{12}^{p,-}$. In short, at large strains, we only need

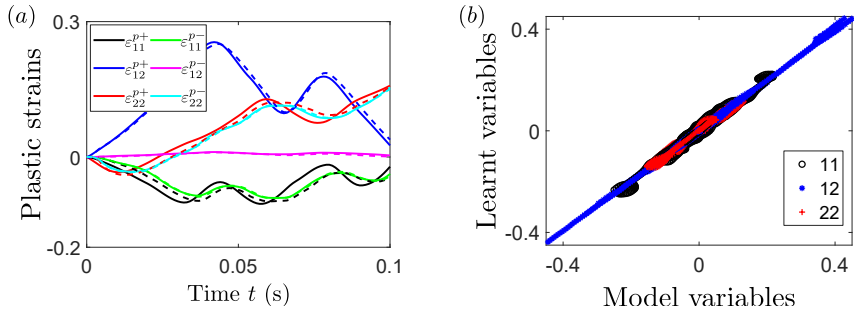

Figure 5.4: Reconstructing the micromechanical model variables from the macroscopic internal variables for the case M3. Comparison between the computed values of the model variables and the recovered values from the RNO internal variables for (a) an arbitrarily chosen trajectory and (b) eight arbitrarily chosen trajectories.

information from the softer layer, and thus only three internal variables. Further, this approximation improves when we have higher contrast.

The fact that the reduced variables encode the model variables suggests that they can be used as internal variables in an RNO. So we again train an RNO of the form (5.2) with three internal variables ($k = 3$) set to be the reduced variables learned by the auto-encoder. To elaborate, let $\phi_{\text{AE}} : \varepsilon^{p,\pm} \to \zeta$ denote the trained auto-encoder from the model variables $\varepsilon^{p,\pm} \in \mathbb{R}^6$ to the reduced variables $\zeta \in \mathbb{R}^3$. So, for any trajectory, at any instant, we use $\{\bar{\varepsilon}(t), \phi_{\text{AE}}(\varepsilon^{p,\pm})(t)\}$ as input and $\{\bar{\sigma}(t), \dot{\overline{\phi_{\text{AE}}(\varepsilon^{p,\pm})}}(t)\}$ as outputs to train a neural network approximation for the map

$$\Phi : \begin{cases} \sigma = f(\bar{\varepsilon}, \zeta), \\ \dot{\zeta} = g(\bar{\varepsilon}, \zeta). \end{cases} \tag{5.18}$$

We train this map on a training data set consisting of 100 time steps across 800 trajectories, with an architecture of 6 layers and 400 nodes, and test it against a test data set consisting of 100 time steps across 200 trajectories. The overall error is 2.39%. Figure 5.3(d) compares the actual computed stress response (solid line) with the learned response (dashed line) for a typical test trajectory. Figure 5.3(e) compares model variables (solid line) with those reconstructed from the learned map (5.18) and the auto-encoder for a typical test trajectory. Specifically, for a given strain trajectory, we predict the stress σ and ζ using the learned map (5.18) and then reconstruct the plastic strains from the learned auto-encoder $\psi_{\text{AE}}(\zeta)$. Figure 5.3(f) repeats the stress comparison for eight trajectories chosen arbitrarily from the test data.

Recall from Section 5.2 that the internal variables have no inherent meaning and

that reparametrization can lead to an equivalent set of internal variables. In the passage above, we identified one set of internal variables by training the RNO purely from the macroscopic strain trajectory to the stress trajectory map and an alternate set by reducing the dimension of the microscopic or model variables using an auto-encoder. The fact that both sets can approximate the macroscopic response suggests that they are equivalent sets of internal variables. We conclude this section by studying the converse. Figure 5.4 shows that the internal variables, learned by training the RNO purely from the macroscopic strain trajectory to stress trajectory, can reconstruct the micromechanical model variables. We train a neural network from the internal variables to the model variables. Figure 5.4 shows that it provides a good representation. We should note, however, that this ability of the internal variables to learn the model variables may be very particular to the case of the laminate — in general, the map from the micromechanical variables in high dimension to the macroscopic internal variables in low dimension may not be invertible.

5.3.2 Exponential strain hardening

We repeat the analysis conducted in Section 5.3.1 for the exponential strain hardening case. Figure 5.5(a–c) shows the results of training an RNO for the homogeneous case (MH) and the case M3 with an exponential hardening coefficient of $h = 1$ (MH–EH and M3–EH). We see in Figure 5.5(a) that we need four internal variables (in contrast to the case of no hardening, where we needed only three). Furthermore, we observe that the final error is still low, $1 - 1.5\%$ for both cases. Figure 5.5(b) shows that transfer learning (as defined in the preceding subsection) starting from the homogeneous material with no hardening leads to a better approximation even for the homogeneous case. Figure 5.5(c) compares the ground truth and RNO output for eight test trajectories for the case (M3–EH) with four internal variables. Figure 5.5(d–f) explores using an auto-encoder to learn the reduced variables from the eight model variables. We see in Figure 5.5(d) we need four reduced variables consistent with the RNO, and in Figure 5.5(e) that these are able to correctly recover the model variables for the (M3–EH) case with a reduced dimension of four. Figure 5.5(f) compares the model variables in one layer with that in the other for the (M3–EH) case. As before, we see that the 11 and 22 components of the plastic strain are almost equal, and the 12 component in the + layer dominates over that in the − layer (the same argument holds). The hardening variable q in the + layer also dominates, but not as much; still, the values in the two layers are proportional to each other,

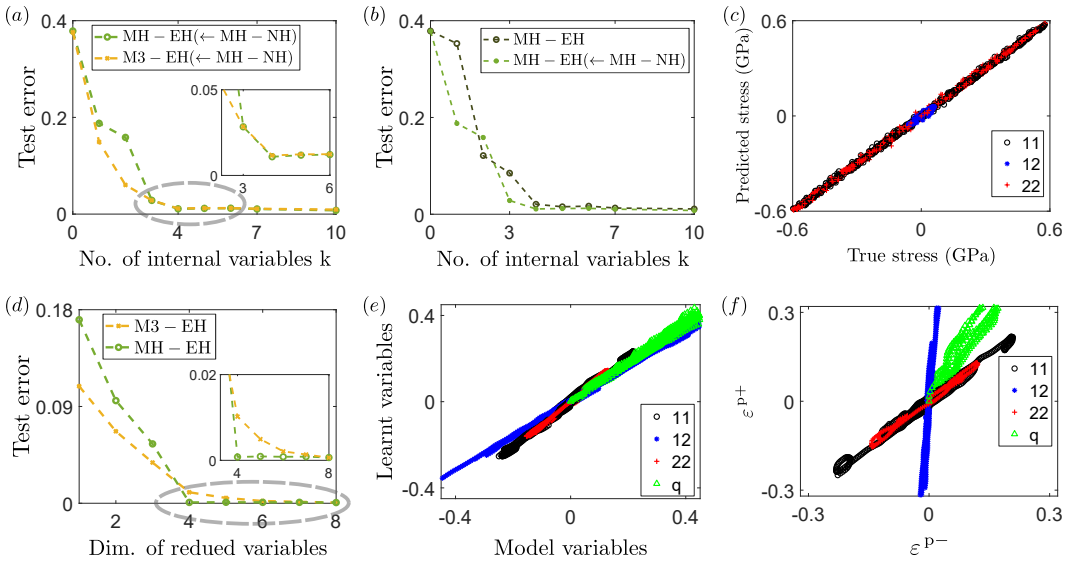

Figure 5.5: Approximating an elasto-viscoplastic laminate with exponential strain hardening. (a–c) Learning the strain history to stress history map with a recurrent neural operator: (a) Training RNOs with various numbers of internal variables. In each case, we train the homogeneous material with no hardening (MH–NH) and then use transfer learning. (b) Training RNOs with various numbers of internal variables both directly and with transfer learning. (c) Comparison of the ground truth and RNO output for eight test strain trajectory for the case M3-EH with four internal variables. (d–f) Reducing the number of the internal variables using an auto-encoder: (d) The error of approximating the model variables (state variables in the original laminate model) with an auto-encoder for various reduced dimensions. (e) Comparison between the computed values of the model variables and the recovered values from the trained auto-encoder for eight arbitrarily chosen trajectories in the test data for the case M3–EH with a reduced dimension of four. (f) The computed values of the model variables in the the two layers for eight arbitrarily chosen trajectories in the test data for the case M3–EH.

meaning that we need only one value to describe the overall behavior.

In summary, we find that the RNO trained only on macroscopic stress-strain data provides an accurate approximation of the actual response of a laminated composite. Further, the training process shows that we require half the number of internal variables than one would expect, and an analysis of the micromechanical fields shows that the governing equations force the micromechanical variables to the proximity of a low dimensional manifold.

5.4 Elasto-viscoplastic polycrystals

We now consider a two-dimensional polycrystalline medium comprising 32 randomly oriented grains generated using periodic Voronoi tessellation [64]. We assume that each grain is an elasto-viscoplastic material with two slip systems. We adopt the two-scale framework introduced in Section 5.2, generate data using a unit cell problem, and then use this data to train the RNO approximation.

The data is generated according to the microscopic model (crystal plasticity) described in Section 2.1 with two slip systems, i.e., $N_s = 2$. The elastic energy density, W_{e}, of each grain will follow a compressible neo-Hookean, which in two dimensions is,

$$W^{\mathrm{e}}(\mathbf{F}^{\mathrm{e}}) = \frac{\mu}{2}\left(\frac{\operatorname{tr}\mathbf{F}^{\mathrm{e}\,T}\mathbf{F}^{\mathrm{e}}}{\det\mathbf{F}^{\mathrm{e}}} - 2\right) + \frac{\kappa}{2}(\det\mathbf{F}^{\mathrm{e}} - 1)^2. \tag{5.19}$$

While the plastic work hardening W_{p}, that depends on the accumulated plastic activity in the slip systems ϵ_i^{p}, will take the form

$$W^{\mathrm{p}} = \sum_{i=1}^{N_s} \sigma_i^{\infty}\left(\epsilon_i^{\mathrm{p}} + \frac{\sigma_i^{\infty}}{h_i}\exp\left(-\frac{h_i\epsilon_i^{\mathrm{p}}}{\sigma_i^{\infty}}\right)\right) + \frac{1}{2}\sum_{i,j=1}^{N_s}\epsilon_i^{\mathrm{p}}\mathcal{K}_{ij}\epsilon_j^{\mathrm{p}}, \tag{5.20}$$

where the first term is associated with self-hardening and the second term is latent hardening. Above, μ and κ are the shear and bulk moduli; σ_i^{∞} is the ultimate strength and h_i the hardening parameter on the i^{th} slip system; and K_{ij} is the latent hardening matrix with zero diagonal entries.

The evolution of the slip activity is governed by the dissipation potential

$$\Psi^*(\gamma) = \sum_{i=1}^{N_s}\frac{\tau_{0,i}^{\mathrm{p}}\dot{\gamma}_{0,i}^{\mathrm{p}}}{m_i+1}\left(\frac{|\dot{\gamma^{\mathrm{p}}}_i|}{\dot{\gamma}_{0,i}^{\mathrm{p}}}\right)^{m_i+1} \tag{5.21}$$

where $\tau_{0,i}^{\mathrm{p}}$ is the critical resolved shear stresses, $\dot{\gamma}_{0,i}^{\mathrm{p}}$ the reference shear rate, and m_i the power rate hardening parameter for the i^{th} slip system.

Finally, the governing equations follow that described in Section 2.1 with implementation following the accelerated computational micromechanics framework [160]. We consider several material cases with various rate hardening or strain hardening parameters shown in Table 5.2 and generate independent data sets of deformation gradient and stress pairs.

The compressible neo-Hookean elasticity model used (equation 5.19) at the microscale leads to a natural decomposition of the Cauchy stress into hydrostatic and

Elastic: all cases							
μ = 19 GPa, κ = 48 GPa							
Slip system 1							
Case	b_1	n_1	$\tau^{\mathrm{p}}_{0,1}$ (MPa)	$\dot{\gamma}^{\mathrm{p}}_{0,1}$ (s^{-1})	m_1	σ^{∞}_1 (MPa)	h_1 (MPa)
PH,P1,P2	(1, 0)	(0, 1)	100	1	0.05	2	7100
P3	(1, 0)	(0, 1)	100	1	0.05	50	100
P4	(1, 0)	(0, 1)	100	1	0.05	100	100
P5	(1, 0)	(0, 1)	100	1	0.05	100	100
Slip system 2							
Case	b_2	n_2	$\tau^{\mathrm{p}}_{0,2}$ (MPa)	$\dot{\gamma}^{\mathrm{p}}_{0,2}$ (s^{-1})	m_2	σ^{∞}_2 (MPa)	h_2 (MPa)
PH	(1, 1)	(-1, 1)	100	1	0.05	2	7100
P1	(1, 1)	(-1, 1)	100	1	0.25	2	7100
P2	(1, 1)	(-1, 1)	100	1	0.5	2	7100
P3	(1, 1)	(-1, 1)	100	1	0.05	50	100
P4	(1, 1)	(-1, 1)	100	1	0.05	100	100
P5	(1, 1)	(-1, 1)	500	1	0.25	500	100

Table 5.2: Material parameter cases used for polycrystals unit cell simulations in two dimensions.

deviatoric components

$$\sigma^{\mu}(F^{\mu}, F^{p,\mu}) = -p(\det F^{\mu})I + \sigma^{\mathrm{dev},\mu}(F^{\mu}, F^{p,\mu}) \tag{5.22}$$

where we use the superscript μ to emphasize that this holds at the microscopic scale, and the fact that $\det F^{p,\mu} = 1$. It follows that at the macroscopic scale,

$$\sigma = -\langle -p(\det F^{\mu})\rangle I + \langle \sigma^{\mathrm{dev},\mu}(F^{\mu}, F^{p,\mu})\rangle = -pI + \sigma^{\mathrm{dev}}. \tag{5.23}$$

Now, since $\det F^{p,\mu} = 1$, the pressure at any point in the unit cell is independent of the plastic strain at that point. So, it is independent of the history of that point. However, the overall stress distribution and, therefore, the overall hydrostatic pressure can depend on the distribution of the plastic strain in the unit cell. Therefore, the overall hydrostatic pressure can develop history dependence from the evolution of the plastic strain distribution. Still, we expect the deviatoric stress to be much more sensitive to history. Therefore, we fit the hydrostatic pressure and deviatoric stress separately: in other words, we train an RNO to learn the hydrostatic pressure and another independent RNO to learn the deviatoric stress — or, we can think of them as one RNO with two disjoint parts.

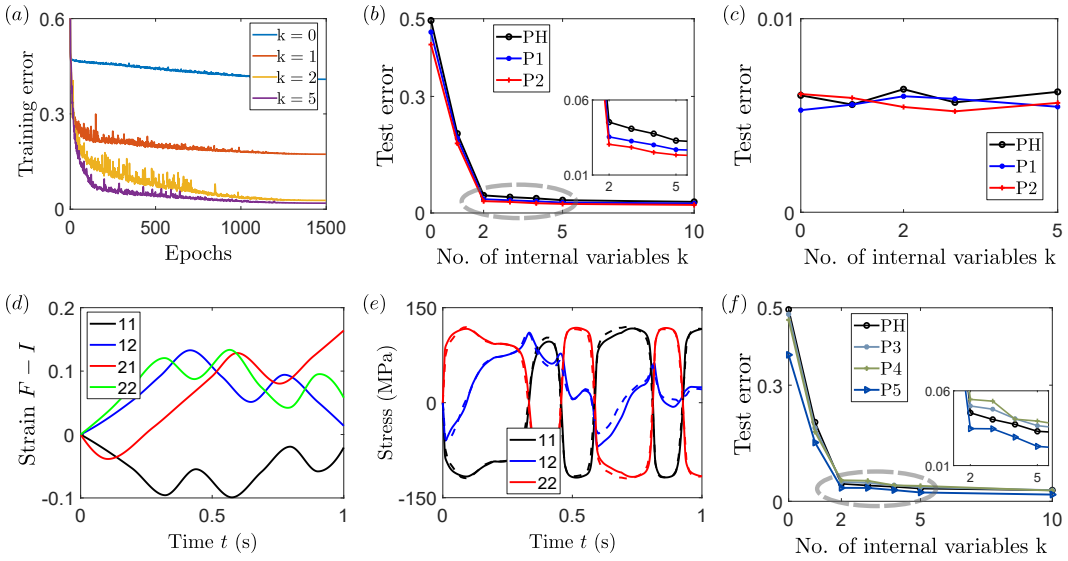

Figure 5.6: Approximating two dimensional polycrystalline elasto-viscoplasticity with a recurrent neural operator. (a) Training RNOs with various numbers of internal variables with increasing epochs. (b) Test error of the trained RNOs of the deviatoric stress with various number of internal variables and rate hardening cases. (c) Test error of the trained RNOs of the hydrostatic pressure with various number of internal variables and rate hardening cases. (d) A typical average deformation gradient history input from the test data. (e) Comparison of the resulting deviatoric stress history for the test data (solid) and the prediction of the RNO with two internal variables (dashed) for case PH. (f) Test error of the trained RNOs of the deviatoric stress with various number of internal variables and strain hardening cases.

We generate data associated with 500 trajectories for various combinations of material parameters. We use 400 trajectories for training and 100 trajectories for testing. Again, for each case, we train the model with various numbers of internal variables. The results are shown in Figure 5.6. Figure 5.6(a) shows the decrease of the training error for the deviatoric stress with the number of training epochs for case PH. We see that the error decreases rapidly, and we obtain convergence with about 1500 epochs. The results are similar in other cases.

Figure 5.6(b) shows the test error in learning the deviatoric stress for the PH and P1–P2 material cases shown in Table 5.2. In each case, we see that the RNO with no internal variables has a large error, but the error reduces with one and two internal variables. Increasing the number of internal variables beyond two does not reduce the error. Moreover, the relative error is small, $3-5\%$. Thus, we conclude that the data is well-represented with two internal variables. Figure 5.6(c) shows the corresponding results for the hydrostatic pressure: we see no dependence of the

error on the number of internal variables, and the error is small (0.6%). Therefore, we conclude that the hydrostatic pressure has no history dependence. Figure 5.6(d) shows a typical deformation gradient trajectory, and Figure 5.6(e) compares the 'truth' (solid line) and the learned (dashed line) stress trajectory for the PH material case. Note that the stress shown is only the deviatoric component. Again, the learned response provides a very good approximation for the data. Finally, we study the effect of strain hardening in Figure 5.6(f): we again observe that we obtain a good approximation with two internal variables; increasing the number of internal variables beyond two does not provide any better approximation.

In summary, the RNO is able to provide a highly accurate surrogate for 2D crystal plasticity. Further, we only require two state variables for various choices of parameters. In two dimensions, deviatoric stresses and isochoric stretches associated with plasticity lie on a two-dimensional manifold. Therefore, the fact that we can represent the strain vs. stress trajectory with two hidden variables is significant. At the same time, we do not know how general this is and discuss this further in Section 5.5.

5.5 Discussion

In this study, we have proposed exploiting a recurrent neural operator (RNO) of the form (5.2) as a surrogate for a fine-scale model in multi-scale modeling of history dependent materials. The architecture of the RNO builds in causality in that the stress at any instant of time depends only on the prior history of the deformation. The history is represented using an internal variable; thus, the stress can be evaluated locally in space and time. The architecture of the RNO is consistent with the common formulation of constitutive relations using internal variables or state variables in continuum mechanics [72, 141]. We may regard the internal variables to be those variables that describe the state of the continuum, $(5.2)_1$ as the stress-strain relation for a given state of the continuum, and $(5.2)_2$ as the kinetic relation that describes the evolution of the state of the continuum. However, a crucial point is that we do not specify *a priori* what the internal variables are but seek to learn them from the stress-strain data.

Although we have explored multi-scale modeling problems in the context of elasto-viscoplasticity with crystal plasticity as the fine-scale model, the framework and the methodology are broader and can be used in other settings where we have (numerical or experimental) information about the map from the history of deformation to the

stress. Therefore, we can use it in other two-scale settings like atomic-continuum transitions and granular materials. Further, it can also be used to identify constitutive behavior from experimental data provided we have a sufficiently rich data set concerning the map from the history of deformation to the stress.

In formulating this study, we recognize that the macroscopic behavior can be an operator from one function space (deformation gradient over an interval of time) to a tensor (though there may be examples where this is also a function space). This means we want the trained model to be independent of the resolution (time step) at which the training data is presented and the trained model is used. In other words, the training data can be at one resolution, but we can use the trained model accurately at every resolution. This is crucial for using this model in multiscale modeling since we may generate training data from the microscopic model at one (generally fine) resolution but may want to use the trained model in macroscopic calculations at different (generally coarse) resolutions. Separate calculations have been conducted to illustrate the resolution-independence of the RNO architecture (5.2) in [113] as well as how this independence results from careful consideration on the choice of architecture.

An important and interesting question concerns the number of state or internal variables one should use. In the case of elasto-viscoplastic laminates, Section 5.3, the theory suggests six (eight with hardening) internal variables are necessary. However, we empirically find that we need three (four with hardening) internal variables, i.e., we trained RNOs with various numbers of internal variables and found that three (four, respectively) is the smallest number that gives rise to a good approximation. We, therefore, studied the state variables in the micromechanical model and learned that the governing equations forced the six (respectively eight) model variables to be confined close to a three (respectively four) dimensional manifold. In the case of elasto-viscoplastic polycrystals, we find empirically through our training procedure that the number of internal variables is related to the dimension of the isochoric manifold — two in two-dimensional example shown here and five in a three-dimensional example explored in [113]. This is somewhat unexpected. A typical empirical elasto-viscoplastic law in two dimensions has two variables for the plastic strain, one for the isotropic hardening and two for the kinematic hardening. The fact that we are able to fit complex loading paths, exhibiting both isotropic and kinematic hardening and using only two variables, suggests that either there is some redundancy in classical empirical models or that there are particular simplifying

aspects of the crystal plasticity single crystal model that we use to generate the data.

Another research topic is the connection between the field variables in the micromechanical calculations and the internal variables learned from the macroscopic response. Here, we train our RNO using only macroscopic stress-strain data following the framework of homogenization or multiscale modeling where the large scale provides the control and the small scale returns the average. However, our micromechanical simulations have a lot more information, and this information is discarded. The question of whether this information can be used is a very interesting question, one that is an active topic of our research. In the example of laminates, Section 5.3, we find that the six (eight with strain hardening) dimensional micromechanical (field) variables can be encoded using only three (respectively four) internal variables. This is very much in the spirit of reduced order modeling. Further, these encoding variables can be used as internal variables. So it is possible that adding the micromechanical fields can lead to identifying internal variables with less data (fewer trajectories). The converse, reconstructing the micromechanical field from the macroscopically learned internal variable, is subtler. Since the macroscale response is averaged, many different micromechanical fields may give rise to the same incremental macroscale response. In other words, the map from the micromechanical field to incremental macroscopic response is unique, but the converse may not be. The analogous question over a trajectory over long periods of time is not clear since the flow may collapse the micromechanical fields. All of this is a topic of current research.

Lastly, an interesting topic concerns thermodynamic and symmetry restrictions. In this work, we have not required any thermodynamic or material symmetry restrictions on the functions f, g_i in (5.2). Instead, we expect the models to learn such restrictions from the data. It is possible to build architectures with such conditions (e.g., [119] for dissipative processes and [16] for hyperelasticity). We do not do so for two reasons. Thermodynamic and symmetry conditions often restrict the constitutive relations to certain (nonlinear) manifolds, breaking the linear space structure useful for neural networks. Further, we believe the ability to learn such non-trivial conditions from data is a very useful check on the ability of these otherwise black-box over-parametrized models to approximate the data. So there is an intriguing balance between building in all known physics on the one hand and maintaining a relevant mathematical structure to learn physics from the data. This is a topic of current research.

Finally, our studies could be enhanced by two further explorations. First, for the polycrystal example, the single-crystal model we use to generate our data uses an isotropic "compressible neo-Hookean" elastic model. This choice in the model means the polycrystal is elastically homogeneous, removing possible microstructure coupling between elasticity and plasticity. Second, our approach does not address the starting microstructure, and we have to train an RNO for each initial microstructure. However, the internal variables incorporate some information about the microstructure during its evolution. Therefore, it may be possible to incorporate starting microstructure into this RNO framework. Both of these remain topics for the future.

Chapter 6

CONCLUSIONS AND FUTURE WORKS

6.1 Summary of findings

The complex material behavior observed due to inelastic deformations makes materials fascinating to study. Their dependence on defects, microstructure, history, loading conditions, etc., provides a breadth of avenues for engineering materials research and improvements. This thesis presents two computational approaches developed as tools to study these aspects in crystalline materials at the mesoscale.

Chapter 3 and 4 explored a phase-field approach to study deformation twinning, coupled with dislocation slip described through crystal plasticity, at the several grain scale. Specifically, in Chapter 3, we started by providing a detailed outline of the phase-field model to capture twinning's length-scale, coupled with classical crystal plasticity for dislocation slip and anisotropic elasticity. By focusing on simpler two-dimensional single-crystal samples with a single twin/slip system, we explored contributions from the phase-field surface energy to a twin thickness, separate twin nucleation and propagation thresholds, and twin-slip coupling. Next, through novel GPU accelerated computations, we explored two-dimensional polycrystal samples, which successfully captured complex twin bands and associated stress drops, often observed experimentally but lacking in previous "pseudo-slip" work. Further studies illustrated the model's complex history dependence and asymmetry in response, in the absence of cross-hardening, indicating the twin/slip systems interact solely through the kinematics. Chapter 4 built off the previous phase field study and focused on its application to describing low-symmetry metals such as magnesium. Appropriate extensions were made to account for three-dimensional materials with multiple twin and slip systems. Detailed twin transmission studies were conducted on a bicrystal sample, which showed twin promotion/arrest at grain boundaries and slip hot spots near twin boundaries. Finally, polycrystal simulations captured complex twin bands, texture influences, and non-local slip-twin interactions at grain boundaries.

The final study, in Chapter 5, explored developing an efficient surrogate model for predicting the average stress response of history dependent microscale problems. A deep neural network approach, recurrent neural operator (RNO), was developed

(with motivation from established internal variable theories in continuum models) in continuous time to map the history of the deformation gradient to the stress. The RNO was first applied to a laminate composite of elasto-viscoplastic materials, providing an accurate fitting with fewer state variables predicted than expected from theory. However, this simple model provides access to the low-dimension unit cell internal variables. Applying an auto-encoder on the model variables and more closely inspecting the governing equations allow us to confirm why the RNO model was able to use fewer variables. Secondly, the RNO model was applied to a more complex two-dimensional polycrystal elasto-viscoplastic material with two slip systems and varying plastic strain/rate hardening parameters. For all cases, we capture the need for two state variables to predict the deviatoric stress and none for the hydrostatic pressure since the history-dependent plasticity is solely in the deviatoric component of stress. Finally, additional studies were applied to three-dimensional magnesium specimens [113], where it provided an accurate surrogate, demonstrated resolution independence, and efficiency in multiscale simulations.

6.2 Future directions

This thesis presents physics-based and data-driven computational approaches to capture the inelastic deformation of materials; however, there are still several areas where continued development is possible.

The final phase field model developed and explored in Chapters 3 and 4 was applied in the context of twelve relevant slip systems, but only two of the six tensile twins. Although this simplification allowed us to keep the number of phase field variables manageable for this first study, several extensions can be made to include more inelastic mechanisms. First, including all tensile twins will allow for more quantitative investigation of the micro-structural details and experimental comparison, such as of polycrystal magnesium specimens conducted by Kelley and Hosford [93]. Second, although our simulations did not include compression twins due to their high nucleation threshold, studies by Li *et al.* [110] have found that the activation of compression twins is essential for certain loading situations. Thus, a simple model extension to include compression twins, would allow explorations of the competition between twins and pyramidal slip in c-axis compression. Both cases will also benefit from valid experimental data and atomistic simulations on the hardening behavior of these inelastic systems to fit cross-hardening energies, dissipation potentials, and phase field surface energies. For example, in Section 4.3, we discussed the matching of phase field parameters with first principle or density functional

theory simulations of twin surface energy calculations; however, this will be highly dependent on twin systems considered, material/alloying compositions, and other microstructure details, requiring calculations of energies for different applications. The inclusion of all relevant inelastic systems will allow for detailed microstructure studies of magnesium (and other hcp materials) where the competition or cooperation of twin and slip can be systematically explored in its connection to texture and loading conditions.

Another consideration for the phase-field modeling study is to account for dynamic loading and rate effects in these inelastic systems since twinning has been shown to have increased presence under high strain rate situations. The extent of rate dependency in the above studies is modeled through the dissipation potentials for twinning and dislocation slip. However, elastic rate dependence, inertia effects, and wave propagation are necessary to adequately capture dynamic material behavior. Lastly, the twin-slip interactions were based on our kinematic assumptions (i.e., order of the deformation gradients — plastic slip following twining), but the reverse order could be incorporated through slip transmutations. For this, detailed surveys of experimental and atomistic simulations on the transmutation/absorption of existing dislocations across a twin interface would be necessary [45, 58, 128] due to the high dependence on specific slip/twin systems and material considered. These additional considerations can develop accurate and versatile simulations to capture microscale details of magnesium, or other crystalline solids with deformation twinning and dislocation slip as their main inelastic mechanisms. By exploring these materials under complex loading conditions, we can motivate the design of material texture, composition, cold hardening, or other hardening mechanisms for increased strength, ductility, or impact resistance.

For the machine learning approach for surrogate models in Chapter 5, the accuracy and learned state variables were explored for the laminate composite and polycrystal cases with elasto-viscoplastic materials. Through the laminate composite studies we were able to directly connect the RNO learned internal variables to the model variables, leaving the future question on achieving the same for the polycrystal material. For the polycrystal case we have a significantly larger number of internal variables causing concerns on the uniqueness of the mapping between model and learned internal variables; nonetheless, obtaining a physical interpretation of the internal variable is of interest and could be explored following the laminate case. A second question of interest for the polycrystal case is why only two learned RNO internal

variables are necessary; and if any model assumptions cause these reduced variables. For example, in the studies, we considered only anisotropic behavior through plasticity. However, at the single crystal level, metals have anisotropic elasticity that could add additional texture information within the state variables. A second example would be to ensure the deformation gradient paths are a sufficient sampling of the input space and explore how varying the strain rates (or other sampling constants) may change results. Finally, the approach studied does not account for the starting microstructure of the polycrystalline samples. This would require training a separate RNO for each starting texture, which, although this training would be offline in the context of multiscale modeling, would add computations if exploring cases with several different local textures. Hence, a study of interest would be to incorporate starting microstructure into the RNO in the form of initialization of the RNO. The studies have shown that the learned internal variables hold information on the microstructure evolution, so it is reasonable that we can feed in the starting texture as an additional input.

Further natural extensions of the surrogate modeling studies would be to utilize the methodology and insights gained from the simpler laminate composite and polycrystal cases to explore other physics. The breadth of internal variable formulations for continuum problems provides several applications of the RNO structure to other physical phenomena beyond the elasto-viscoplastic case, such as deformation twinning, damage/fracture [29, 30, 32, 62, 122], liquid crystal elastomers [26, 52, 55, 120], etc. For the first case, deformation twinning, the phase field model for deformation twinning discussed in the previous studies, Chapter 3 and 4, along with its GPU accelerated computations can be utilized to efficiently generate data for the RNO framework. Utilizing the RNO fitting we will gain both an accurate stress prediction and learned internal variables. The high degree of anisotropy introduced by twinning and its length scale should require more state variables, which we could analyze and connect to inelastic variables or texture. The stress prediction can then be utilized within a multiscale framework to accurately predict the response and failure of materials with both twin and slip modes of inelastic deformation. The coupling of the phase-field twinning model with the RNO framework would be invaluable for describing the response of materials, such as Magnesium, at the application scale. By exploring these materials, at the macroscale, we can understand the effect of starting texture, material geometry, or hardening mechanisms for increased strength, ductility, or impact resistance for various dynamic applications.

All these enhancements will further contribute to the understanding and designing of failure-resilient engineering materials for complex loading.

BIBLIOGRAPHY

[1] M. A. Kumar and S. Mahesh. "Banding in single crystals during plastic deformation". In: *International Journal of Plasticity* 36 (2012), pp. 15–33. ISSN: 0749-6419. DOI: https://doi.org/10.1016/j.ijplas.2012.03.008. URL: https://www.sciencedirect.com/science/article/pii/S0749641912000484.

[2] H. Abdolvand and M. R. Daymond. "Multi-scale modeling and experimental study of twin inception and propagation in hexagonal close-packed materials using a crystal plasticity finite element approach; Part I: Average behavior. Part II: local behavior". In: *Journal of the Mechanics and Physics of Solids* 61 (2013), 783-802 and 803–818.

[3] S. R. Agnew, D. W. Brown, and C. N. Tomé. "Validating a polycrystal model for the elastoplastic response of magnesium alloy AZ31 using in situ neutron diffraction". In: *Acta Materialia* 54.18 (2006), pp. 4841–4852. ISSN: 1359-6454. DOI: https://doi.org/10.1016/j.actamat.2006.06.020. URL: https://www.sciencedirect.com/science/article/pii/S1359645406004502.

[4] S. R. Agnew, D. W. Brown, S. C. Vogel, and T. Holden. "In-Situ measurement of internal strain evolution during deformation dominated by mechanical twinning". In: *Residual Stresses VI, ECRS6*. Vol. 404. Materials Science Forum. Trans Tech Publications Ltd, Aug. 2002, pp. 747–754. DOI: 10.4028/www.scientific.net/MSF.404-407.747.

[5] S. R. Agnew and O. Duygulu. "Plastic anisotropy and the role of non-basal slip in magnesium alloy AZ31B". In: *International Journal of Plasticity* 21.6 (2005). Plasticity of Multiphase Materials, pp. 1161–1193. ISSN: 0749-6419. DOI: https://doi.org/10.1016/j.ijplas.2004.05.018. URL: https://www.sciencedirect.com/science/article/pii/S0749641904001408.

[6] S. R. Agnew, C. N. Tomé, D. W. Brown, T. M. Holden, and S. C. Vogel. "Study of slip mechanisms in a magnesium alloy by neutron diffraction and modeling". In: *Scripta Materialia* 48.8 (2003). ViewPoint Set No. 29 "Phase Transformations and Deformations in Magnesium Alloys", pp. 1003–1008. ISSN: 1359-6462. DOI: https://doi.org/10.1016/S1359-6462(02)00591-2. URL: https://www.sciencedirect.com/science/article/pii/S1359646202005912.

[7] S. R. Agnew, M. H. Yoo, and C. N. Tomé. "Application of texture simulation to understanding mechanical behavior of Mg and solid solution alloys containing Li or Y". In: *Acta Materialia* 49 (2001), pp. 4277–4289. ISSN: 13596454. DOI: 10.1016/S1359-6454(01)00297-X.

[8] A. Akhtar and A. Teghtsoonian. “Plastic deformation of zirconium single crystals”. In: *Acta Metallurgica* 19.7 (1971), pp. 655–663. ISSN: 0001-6160. DOI: https://doi.org/10.1016/0001-6160(71)90019-8. URL: https://www.sciencedirect.com/science/article/pii/0001616071900198.

[9] S. M. Allen and J. W. Cahn. “A microscopic theory for antiphase boundary motion and its application to antiphase domain coarsening”. In: *Acta Metallurgica* 27 (1979), pp. 1085–1095. ISSN: 00016160. DOI: 10.1016/0001-6160(79)90196-2.

[10] M. T. Andani et al. “A quantitative study of stress fields ahead of a slip band blocked by a grain boundary in unalloyed magnesium”. In: *Scientific Reports* 10.1 (2020). DOI: 10.1038/s41598-020-59684-y.

[11] M. Ardeljan and M. Knezevic. “Explicit modeling of double twinning in AZ31 using crystal plasticity finite elements for predicting the mechanical fields for twin variant selection and fracture analyses”. In: *Acta Materialia* 157 (2018), pp. 339–354. ISSN: 13596454. DOI: 10.1016/j.actamat.2018.07.045. URL: https://doi.org/10.1016/j.actamat.2018.07.045.

[12] M. Ardeljan, R. J. McCabe, I. J. Beyerlein, and M. Knezevic. “Explicit incorporation of deformation twins into crystal plasticity finite element models”. In: *Computer Methods in Applied Mechanics and Engineering* 295 (2015), pp. 396–413. ISSN: 00457825. DOI: 10.1016/j.cma.2015.07.003. URL: http://dx.doi.org/10.1016/j.cma.2015.07.003.

[13] A. Argon. *Strengthening mechanisms in crystal plasticity*. Oxford University Press, 2007.

[14] A. Artemev, Y. Jin, and A. Khachaturyan. “Three-dimensional phase field model of proper martensitic transformation”. In: *Acta Materialia* 49 (2001), pp. 1165–1177.

[15] M. Arul Kumar et al. “Role of microstructure on twin nucleation and growth in HCP titanium: A statistical study”. In: *Acta Materialia* 148 (2018), pp. 123–132. ISSN: 1359-6454. DOI: https://doi.org/10.1016/j.actamat.2018.01.041. URL: https://www.sciencedirect.com/science/article/pii/S1359645418300727.

[16] F. As’Ad, P. Avery, and C. Farhat. “A mechanics informed artificial neural network approach in data?driven constitutive modeling”. In: *International Journal for Numerical Methods in Engineering* 123 (2022), pp. 2738–2759.

[17] M. R. Barnett, M. D. Nave, and A. Ghaderi. “Yield point elongation due to twinning in a magnesium alloy”. In: *Acta Materialia* 60.4 (2012), pp. 1433–1443. ISSN: 1359-6454. DOI: https://doi.org/10.1016/j.actamat.2011.11.022. URL: https://www.sciencedirect.com/science/article/pii/S1359645411008123.

[18] B. Bay, N. Hansen, D.A. Hughes, and D. Kuhlmann-Wilsdorf. "Overview no. 96 evolution of f.c.c. deformation structures in polyslip". In: *Acta Metallurgica et Materialia* 40.2 (1992), pp. 205–219. ISSN: 0956-7151. DOI: https://doi.org/10.1016/0956-7151(92)90296-Q. URL: https://www.sciencedirect.com/science/article/pii/095671519290296Q.

[19] A. Bensoussan, J.-L. Lions, and G. Papanicolaou. *Asymptotic analysis for periodic structures*. Vol. 374. American Mathematical Soc., 2011.

[20] I. J. Beyerlein, L. Capolungo, P. E. Marshall, R. J. McCabe, and C. N. Tomé. "Statistical analyses of deformation twinning in magnesium". In: *Philosophical Magazine* 90 (2010), pp. 2161–2190.

[21] I. J. Beyerlein and A. Hunter. "Understanding dislocation mechanics at the mesoscale using phase field dislocation dynamics". In: *Philosophical Transactions of the Royal Society A: Mathematical, Physical and Engineering Sciences* 374 (2016), p. 20150166. ISSN: 1364503X. DOI: 10.1098/rsta.2015.0166.

[22] I. J. Beyerlein, R. J. McCabe, and C. N. Tomé. "Effect of microstructure on the nucleation of deformation twins in polycrystalline high-purity magnesium: A multi-scale modeling study". In: *Journal of the Mechanics and Physics of Solids* 59 (2011), pp. 988–1003. ISSN: 00225096. DOI: 10.1016/j.jmps.2011.02.007.

[23] I. J. Beyerlein and C. N. Tomé. "A probabilistic twin nucleation model for HCP polycrystalline metals". In: *Proceedings of the Royal Society A: Mathematical, Physical and Engineering Sciences* 466.2121 (2010), pp. 2517–2544. DOI: 10.1098/rspa.2009.0661.

[24] I. J. Beyerlein, J. Wang, M. R. Barnett, and C. N. Tomé. "Double twinning mechanisms in magnesium alloys via dissociation of lattice dislocations". In: *Proceedings of the Royal Society A: Mathematical, Physical and Engineering Sciences* 468.2141 (2012), pp. 1496–1520. DOI: 10.1098/rspa.2011.0731.

[25] T. R. Bieler, L. Wang, A. J. Beaudoin, P. Kenesei, and U. Lienert. "In situ characterization of twin nucleation in pure TI using 3D-XRD". In: *Metallurgical and Materials Transactions A* 45.1 (2013), pp. 109–122. DOI: 10.1007/s11661-013-2082-3.

[26] J. S. Biggins, M. Warner, and K. Bhattacharya. "Supersoft elasticity in polydomain nematic elastomers". In: *Physical Review Letters* 103.3 (2009). DOI: 10.1103/physrevlett.103.037802.

[27] J. F. Bingert, T. A. Mason, G. C. Kaschner, P. J. Maudlin, and G. T. Gray. "Deformation twinning in polycrystalline Zr: Insights from electron backscattered diffraction characterization". In: *Metallurgical and Materials Transactions A* 33.3 (2002). Sp. Iss. SI, pp. 955–963.

[28] C. Bonatti and D. Mohr. “On the importance of self-consistency in recurrent neural network models representing elasto-plastic solids”. In: *Journal of the Mechanics and Physics of Solids* 158 (2022), p. 104697.

[29] B. Bourdin, G. A. Francfort, and J.-J. Marigo. “Numerical experiments in revisited brittle fracture”. In: *Journal of the Mechanics and Physics of Solids* 48.4 (2000), pp. 797–826. ISSN: 0022-5096. DOI: https://doi.org/10.1016/S0022-5096(99)00028-9. URL: https://www.sciencedirect.com/science/article/pii/S0022509699000289.

[30] B. Bourdin, G. A. Francfort, and J.-J. Marigo. “The variational approach to fracture”. In: *Journal of Elasticity* 91.1-3 (2008), pp. 5–148. DOI: 10.1007/s10659-007-9107-3.

[31] K. J. Bowman. *Mechanical behavior of materials*. Wiley, 2009.

[32] S. Brach, E. Tanné, B. Bourdin, and K. Bhattacharya. “Phase-field study of crack nucleation and propagation in elastic–perfectly plastic bodies”. In: *Computer Methods in Applied Mechanics and Engineering* 353 (2019), pp. 44–65. ISSN: 0045-7825. DOI: https://doi.org/10.1016/j.cma.2019.04.027. URL: https://www.sciencedirect.com/science/article/pii/S0045782519302300.

[33] R. Brenner and P. Suquet. “Overall response of viscoelastic composites and polycrystals: exact asymptotic relations and approximate estimates”. In: *International Journal of Solids and Structures* 50.10 (2013), pp. 1824–1838.

[34] D. W. Brown et al. “Internal strain and texture evolution during deformation twinning in magnesium”. In: *Materials Science and Engineering: A* 399.1 (2005). Measurement and Interpretation of Internal/Residual Stresses, pp. 1–12. ISSN: 0921-5093. DOI: https://doi.org/10.1016/j.msea.2005.02.016. URL: https://www.sciencedirect.com/science/article/pii/S0921509305001541.

[35] H. G. V. Bueren. *Imperfections in crystals*. North-Holland, 1961.

[36] E. C. Burke and W. R. Hibbard. “Plastic deformation of magnesium single crystals”. In: *Journal of Mechanics* 4.3 (1952), pp. 295–303. DOI: 10.1007/bf03397694.

[37] J. W. Cahn and J. E. Hilliard. “Free energy of a nonuniform system. I. interfacial free energy”. In: *The Journal of Chemical Physics* 28.2 (Aug. 1958), pp. 258–267. ISSN: 0021-9606. DOI: 10.1063/1.1744102. eprint: https://pubs.aip.org/aip/jcp/article-pdf/28/2/258/11106115/258_1_online.pdf. URL: https://doi.org/10.1063/1.1744102.

[38] A. J. Cao and Y. G. Wei. “Formation of fivefold deformation twins in nanocrystalline face-centered-cubic copper based on molecular dynamics simulations”. In: *Applied Physics Letters* 89 (2006), pp. 2004–2007. ISSN: 00036951. DOI: 10.1063/1.2243958.

[39] L. Capolungo and I. J. Beyerlein. "Nucleation and stability of twins in hcp metals". In: *Physics Review B* 78 (2 July 2008), p. 024117. DOI: 10.1103/PhysRevB.78.024117. URL: https://link.aps.org/doi/10.1103/PhysRevB.78.024117.

[40] L. Capolungo, P. E. Marshall, R. J. McCabe, I. J. Beyerlein, and C. N. Tomé. "Nucleation and growth of twins in Zr: A statistical study". In: *Acta Materialia* 57.20 (2009), pp. 6047–6056.

[41] C. Carstensen, K. Hackl, and A. Mielke. "Non-convex potentials and microstructures in finite-strain plasticity". In: *Proceedings of the Royal Society A: Mathematical, Physical and Engineering Sciences* 458 (2002), pp. 299–317. ISSN: 13645021. DOI: 10.1098/rspa.2001.0864.

[42] Y. Chang and D. M. Kochmann. "A variational constitutive model for slip-twinning interactions in hcp metals: Application to single- and polycrystalline magnesium". In: *International Journal of Plasticity* 73 (2015), pp. 39–61. ISSN: 07496419. DOI: 10.1016/j.ijplas.2015.03.008. URL: http://dx.doi.org/10.1016/j.ijplas.2015.03.008.

[43] Y. Chang, J. T. Lloyd, R. Becker, and D. M. Kochmann. "Modeling microstructure evolution in magnesium: Comparison of detailed and reduced-order kinematic models". In: *Mechanics of Materials* 108 (2017), pp. 40–57. ISSN: 01676636. DOI: 10.1016/j.mechmat.2017.02.007. URL: http://dx.doi.org/10.1016/j.mechmat.2017.02.007.

[44] A. Chapuis and J. H. Driver. "Temperature dependency of slip and twinning in plane strain compressed magnesium single crystals". In: *Acta Materialia* 59.5 (2011), pp. 1986–1994. ISSN: 1359-6454. DOI: https://doi.org/10.1016/j.actamat.2010.11.064. URL: https://www.sciencedirect.com/science/article/pii/S1359645410008190.

[45] P. Chen, F. Wang, and B. Li. "Dislocation absorption and transmutation at $\{10\bar{1}2\}$ twin boundaries in deformation of magnesium". In: *Acta Materialia* 164 (2019), pp. 440–453. DOI: 10.1016/j.actamat.2018.10.064.

[46] X. Chen, Y. Geng, and F. Pan. "Research progress in magnesium alloys as functional materials". In: *Rare Metal Materials and Engineering* 45 (2016), pp. 2269–2274. ISSN: 1002185X. DOI: 10.1016/s1875-5372(17)30015-2. URL: http://dx.doi.org/10.1016/S1875-5372(17)30015-2.

[47] J. Cheng and S. Ghosh. "Crystal plasticity finite element modeling of discrete twin evolution in polycrystalline magnesium". In: *Journal of the Mechanics and Physics of Solids* 99.July 2016 (2017), pp. 512–538. ISSN: 00225096. DOI: 10.1016/j.jmps.2016.12.008. URL: http://dx.doi.org/10.1016/j.jmps.2016.12.008.

[48] J. Cheng, J. Shen, R. K. Mishra, and S. Ghosh. "Discrete twin evolution in Mg alloys using a novel crystal plasticity finite element model". In: *Acta Materialia* 149 (2018), pp. 142–153. ISSN: 13596454. DOI: 10.1016/

j.actamat.2018.02.032. URL: https://doi.org/10.1016/j.actamat.2018.02.032.

[49] J. W. Christian and S. Mahajan. "Deformation twinning". In: *Progress in Materials Science* 39 (1995), pp. 1–157.

[50] J. D. Clayton and J. Knap. "A phase field model of deformation twinning: Nonlinear theory and numerical simulations". In: *Physica D: Nonlinear Phenomena* 240 (2011), pp. 841–858. ISSN: 01672789. DOI: 10.1016/j.physd.2010.12.012. URL: http://dx.doi.org/10.1016/j.physd.2010.12.012.

[51] J.B. Cohen and J. Weertman. "A dislocation model for twinning in f.c.c. metals". In: *Acta Metallurgica* 11.8 (1963), pp. 996–998. ISSN: 0001-6160. DOI: https://doi.org/10.1016/0001-6160(63)90074-9. URL: https://www.sciencedirect.com/science/article/pii/0001616063900749.

[52] S. Conti, A. DeSimone, and G. Dolzmann. "Soft elastic response of stretched sheets of nematic elastomers: a numerical study". In: *Journal of the Mechanics and Physics of Solids* 50.7 (2002), pp. 1431–1451. ISSN: 0022-5096. DOI: https://doi.org/10.1016/S0022-5096(01)00120-X. URL: https://www.sciencedirect.com/science/article/pii/S002250960100120X.

[53] S. Conti and M. Ortiz. "Minimum principles for the trajectories of systems governed by rate problems". In: *Journal of the Mechanics and Physics of Solids* 56 (2008), pp. 1885–1904. ISSN: 00225096. DOI: 10.1016/j.jmps.2007.11.006.

[54] A. M. Cuitino and M. Ortiz. "Computational modelling of single crystals". In: *Modelling and Simulation in Materials Science and Engineering* 1.3 (1993), pp. 225–263. DOI: 10.1088/0965-0393/1/3/001.

[55] A. DeSimone and G. Dolzmann. "Macroscopic response of nematic elastomers via relaxation of a class of so(3)-invariant energies". In: *Archive for Rational Mechanics and Analysis* 161.3 (2002), pp. 181–204. DOI: 10.1007/s002050100174.

[56] G. E. Dieter. *Mechanical metallurgy*. McGraw-Hill, 1976.

[57] S. Du, J. Lee, H. Li, L. Wang, and X. Zhai. "Gradient descent finds global minima of deep neural networks". In: *International conference on machine learning*. PMLR. 2019, pp. 1675–1685.

[58] H. El Kadiri and A.L. Oppedal. "A crystal plasticity theory for latent hardening by glide twinning through dislocation transmutation and twin accommodation effects". In: *Journal of the Mechanics and Physics of Solids* 58.4 (2010), pp. 613–624. ISSN: 0022-5096. DOI: https://doi.org/10.1016/j.jmps.2009.12.004. URL: https://www.sciencedirect.com/science/article/pii/S0022509609001793.

[59] H. El Kadiri et al. “Flow asymmetry and nucleation stresses of $\{10\bar{1}2\}$ twinning and non-basal slip in magnesium”. In: *International Journal of Plasticity* 44 (2013), pp. 111–120. ISSN: 0749-6419. DOI: https://doi.org/10.1016/j.ijplas.2012.11.004. URL: https://www.sciencedirect.com/science/article/pii/S0749641912001696.

[60] B. Feng et al. “Coupled elasticity, plastic slip, and twinning in single crystal titanium loaded by split-Hopkinson pressure bar”. In: *Journal of the Mechanics and Physics of Solids* 119 (2018), pp. 274–297. ISSN: 00225096. DOI: 10.1016/j.jmps.2018.06.018. URL: https://doi.org/10.1016/j.jmps.2018.06.018.

[61] B. Feng et al. “Three-dimensional modeling and simulations of single-crystal and bi-crystal titanium for high-strain-rate loading conditions”. In: *International Journal of Plasticity* 133 (2020). ISSN: 07496419. DOI: 10.1016/j.ijplas.2020.102771.

[62] G. A. Francfort and J.-J. Marigo. “Revisiting brittle fracture as an energy minimization problem”. In: *Journal of the Mechanics and Physics of Solids* 46.8 (1998), pp. 1319–1342. ISSN: 0022-5096. DOI: https://doi.org/10.1016/S0022-5096(98)00034-9. URL: https://www.sciencedirect.com/science/article/pii/S0022509698000349.

[63] G. A. Francfort and P. M. Suquet. “Homogenization and mechanical dissipation in thermoviscoelasticity”. In: *Archive for Rational Mechanics and Analysis* 96.3 (1986), pp. 265–293.

[64] F. Fritzen, T. Böhlke, and E. Schnack. “Periodic three-dimensional mesh generation for crystalline aggregates based on Voronoi tessellations”. In: *Computational Mechanics* 43 (2009), pp. 701–713.

[65] F. Ghavamian and A. Simone. “Accelerating multiscale finite element simulations of history-dependent materials using a recurrent neural network”. In: *Computer Methods in Applied Mechanics and Engineering* 357 (2019), p. 112594.

[66] E. Van Der Giessen et al. “Roadmap on multiscale materials modeling”. In: *Modelling and Simulation in Materials Science and Engineering* 28.4 (2020), p. 043001.

[67] S. Godet, L. Jiang, A. A. Luo, and J. J. Jonas. “Use of Schmid factors to select extension twin variants in extruded magnesium alloy tubes”. In: *Scripta materialia* 55.11 (2006), pp. 1055–1058.

[68] S. Graff, W. Brocks, and D. Steglich. “Yielding of magnesium: From single crystal to polycrystalline aggregates”. In: *International Journal of Plasticity* 23 (2007), pp. 1957–1978. ISSN: 07496419. DOI: 10.1016/j.ijplas.2007.07.009.

[69] G. T. Gray. “Influence of strain rate and temperature on the structure. property behavior of high-purity titanium”. In: *Le Journal de Physique IV* 07.C3 (1997). DOI: 10.1051/jp4:1997373.

[70] C. Guo, R. Xin, C. Ding, B. Song, and Q. Liu. “Understanding of variant selection and twin patterns in compressed Mg alloy sheets via combined analysis of Schmid factor and strain compatibility factor”. In: *Materials Science and Engineering: A* 609 (2014), pp. 92–101.

[71] N. P. Gurao, R. Kapoor, and S. Suwas. “Deformation behaviour of commercially pure titanium at extreme strain rates”. In: *Acta Materialia* 59.9 (2011), pp. 3431–3446. ISSN: 1359-6454. DOI: https://doi.org/10.1016/j.actamat.2011.02.018. URL: https://www.sciencedirect.com/science/article/pii/S1359645411001121.

[72] M. E. Gurtin, E. Fried, and L. Anand. *The Mechanics and Thermodynamics of Continua*. Cambridge: Cambridge University Press, 2010.

[73] M. Gzyl et al. “Mechanical properties and microstructure of AZ31B Magnesium alloy processed by I-ECAP”. In: *Metallurgical and Materials Transactions A* 45 (Mar. 2014). DOI: 10.1007/s11661-013-2094-z.

[74] E. O. Hall. “The deformation and ageing of mild steel: III discussion of results”. In: *Proceedings of the Physical Society. Section B* 64.9 (1951), pp. 747–753. DOI: 10.1088/0370-1301/64/9/303.

[75] N. Hansen. “The effect of grain size and strain on the tensile flow stress of aluminium at room temperature”. In: *Acta Metallurgica* 25.8 (1977), pp. 863–869. ISSN: 0001-6160. DOI: https://doi.org/10.1016/0001-6160(77)90171-7. URL: https://www.sciencedirect.com/science/article/pii/0001616077901717.

[76] R. Hill and J. R. Rice. “Constitutive analysis of elastic-plastic crystals at arbitrary strain”. In: *Journal of the Mechanics and Physics of Solids* 20.6 (1972), pp. 401–413. ISSN: 0022-5096. DOI: https://doi.org/10.1016/0022-5096(72)90017-8. URL: https://www.sciencedirect.com/science/article/pii/0022509672900178.

[77] S.-G. Hong, S. H. Park, and C. S. Lee. “Role of $\{10\bar{1}2\}$ twinning characteristics in the deformation behavior of a polycrystalline magnesium alloy”. In: *Acta Materialia* 58.18 (2010), pp. 5873–5885. ISSN: 1359-6454. DOI: https://doi.org/10.1016/j.actamat.2010.07.002. URL: https://www.sciencedirect.com/science/article/pii/S135964541000426X.

[78] S. Hu, C. H. Henager, and L. Chen. “Simulations of stress-induced twinning and de-twinning: A phase field model”. In: *Acta Materialia* 58.19 (2010), pp. 6554–6564. ISSN: 1359-6454. DOI: https://doi.org/10.1016/j.actamat.2010.08.020. URL: https://www.sciencedirect.com/science/article/pii/S1359645410005343.

[79] X. Hu, Y. Ji, W. Heo T, L.-Q. Chen, and X. Cui. "Phase-field model of deformation twin-grain boundary interactions in hexagonal systems". In: *Acta Materialia* 200 (2020), pp. 821–834. ISSN: 1359-6454. DOI: https://doi.org/10.1016/j.actamat.2020.09.062. URL: https://www.sciencedirect.com/science/article/pii/S1359645420307564.

[80] X. Hu et al. "Spectral phase-field model of deformation twinning and plastic deformation". In: *International Journal of Plasticity* 143 (2021), p. 103019. ISSN: 0749-6419. DOI: https://doi.org/10.1016/j.ijplas.2021.103019. URL: https://www.sciencedirect.com/science/article/pii/S0749641921000942.

[81] D. A. Hughes and N. Hansen. "High angle boundaries formed by grain subdivision mechanisms". In: *Acta Materialia* 45.9 (1997), pp. 3871–3886. ISSN: 1359-6454. DOI: https://doi.org/10.1016/S1359-6454(97)00027-X. URL: https://www.sciencedirect.com/science/article/pii/S135964549700027X.

[82] J. Humphreys, G. S. Rohrer, and A/ Rollett. "Chapter 2 - The Deformed State". In: *Recrystallization and Related Annealing Phenomena (Third Edition)*. Ed. by John Humphreys, Gregory S. Rohrer, and Anthony Rollett. Third Edition. Oxford: Elsevier, 2017, pp. 13–79. ISBN: 978-0-08-098235-9. DOI: https://doi.org/10.1016/B978-0-08-098235-9.00002-1. URL: https://www.sciencedirect.com/science/article/pii/B9780080982359000021.

[83] S. Im, J. Lee, and M. Cho. "Surrogate modeling of elasto-plastic problems via long short-term memory neural networks and proper orthogonal decomposition". In: *Computer Methods in Applied Mechanics and Engineering* 385 (2021), p. 114030.

[84] K. Jagannadham. "Lattice dislocation near a surface". In: *Journal of Applied Physics* 47.10 (Aug. 2008), pp. 4401–4403. ISSN: 0021-8979. DOI: 10.1063/1.322445. eprint: https://pubs.aip.org/aip/jap/article-pdf/47/10/4401/7957289/4401_1_online.pdf. URL: https://doi.org/10.1063/1.322445.

[85] R. D. James. "Finite deformation by mechanical twinning". In: *Archive for Rational Mechanics and Analysis* 77.2 (1981), pp. 143–176. DOI: 10.1007/bf00250621.

[86] L. Jiang et al. "Twin nucleation from a single <c+a> dislocation in hexagonal close-packed crystals". In: *Acta Materialia* 202 (2021), pp. 35–41. ISSN: 13596454. DOI: 10.1016/j.actamat.2020.10.038.

[87] T. Jin, H. M. Mourad, C. A. Bronkhorst, and I. J. Beyerlein. "A single crystal plasticity finite element formulation with embedded deformation twins". In: *Journal of the Mechanics and Physics of Solids* 133 (2019),

p. 103723. ISSN: 00225096. DOI: 10.1016/j.jmps.2019.103723. URL: https://doi.org/10.1016/j.jmps.2019.103723.

[88] J. J. Jonas et al. "The role of strain accommodation during the variant selection of primary twins in magnesium". In: *Acta Materialia* 59.5 (2011), pp. 2046–2056.

[89] W. J. Joost and P. E. Krajewski. "Towards magnesium alloys for high-volume automotive applications". In: *Scripta Materialia* 128 (2017), pp. 107–112. ISSN: 13596462. DOI: 10.1016/j.scriptamat.2016.07.035. URL: http://dx.doi.org/10.1016/j.scriptamat.2016.07.035.

[90] T. Kaiser and A. Menzel. "A dislocation density tensor-based crystal plasticity framework". In: *Journal of the Mechanics and Physics of Solids* 131 (2019), pp. 276–302. ISSN: 00225096. DOI: 10.1016/j.jmps.2019.05.019.

[91] S. R. Kalidindi. "Incorporation of Deformation Twinning in Models". In: *International Journal of Plasticity* 46 (1998), pp. 267–290.

[92] K. Kawaguchi. "Deep learning without poor local minima". In: *Advances in Neural Information Processing Systems* 29 (2016).

[93] E. W. Kelley and W. F. Hosford. "Plane-strain compression of Magnesium and Magnesium alloy crystals". In: *Transactions of the Metallurgical Society of AIME* (1969), p. 9.

[94] A. Kelly and K. M. Knowles. *Crystallography and Crystal Engineering*. Vol. 2. John Wiley and Sons, 2012, pp. 459–498. ISBN: 9783527329823. DOI: 10.1002/9783527644131.ch10.

[95] D. P. Kingma and J. Ba. "Adam: A method for stochastic optimization". In: *arXiv preprint arXiv:1412.6980* (2014).

[96] G. Klambauer, T. Unterthiner, A. Mayr, and S. Hochreiter. "Self-normalizing neural networks". In: *Advances in neural information processing systems* 30 (2017).

[97] R. Kondo, Y. Tadano, and K. Shizawa. "A phase-field model of twinning and detwinning coupled with dislocation-based crystal plasticity for HCP metals". In: *Computational Materials Science* 95 (2014), pp. 672–683. ISSN: 0927-0256. DOI: https://doi.org/10.1016/j.commatsci.2014.08.034. URL: https://www.sciencedirect.com/science/article/pii/S092702561400576X.

[98] M. L. Kronberg. "A structural mechanism for the twinning process on [1012] in hexagonal close packed metals". In: *Acta Metallurgica* 16 (1968), pp. 29–34. ISSN: 00016160. DOI: 10.1016/0001-6160(68)90068-0.

[99] E. Kröner and C. Teodosiu. "Lattice defect approach to plasticity and viscoplasticity". In: *Problems of Plasticity* (1974), pp. 45–88. DOI: 10.1007/978-94-010-2311-5_3.

[100] D. Kuhlmann-Wilsdorf. "OVERVIEW No. 131"Regular" deformation bands (DBs) and the LEDS hypothesis". In: *Acta Materialia* 47.6 (1999), pp. 1697–1712. ISSN: 1359-6454. DOI: https://doi.org/10.1016/S1359-6454(98)00413-3. URL: https://www.sciencedirect.com/science/article/pii/S1359645498004133.

[101] D. Kuhlmann-Wilsdorf and N. Hansen. "Geometrically necessary, incidental and subgrain boundaries". In: *Scripta Metallurgica et Materialia* 25.7 (1991), pp. 1557–1562. ISSN: 0956-716X. DOI: https://doi.org/10.1016/0956-716X(91)90451-6. URL: https://www.sciencedirect.com/science/article/pii/0956716X91904516.

[102] M. K. Kulekci. "Magnesium and its alloys applications in automotive industry". In: *International Journal of Advanced Manufacturing Technology* 39 (2008), pp. 851–865. ISSN: 02683768. DOI: 10.1007/s00170-007-1279-2.

[103] A. M. Kumar, I. J. Beyerlein, R. J. McCabe, and C. N. Tomé. "Grain neighbour effects on twin transmission in hexagonal close-packed materials". In: *Nature Communications* 7.1 (2016). DOI: 10.1038/ncomms13826.

[104] K. Kuśnierczyk and M. Basista. "Recent advances in research on magnesium alloys and magnesium-calcium phosphate composites as biodegradable implant materials". In: *Journal of Biomaterials Applications* 31 (2017), pp. 878–900. ISSN: 15308022. DOI: 10.1177/0885328216657271.

[105] Y. LeCun, Y. Bengio, and G. Hinton. "Deep learning". In: *Nature* 521.7553 (2015), pp. 436–444.

[106] E. H. Lee. "Elastic-plastic deformation at finite strains". In: *Journal of Applied Mechanics* 36.1 (1969), pp. 1–6. DOI: 10.1115/1.3564580.

[107] M. Lefik, D.P. Boso, and B.A. Schrefler. "Artificial Neural Networks in numerical modelling of composites". In: *Computer Methods in Applied Mechanics and Engineering* 198 (2009), pp. 1785–1804.

[108] M. Lentz, M. Risse, N. Schaefer, W. Reimers, and I. J. Beyerlein. "Strength and ductility with $\{10\bar{1}1\}$ — $\{10\bar{1}2\}$ double twinning in a Magnesium alloy". In: *Nature Communications* 7.1 (2016). DOI: 10.1038/ncomms11068.

[109] V. I. Levitas, V. A. Levin, K. M. Zingerman, and E. I. Freiman. "Displacive phase transitions at large strains: Phase-field theory and simulations". In: *Physical Review Letters* 103 (2009), pp. 1–4. ISSN: 00319007. DOI: 10.1103/PhysRevLett.103.025702.

[110] B. Li and E. Ma. "Atomic shuffling dominated mechanism for deformation twinning in magnesium". In: *Physical Review Letters* 103 (2009), pp. 1–4. ISSN: 00319007. DOI: 10.1103/PhysRevLett.103.035503.

[111] H. Li, Z. Xu, G. Taylor, C. Studer, and T. Goldstein. "Visualizing the loss landscape of neural nets". In: *Advances in Neural Information Processing Systems* 31 (2018).

[112] J. Lind et al. "Tensile twin nucleation events coupled to neighboring slip observed in three dimensions". In: *Acta Materialia* 76 (2014), pp. 213–220. ISSN: 1359-6454. DOI: 10.1016/j.actamat.2014.04.050.

[113] B. Liu, E. Ocegueda, M. Trautner, A. M. Stuart, and K. Bhattacharya. "Learning macroscopic internal variables and history dependence from microscopic models". In: *Journal of the Mechanics and Physics of Solids* (2023), p. 105329. ISSN: 0022-5096. DOI: https://doi.org/10.1016/j.jmps.2023.105329. URL: https://www.sciencedirect.com/science/article/pii/S0022509623001333.

[114] B. Liu et al. "A learning-based multiscale method and its application to inelastic impact problems". In: *Journal of the Mechanics and Physics of Solids* 158 (2022), p. 104668.

[115] C. Liu et al. "An integrated crystal plasticity-phase field model for spatially resolved twin nucleation, propagation, and growth in hexagonal materials". In: *International Journal of Plasticity* 106 (2018), pp. 203–227. ISSN: 07496419. DOI: 10.1016/j.ijplas.2018.03.009. URL: https://doi.org/10.1016/j.ijplas.2018.03.009.

[116] H. Liu et al. "Formation and autocatalytic nucleation of co-zone $\{10\bar{1}2\}$ deformation twins in polycrystalline Mg: A phase field simulation study". In: *Acta Materialia* 153 (2018), pp. 86–107. ISSN: 1359-6454. DOI: https://doi.org/10.1016/j.actamat.2018.04.043. URL: https://www.sciencedirect.com/science/article/pii/S1359645418303203.

[117] H. J. Logarzo, G. Capuano, and J. J. Rimoli. "Smart constitutive laws: Inelastic homogenization through machine learning". In: *Computer Methods in Applied Mechanics and Engineering* 373 (2021).

[118] S. Mahajan and G.Y. Chin. "Formation of deformation twins in f.c.c. crystals". In: *Acta Metallurgica* 21.10 (1973), pp. 1353–1363. ISSN: 0001-6160. DOI: https://doi.org/10.1016/0001-6160(73)90085-0. URL: https://www.sciencedirect.com/science/article/pii/0001616073900850.

[119] F. Masi, I. Stefanou, P. Vannucci, and V. Maffi-Berthier. "Thermodynamics-based Artificial Neural Networks for constitutive modeling". In: *Journal of the Mechanics and Physics of Solids* 147 (2021), p. 104277.

[120] B. L. Mbanga, F. Ye, J. V. Selinger, and R. L. Selinger. "Modeling elastic instabilities in nematic elastomers". In: *Physical Review E* 82.5 (2010). DOI: 10.1103/physreve.82.051701.

[121] S. Mendelson. “Dislocation dissociations and dislocation mobility in diamond lattice crystals”. In: *Journal of Applied Physics* 43.5 (Oct. 2008), pp. 2102–2113. ISSN: 0021-8979. DOI: 10.1063/1.1661460. eprint: https://pubs.aip.org/aip/jap/article-pdf/43/5/2102/10562006/2102_1_online.pdf. URL: https://doi.org/10.1063/1.1661460.

[122] C. Miehe, M. Hofacker, and F. Welschinger. “A phase field model for rate-independent crack propagation: Robust algorithmic implementation based on operator splits”. In: *Computer Methods in Applied Mechanics and Engineering* 199.45 (2010), pp. 2765–2778. ISSN: 0045-7825. DOI: https://doi.org/10.1016/j.cma.2010.04.011. URL: https://www.sciencedirect.com/science/article/pii/S0045782510001283.

[123] C. Miehe and J. Schröder. “A comparative study of stress update algorithms for rate-independent and rate-dependent crystal plasticity”. In: *International Journal for Numerical Methods in Engineering* 50.2 (2001), pp. 273–298. DOI: https://doi.org/10.1002/1097-0207(20010120)50:2<273::AID-NME17>3.0.CO;2-Q. eprint: https://onlinelibrary.wiley.com/doi/pdf/10.1002/1097-0207\%2820010120\%2950\%3A2\%3C273\%3A\%3AAID-NME17\%3E3.0.CO\%3B2-Q. URL: https://onlinelibrary.wiley.com/doi/abs/10.1002/1097-0207%5C%%202820010120%5C%2950%5C%3A2%5C%3C273%5C%3A%5C%3AAID-NME17%5C%3E3.0.CO%5C%3B2-Q.

[124] A. Miranville. “Generalized Cahn-Hilliard equations based on a microforce balance”. In: *Journal of Applied Mathematics* 2003 (2003), pp. 165–185. ISSN: 1110757X. DOI: 10.1155/S1110757X03204083.

[125] T. Morris, R. James, Y. Ye, and M. H. Yoo. “First-principles examination of the twin boundary in Hcp Metals”. In: *Philosophical Magazine* 85.2-3 (2005), pp. 233–238. DOI: 10.1080/14786430412331315671.

[126] M. Mozaffar et al. “Deep learning predicts path-dependent plasticity”. In: *Proceedings of the National Academy of Sciences* 116.52 (2019), pp. 26414–26420.

[127] J. F. Nye. “Some geometrical relations in dislocated crystals”. In: *Acta Metallurgica* 1 (1953), pp. 153–162. ISSN: 00016160. DOI: 10.1016/0001-6160(53)90054-6.

[128] A. L. Oppedal et al. “Effect of dislocation transmutation on modeling hardening mechanisms by twinning in magnesium”. In: *International Journal of Plasticity* 30-31 (2012), pp. 41–61. ISSN: 0749-6419. DOI: https://doi.org/10.1016/j.ijplas.2011.09.002. URL: https://www.sciencedirect.com/science/article/pii/S0749641911001495.

[129] A. Orozco-Caballero, D. Lunt, J. D. Robson, and J. Quinta da Fonseca. "How magnesium accommodates local deformation incompatibility: A high-resolution digital image correlation study". In: *Acta Materialia* 133 (2017), pp. 367–379. ISSN: 13596454. DOI: 10.1016/j.actamat.2017.05.040.

[130] M. Ortiz and L. Stainier. "The variational formulation of viscoplastic constitutive updates". In: *Computer Methods in Applied Mechanics and Engineering* 171 (1999), pp. 419–444. ISSN: 00457825. DOI: 10.1016/S0045-7825(98)00219-9.

[131] G. Pavliotis and A. M. Stuart. *Multiscale methods: averaging and homogenization*. Springer Science & Business Media, 2008.

[132] D. Peirce, R. J. Asaro, and A. Needleman. "An analysis of nonuniform and localized deformation in ductile single crystals". In: *Acta Metallurgica* 30.6 (1982), pp. 1087–1119. ISSN: 0001-6160. DOI: https://doi.org/10.1016/0001-6160(82)90005-0. URL: https://www.sciencedirect.com/science/article/pii/0001616082900050.

[133] N. J. Petch. "The cleavage strength of polycrystals". In: *The Journal of the Iron and Steel Institute* 173.5 (1953), pp. 25–28.

[134] R. Phillips. *Crystals, defects and microstructures: modeling across scales*. Cambridge University Press, 2001.

[135] R. Priestner and W. C. Leslie. "Nucleation of deformation twins at slip plane intersections in B.C.C. metals". In: *The Philosophical Magazine: A Journal of Theoretical Experimental and Applied Physics* 11.113 (1965), pp. 895–916. DOI: 10.1080/14786436508223953. eprint: https://doi.org/10.1080/14786436508223953. URL: https://doi.org/10.1080/14786436508223953.

[136] S. R. Kalidindi. "Modeling anisotropic strain hardening and deformation textures in low stacking fault energy fcc metals". In: *International Journal of Plasticity* 17.6 (2001), pp. 837–860. ISSN: 0749-6419. DOI: https://doi.org/10.1016/S0749-6419(00)00071-1. URL: https://www.sciencedirect.com/science/article/pii/S0749641900000711.

[137] W. T. Read. *Dislocations in crystals*. McGraw-Hill, 1953.

[138] R. E. Reed-Hill and W. D. Robertson. "Pyramidal slip in Magnesium". In: *Trans. Met. Soc. AIME* (Apr. 1958). URL: https://www.osti.gov/biblio/4317515.

[139] M. Rezaee-Hajidehi, P. Sadowski, and S. Stupkiewicz. "Deformation twinning as a displacive transformation: Finite-strain phase-field model of coupled twinning and crystal plasticity". In: *Journal of the Mechanics and Physics of Solids* 163 (2022), p. 104855. ISSN: 0022-5096. DOI: https://doi.org/10.1016/j.jmps.2022.104855. URL: https://www.sciencedirect.com/science/article/pii/S0022509622000680.

[140] J. R. Rice. "Inelastic constitutive relations for solids: An internal-variable theory and its application to metal plasticity". In: *Journal of the Mechanics and Physics of Solids* 19.6 (1971), pp. 433–455. ISSN: 0022-5096. DOI: https://doi.org/10.1016/0022-5096(71)90010-X. URL: https://www.sciencedirect.com/science/article/pii/002250967190010X.

[141] J. R. Rice. "Inelastic constitutive relations for solids: an internal-variable theory and its application to metal plasticity". In: *Journal of the Mechanics and Physics of Solids* 19.6 (1971), pp. 433–455.

[142] G. Rotskoff and E. Vanden-Eijnden. "Trainability and accuracy of artificial neural networks: An interacting particle system approach". In: *Communications on Pure and Applied Mathematics* 75.9 (2022), pp. 1889–1935.

[143] I. Safran and O. Shamir. "Spurious local minima are common in two-layer relu neural networks". In: *International conference on machine learning*. PMLR. 2018, pp. 4433–4441.

[144] J. Sanchez-Hubert and E. Sanchez-Palencia. "Sur certains problèmes physiques d'homogénéisation donnant lieu à des phénomènes de relaxation". In: *Comptes Rendus de l'Académie des Sciences - Series A* 286 (1978), pp. 903–906.

[145] S. Sandlöbes, S. Zaefferer, I. Schestakow, S. Yi, and R. Gonzalez-Martinez. "On the role of non-basal deformation mechanisms for the ductility of Mg and Mg–Y alloys". In: *Acta Materialia* 59.2 (2011), pp. 429–439. ISSN: 1359-6454. DOI: https://doi.org/10.1016/j.actamat.2010.08.031. URL: https://www.sciencedirect.com/science/article/pii/S1359645410005458.

[146] L. J. Slutsky and C. W. Garland. "Elastic Constants of Magnesium from 4.2°K to 300°K". In: *Physics Review* 107 (4 Aug. 1957), pp. 972–976. DOI: 10.1103/PhysRev.107.972. URL: https://link.aps.org/doi/10.1103/PhysRev.107.972.

[147] Y. Song, J. Yeon, and B. Na. "Numerical simulations of the hall–petch relationship in aluminium using gradient-enhanced plasticity model". In: *Advances in Civil Engineering* 2019 (2019), pp. 1–9. DOI: 10.1155/2019/7356581.

[148] A. Staroselsky and L. Anand. "A constitutive model for hcp materials deforming by slip and twinning: Application to magnesium alloy AZ31B". In: *International Journal of Plasticity* 19 (2003), pp. 1843–1864. ISSN: 07496419. DOI: 10.1016/S0749-6419(03)00039-1.

[149] J. Tang et al. "Interaction between a {1012} twin boundary and grain boundaries in magnesium". In: *International Journal of Plasticity* 126 (2020), p. 102613. ISSN: 07496419. DOI: 10.1016/j.ijplas.2019.10.001. URL: https://doi.org/10.1016/j.ijplas.2019.10.001.

[150] A. D. Tutcuoglu, A. Vidyasagar, K. Bhattacharya, and D. M. Kochmann. "Stochastic modeling of discontinuous dynamic recrystallization at finite strains in hcp metals". In: *Journal of the Mechanics and Physics of Solids* 122 (2019), pp. 590–612. ISSN: 00225096. DOI: 10.1016/j.jmps.2018.09.032.

[151] J. Wang, J. P. Hirth, and C. N. Tomé. "(-1 0 1 2) Twinning nucleation mechanisms in hexagonal-close-packed crystals". In: *Acta Materialia* 57 (2009), pp. 5521–5530. ISSN: 13596454. DOI: 10.1016/j.actamat.2009.07.047.

[152] L. Wang, R. Barabash, T. Bieler, W. Liu, and P. Eisenlohr. "Study of $\{11\bar{2}1\}$ twinning in α-TI by EBSD and Laue microdiffraction". In: *Metallurgical and Materials Transactions A* 44.8 (2013), pp. 3664–3674. DOI: 10.1007/s11661-013-1714-y.

[153] Y. Wang, L.-Q. Chen, Z.-K. Liu, and S.N. Mathaudhu. "First-principles calculations of twin-boundary and stacking-fault energies in magnesium". In: *Scripta Materialia* 62.9 (2010), pp. 646–649. ISSN: 1359-6462. DOI: https://doi.org/10.1016/j.scriptamat.2010.01.014. URL: https://www.sciencedirect.com/science/article/pii/S1359646210000151.

[154] L. Wu, V. D. Nguyen, N. G. Kilingar, and L. Noels. "A recurrent neural network-accelerated multi-scale model for elasto-plastic heterogeneous materials subjected to random cyclic and non-proportional loading paths". In: *Computer Methods in Applied Mechanics and Engineering* 369 (2020), p. 113234.

[155] L. Wu and L. Noels. "Recurrent Neural Networks (RNNs) with dimensionality reduction and break down in computational mechanics; application to multi-scale localization step". In: *Computer Methods in Applied Mechanics and Engineering* 390 (2022), p. 114476.

[156] V. Yamakov, D. Wolf, S. R. Phillpot, A. K. Mukherjee, and H. Gleiter. "Dislocation processes in the deformation of nanocrystalline aluminium by molecular-dynamics simulation". In: *Nature Materials* 1 (2002), pp. 45–48. ISSN: 14761122. DOI: 10.1038/nmat700.

[157] L. Yang and K. Dayal. "Formulation of phase-field energies for microstructure in complex crystal structures". In: *Applied Physics Letters* 96 (2010), pp. 2008–2011. ISSN: 00036951. DOI: 10.1063/1.3319503.

[158] M. H. Yoo, J. R. Morris, K. M. Ho, and S. R. Agnew. "Nonbasal deformation modes of Hcp Metals and alloys: Role of dislocation source and mobility". In: *Metallurgical and Materials Transactions A* 33.3 (2002), pp. 813–822. DOI: 10.1007/s11661-002-0150-1.

[159] J. Zhang and S. P. Joshi. "Phenomenological crystal plasticity modeling and detailed micromechanical investigations of pure magnesium". In: *Journal of the Mechanics and Physics of Solids* 60 (2012), pp. 945–972. ISSN:

00225096. DOI: 10.1016/j.jmps.2012.01.005. URL: http://dx.doi.org/10.1016/j.jmps.2012.01.005.

[160] H. Zhou and K. Bhattacharya. "Accelerated computational micromechanics and its application to polydomain liquid crystal elastomers". In: *Journal of the Mechanics and Physics of Solids* 153 (2021). ISSN: 23318422. DOI: https://doi.org/10.1016/j.jmps.2021.104470.